



ELINGAS ČEKAS

**RESEARCH AND
DEVELOPMENT OF
AN ACTIVE ELEMENT
FOR A PRESSURE
SENSOR ON THE BASIS
OF PIEZOELECTRIC
COMPOSITE MATERIAL**

DOCTORAL DISSERTATION

K a u n a s
2 0 2 0

KAUNAS UNIVERSITY OF TECHNOLOGY

ELINGAS ČEKAS

RESEARCH AND DEVELOPMENT OF AN ACTIVE ELEMENT FOR A
PRESSURE SENSOR ON THE BASIS OF PIEZOELECTRIC COMPOSITE
MATERIAL

Doctoral Dissertation
Technological sciences, Mechanical engineering (T 009)

2020, Kaunas

This doctoral dissertation was prepared at Kaunas University of Technology, Faculty of Mechanical Engineering and Design, Department of Mechanical Engineering during the period of 2015–2019. The studies were supported by the Research Council of Lithuania.

Scientific Supervisor:

Prof. Dr. GIEDRIUS JANUŠAS (Kaunas University of Technology, Technological Sciences, Mechanical Engineering, T 009)

This doctoral dissertation has been published at:
<http://ktu.edu>

Editor:

Armandas Rumšas (Publishing Office “Technologija”)

© E. Čekas, 2020

KAUNO TECHNOLOGIJOS UNIVERSITETAS

ELINGAS ČEKAS

AKTYVAUS ELEMENTO SLĖGIO JUTIKLIAMS, PAGRĮSTO
PJEZOELEKTRINE KOMPOZITINE MEDŽIAGA, KŪRIMAS IR TYRIMAS

Daktaro disertacija
Technologijos mokslai, mechanikos inžinerija (T 009)

2020, Kaunas

Disertacija rengta 2015–2019 metais Kauno technologijos universiteto mechanikos inžinerijos ir dizaino fakultete mechanikos inžinerijos katedroje. Mokslinius tyrimus rėmė ir Lietuvos mokslo taryba.

Mokslinis vadovas:

Prof. dr. GIEDRIUS JANUŠAS (Kauno technologijos universitetas, technologijos mokslai, mechanikos inžinerija, T 009)

Interneto svetainės, kurioje skelbiama disertacija, adresas:
<http://ktu.edu>

Redagavo:

Armandas Rumšas (leidykla “Technologija”)

CONTENTS

NOMENCLATURE	7
LIST OF FIGURES	8
LIST OF TABLES	11
INTRODUCTION	12
1. LITERATURE REVIEW	16
1.1. Sensor types and their functionality	16
1.2. Pressure sensors	21
1.3. Transducers and actuators	24
1.4. Dynamic elements of a sensor	27
1.5. Materials for sensing elements	29
1.5.1. Piezoelectric materials	29
1.5.2. Other smart materials	30
1.5.3. Piezoelectric composites	32
1.6. Section conclusions	37
2. PIEZOELECTRIC NANOCOMPOSITE SYNTHESIS AND ANALYSIS ...	39
2.1. Synthesis and formation of piezoelectric composite film	39
2.2. Testing methodology and tools	40
2.2.1. Scanning electron microscopy (SEM)	40
2.2.2. Atomic force microscopy (AFM)	42
2.2.3. Energy dispersive X-ray spectroscopy (EDS)	43
2.2.4. Fourier transform infrared spectroscopy (FTIR)	45
2.2.5. Keithley meter scanner	47
2.2.6. Laser triangulation sensor LK-G3000 and PicoScope 3424 oscilloscope	49
2.2.7. Electronic speckle pattern interferometry system PRISM	51
2.2.8. Voltage standing wave ratio (VSWR)	53
2.2.9. Microhardness measurement	54
2.2.10. Micro-scratch tester MST ³	56
2.3. Structural Composition	57
2.4. Chemical Composition	57
2.5. Piezoresistive characteristics of piezoelectric composite	63

2.6.	Microhardness of Coatings	69
2.7.	Section conclusions	72
3.	MODELLING AND ANALYSIS OF OSCILLATING MEMBRANE FOR PRESSURE SENSOR	74
3.1.	Methodology and tools	74
3.1.1.	Mindlin-Reissner theory for thick plates	74
3.1.2.	Membrane formation	75
3.1.3.	Thermal embossing for microstructure imprinting	77
3.1.4.	Laser Doppler vibrometer	79
3.2.	Shape of the membrane	80
3.3.	Finite element model of the membrane	81
3.4.	Harmonic analysis of multilayered membrane	84
3.5.	Fabrication of multilayered membrane.....	87
3.6.	Finite element model verification.....	90
3.7.	Vibrational analysis of the loaded multilayered membrane	90
3.8.	Optical properties of the multilayered membrane	93
3.9.	Section conclusions	94
	GENERAL CONCLUSIONS.....	96
	LIST OF PUBLICATIONS.....	98
	REFERENCES	101

NOMENCLATURE

AFM – atomic force microscope
BSE – backscattering electrons
EDS – energy dispersive spectrometer
FTIR – Fourier transform infrared spectrometer
HB – Brinell hardness
HK – Knoop hardness
HM – Martens hardness
HV – Vickers hardness
IR – infrared radiation
KTU – Kaunas University of Technology
LED – light emitting diode
LPCVD – low pressure chemical vapor deposition
MEMS – microelectromechanical systems
MOEMS – microoptoelectromechanical systems
PIR – passive infrared sensor
PLA – polylactic acid
PLZT – lead lanthanum zirconate titanate
PMDS – Polydimethylsiloxane
PMN – lead magnesium niobite
PMN-PT – lead magnesium niobite-lead titanate
PVB – polyvinyl butyral
PVDF – polyvinylidene fluoride
PZT – lead zirconium titanate
RIE – reactive ion etching
SE – secondary electrons
SEM – scanning electron microscope
TMAH – tetramethylammonium hydroxide
XRD – X-ray diffraction

LIST OF FIGURES

Fig. 1. Scheme of a resistive flex sensor: a) Top view, b) Lateral view, c) View in the working environment [47]	19
Fig. 2. Schematic representation of the working process of an ultrasonic sensor [54]	19
Fig. 3. Tilt sensor working principle [65]	20
Fig. 4. Piezoresistive pressure sensor [77]	22
Fig. 5. Working principle of a piezoelectric disk [78]	23
Fig. 6. Capacitive sensor with two parallel plates [80]	23
Fig. 7. Comb-drive electrostatic actuator [109].....	25
Fig. 8. Electrostatic harmonic motor [110]	25
Fig. 9. Cantilever based sensor [127].....	27
Fig. 10. Schematic view of a vibrating membrane working in two different environments at once	29
Fig. 11. Composite effects: a) sum, b) combinations, and c) products effects [154]	33
Fig. 12. Chemical structure of polyethersulfone	34
Fig. 13. Chemical structure of polydimethylsiloxane	34
Fig. 14. Chemical structure of polyvinyl butyral	34
Fig. 15. Chemical structure of polypropylene.....	35
Fig. 16. Chemical structure of poly(methyl methacrylate).....	35
Fig. 17. Chemical structure of polyacetic acid.....	35
Fig. 18. Chemical structure of polycarbonate	36
Fig. 19. Chemical structure of polyacrylamide	36
Fig. 20. Chemical structure of polyvinyl chloride.....	36
Fig. 21. Chemical structure of polystyrene	37
Fig. 25. Scanning electron microscope <i>Bruker Quanta 200 FEG</i>	41
Fig. 26. Atomic force microscope <i>JPK Nanowizard 3</i>	43
Fig. 27. X-ray characteristic lines	44
Fig. 28. Energy dispersive X-ray spectrometer <i>X-Flash 4030</i> [178]	45
Fig. 29. Fourier transform infrared spectrometer <i>Vertex 70</i>	46
Fig. 30. <i>Keithley 2002 Series 8½-Digit High Performance Multimeter</i>	47
Fig. 32. Schematics of analysis of piezoresistive characteristics	48
Fig. 33. <i>LK-G82</i> sensor head [187]	49
Fig. 34. <i>LK-G3001P</i> control block [188]	49
Fig. 35. Experimental setup for measurement of piezoelectric properties [189]	50
Fig. 36. Experimental setup for piezoelectric response measurement: (1) pendulum, (2) <i>LK-G82</i> sensor head, (3) sample, (4) <i>PicoScope</i> oscilloscope, (5) <i>LK-G3000</i> control block, and (6) power supply block	51
Fig. 37. Electronic speckle pattern interferometry system <i>PRISM</i>	52
Fig. 38. Schematic view of the experimental setup for <i>PRISM</i> system	52
Fig. 42. <i>Fischerscope HM 2000S</i> microhardness meter.....	55
Fig. 43. Micro-scratch tester <i>MST³</i> [199]	56
Fig. 44. Sample views in SEM: PZT with PVB polymer (a), PZT with PMMA polymer (b), and PZT with PS polymer (c).....	57

Fig. 45. Energy dispersive spectra of PMMA/PZT, PVB/PZT, and PS/PZT samples	58
Fig. 46. Relative proportion (intensity) and distribution maps of PVB/PZT samples	59
Fig. 47. Relative proportion (intensity) and distribution maps of the PMMA/PZT sample.....	60
Fig. 48. Relative proportion (intensity) and distribution maps of PS/PZT sample ..	61
Fig. 48. FTIR spectra of PVB/PZT sample with 80 wt.% PZT.....	62
Fig. 49. Fourier Transform Infrared Spectroscopy spectra of PMMA/PZT sample with 80 wt.% PZT.....	62
Fig. 50. Fourier Transform Infrared Spectroscopy spectra of PS/PZT sample with 80 wt.% PZT.....	63
Fig. 51. The resistance-force relationship: (a) PVB/PZT sample, (b) PMMA/PZT sample, and (c) PS/PZT sample.....	65
Fig. 53. Current–voltage characteristics of each piezoelectric coating	66
Fig. 54. Vibrational response of the (a) PVB/PZT, (b) PMMA/PZT, and (c) PS/PZT coating to a mechanical impulse.....	67
Fig. 55. Holographic interferograms of the (a) PVB/PZT, (b) PMMA/PZT, and (c) PS/PZT coating samples.....	68
Fig. 56. Generated electrical energy from each of the samples by periodical excitation	69
Fig. 57. Martins and Vickers microhardness of each coating	70
Fig. 58. Frictional force, normal force, friction coefficient, and the corresponding panorama image of (a) PVB/PZT, (b) PMMA/PZT, and (c) PS/PZT coatings recorded during the scratch test of each sample	72
Fig. 59. Schematic view of vacuum evaporation process [213].....	76
Fig. 60. Vacuum evaporation equipment <i>YBH-71D3</i>	77
Fig. 61. Schematic view (a) and process graph (b) of thermal embossing technique [218]	78
Fig. 62. Schematic diagram of thermal imprinting with high frequency vibration assistance [221]	78
Fig. 63. Schematic view of imprinting process	79
Fig. 64. Experimental setup of <i>Polytec</i> scanning laser Doppler vibrometer	79
Fig. 65. Circular membrane for comparative analysis	81
Fig. 66. Rectangle membrane for comparative analysis.....	81
Fig. 67. Square membrane for comparative analysis	81
Fig. 68. Schematic drawing of multilayered vibrating membrane: 1 – aluminum layer, 2 – PZT nanocomposite layer, 3 – aluminum layer.....	82
Fig. 69. 3D view of the model with the corresponding boundary conditions and structure: 1 – aluminum, 2 – PMMA/PZT.....	82
Fig. 70. Quadrilateral finite element schematic representation (numbers show the numbering of nodes).....	83
Fig. 71. Hexahedral finite element schematic representation (numbers show the numbering of nodes).....	83
Fig. 72. Mesh of the structure used for finite element model.....	84

Fig. 73. Kinetic energy in resonant frequencies of multilayered membrane.....	85
Fig. 74. 1 st vibration mode of multilayered membrane	85
Fig. 75. 2 nd vibration mode of multilayered membrane	85
Fig. 76. 3 rd vibration mode of multilayered membrane	85
Fig. 77. 4 th vibration mode of multilayered membrane	85
Fig. 78. Von Mises stress distribution on the membrane	86
Fig. 79. Stress distribution on the edge of the membrane	86
Fig. 80. Line graph of stress distribution by the depth of the membrane.....	87
Fig. 81. Fabricated defective membranes.....	89
Fig. 82. Fabricated multilayered membrane with the closest geometry to the model	89
Fig. 83. Comparison of transient response of the finite element model membrane and the fabricated membrane.....	90
Fig. 84. Kinetic energy of the multilayered membrane dependency on the acting pressure.....	91
Fig. 85. Vibrational amplitude distribution of unloaded multilayered membrane ...	92
Fig. 86. Vibrational amplitude distribution of loaded multilayer membrane with 54 kPa external pressure	92
Fig. 87. Oscillations amplitude dependency on external pressure load.....	93
Fig. 88. 3D view of the periodical microstructure imprinted by using hot embossing technique in PMMA/PZT multilayered membrane	93
Fig. 89. Diffraction efficiency and diffraction angle versus period of periodical microstructure.....	94

LIST OF TABLES

Table 1. Advantages and disadvantages of various pressure sensor types [72].....	21
Table 2. Analysis of piezoresistive, piezoelectric, and capacitive pressure sensors	22
Table 3. Families and classes of actuators and sensor transducers	24
Table 4. Pressure sensors with various applications based on various transduction methods.....	26
Table 5. Common polymer types for piezoelectric nanocomposites	33
Table 6. Technical characteristics of <i>Quanta 200 FEG</i> scanning electron microscope	42
Table 7. Technical data of <i>X-Flash 4030</i> detector	45
Table 8. Technical characteristics of Fourier transform infrared spectrometer <i>Vertex 70</i>	47
Table 9. Technical characteristics of <i>LK-G82</i> sensor head.....	49
Table 10. Technical characteristics of <i>LK-G3001P</i> control block.....	50
Table 11. PICO 3424 oscilloscope technical characteristics	51
Table 12. Voltage standing wave ratio meter <i>P2-67</i> technical characteristics.....	53
Table 13. Technical characteristics of micro-scratch tester <i>MST³</i>	56
Table 14. Chemical characterization of PVB/PZT sample	58
Table 15. Chemical characterization of the PMMA/PZT sample	60
Table 16. Chemical characterization of PS/PZT sample	61
Table 17. Gauge factor (GF).....	63
Table 18. Capacitance of each sample.....	66
Table 19. Main factors of created coatings	68
Table 20. Sheet resistivity values of each coating sample	69
Table 21. Martins and Vickers microhardness measurement results.....	70
Table 22. Critical load values of PVB/PZT, PMMA/PZT, and PS/PZT samples ...	72
Table 23. Geometric effect on membrane stresses and deflection.....	81
Table 23. Mesh statistics.....	83
Table 24. Resonant frequency shift of loaded multilayered membrane.....	91

INTRODUCTION

The application of microelectromechanical systems (MEMS) has been widespread in technological solutions found in a variety of areas. Starting only from the beginning with silicon etching and polymer processing, it has extensively grown during the last few decades due to a large interest in laser and robotics technologies, measurement and medical applications. These industry segments are similar regarding the way of acting: all of them require high quality, sensitivity, high resolution, and reliable devices. All of the above mentioned properties can only be sought if the technologies and materials of new and improved devices are present. By searching for the optimal alternatives to the latest solutions, many scientists have been assigned continuous funding in MEMS and microoptoelectromechanical systems (MOEMS). Consequently, many successful projects have been completed which satisfy the requirements of the previously listed industry segments.

It is crucial to be able to control the MEMS device if high sensitivity is expected. The high quality factor (Q-factor) is a critical condition in this segment. A variety of aspects are connected with the ability to increase the Q-factor of the device: structural dimensions, the type of the structure, the class of the material in use, its chemistry, defects, microstructure, residual stress, surface chemistry and topography, the mode of vibration, the frequency of oscillation, temperature, pressure, the amplitude of oscillation, as well as the nature and structure of its boundaries [1]. On the other hand, the type and the material of which the oscillator, being the main component in the MEMS device, is fabricated plays a vital role. In the technological development, there are many various types of materials in use, such as polyethersulfone (PESU), polydimethylsiloxane (PMDS), nylon, polypropylene (PP), polyactic acid (PLA) nanofibers, cellulose, polycarbonate (PC), polyacrylamide (PAM), cellulose acetate, polyvinyl chloride (PVC), polyamide/polyurethane (PA) [2–12], polyvinylidene fluoride (PVDF) [4]. The selection of the material plays a key role in designing MEMS devices. Additionally, the designing of novel devices includes the creation of novel active elements and materials. Their properties can be adjusted in order to meet the system requirements.

This thesis is based on solving many technological problems, such as nanocomposite material usage for active element fabrication for a MEMS device, sensitivity improvements, the accuracy of measurements, and combination of feedback signal outputs. Major investigations and the attained knowledge in this thesis came from sensors and their operation, periodical microstructure formation principles, materials science and analysis fields. One of the main areas of focus of this research was to choose a low cost and simple method to improve today's technologies in creating MEMS devices.

Part of the experimental work conducted for this thesis were funded by grants “Development and analysis of new type microresonator for microelectromechanical systems” (No. MIP-081/2015) and “Research and development of innovative functional nano/micro components for micro hydrolic devices in biomedicine” (No. S-MIP-17-102) from the Research Council of Lithuania.

The aim of the thesis

The aim of the thesis is to develop and analyze a piezo-active membrane for a pressure sensor on the basis of a piezoelectric nanocomposite material.

The objectives of the thesis

In order to achieve the above stated thesis aim, several objectives were raised:

1. To identify and investigate materials, technology, tools, and methodology for the development of a piezo-active membrane for a pressure sensor on the basis of a piezoelectric nanocomposite material with electro-optic feedback signal outputs.
2. To develop and analyze the piezoelectric composite material for a piezo-active membrane for an electro-optic pressure sensor.
3. To create a finite element model of a piezo-active membrane for a pressure sensor on the basis of the piezoelectric nanocomposite material with electro-optic feedback signal outputs.
4. To fabricate and investigate the functional prototype of the piezo-active membrane for an electro-optic pressure sensor.

Research methodology

Theoretical and experimental analysis methods have been applied in the study of novel nanocomposite materials and their integration into a MEMS device. In order to evaluate the chemical, piezoelectric, and mechanical properties of these novel materials as well as to analyze their surface morphology, the following equipment and methodology was used: scanning electron microscopy, atomic force microscopy, energy dispersive X-ray spectroscopy, Fourier transform infrared spectroscopy, *Keithley* meter scanner 2002 series, laser triangular displacement sensor *LK-G3000* with *PicoScope 3424* oscilloscope, electronic speckle pattern interferometry system *PRISM*, voltage standing wave ratio methodology, Vickers and Martins microhardness analysis. Finite element models were created and calculated by using *COMSOL Multiphysics* software environment. Additionally, *GSolver* software for diffractive element calculations was used. High voltage polarization equipment was fabricated by scientists from the *Institute of Materials Science* (KTU).

Experimental research was conducted at Kaunas University of Technology, Faculty of Mechanical Engineering and Design, Institute of Mechatronics and the Institute of Materials Science.

Scientific novelty

The novelty of this research is based on piezocomposite material applicability to the pressure sensor field:

1. A piezoelectric nanocomposite has been developed, in which, a periodical microstructure can be formed; this provides optical feedback based on the principles of coherent optics.
2. A piezoelectric nanocomposite developed in the interaction with other structural elements of a pressure sensor improves materials adhesion during

their dynamic interaction and enhances the stability of the optical feedback signal.

3. The selected geometric shape of the active element for a pressure sensor allows correlation of electrical and optical signals while providing maximum stresses and strain in electro-optical pressure sensors.

Defended statements

1. The developed piezoelectric nanocomposite wherein periodical microstructures with the period reaching the micrometer level can be formed ensures possibility to use coherent optics principles by using lasers of 441–632 nm wavelength.
2. The developed piezoelectric nanocomposite shows high resistance to scratching while withstanding critical loads of up to 4 N, which ensures prevention of uncoupling of the piezoelectric nanocomposite during micro formation and high quality in the further steps of fabrication.
3. The application of commonly used excitation voltages (up to 200 V) allows to achieve micrometer-level deflections and mega Pascal-level stress of the square-shaped piezoelectric membrane.

Practical value

1. The developed piezoelectric nanocomposite with an integrated periodic microstructure offers the possibility to operate at the micrometric level, which allows creating a new type pressure sensor.
2. The developed piezoelectric nanocomposite materials expand the usage of sensing technologies and increase the effectiveness of the sensing system.
3. The developed piezoelectric nanocomposite allows forming a periodical microstructure on the surface of an active element for a pressure sensor enabling optical detection.
4. Correlation of electrical and optical feedback signals improves the temporal pressure changes detection effectiveness of the active element of the pressure sensor.

Approval of the doctoral thesis

This research was funded by grants “Development and analysis of new type microresonator for microelectromechanical systems” (No. MIP-081/2015) and “Research and development of innovative functional nano/micro components for micro hydrolic devices in biomedicine” (No. S-MIP-17-102) from the Research Council of Lithuania. The results have been presented in 5 articles in the ISI Web of science database with the citation index, 6 articles in the ISI Web of science database without the citation index and 5 conference proceedings

The results of this doctoral thesis have been presented at 6 scientific conferences:

1. Mechanika 2016: proceedings of the 21st international scientific conference, 12–13 May, 2016, Kaunas, Lithuania. “Development of finite element model for new type composite piezoelectric material.”

2. Proceedings of SPIE: Optical sensing and detection IV, 3 April, 2016, Prague, Czech Republic. “Developing and investigation of MOEMS type displacement-pressure sensor for biological information monitoring.”
3. Proceedings of SPIE: Optical modelling and design IV, 3 April, 2016, Prague, Czech Republic. “Development and analysis of new type microresonator with electro-optic feedback.”
4. Proceedings of SPIE: Smart sensors, actuators, and MEMS VIII, 8–11 May, 2017, Barcelona, Spain. “Influence of binding material of PZT coating on microresonator’s electrical and mechanical properties.”
5. SPIE BIOS: Microfluidics, BioMEMS, and Medical Microsystems XVI: 19 February, 2018, San Francisco, California, United States. “Q-factor control of multilayer micromembrane using PZT composite material.”
6. Bioinformatics and biomedical engineering: 6th international work-conference, IWBBIO 2018, 25–27 April, 2018, Granada, Spain. “Composite piezoelectric material for biomedical micro hydraulic system.”

Structure of the doctoral thesis

The doctoral thesis contains the introduction, 3 chapters, general conclusions, a list of the author’s scientific publications, and a list of literature featuring 221 references. The doctoral thesis is composed of 114 pages, 89 figures, and 24 tables.

1. LITERATURE REVIEW

Many different sensing devices surround us each day in the nature. All living organisms are made of cells whose functions are imitated by mechanical sensors in industries. They detect various physical changes of light, motion, magnetic fields, temperature, moisture, gravity, humidity, sound, vibration, pressure, electrical field, or other physical aspects, such as motion or stretch. This is just a small portion of all the natural fields of sensing wonders. Some of them are imitated by mechanical alternatives in the broadest definition sense; they are commonly called ‘sensors’.

A sensor is a part of any micromechanical system (MEMS) which works in collaboration with other electronic devices. A microelectromechanical system contains the central device which has the function of data processing, and additional units surrounding the central device which gather information and send it as a signal [13]. A sensor, as described by the *Merriam-Webster* dictionary, is a device that responds to a physical stimulus (such as heat, light, sound, pressure, magnetism, or a particular motion) and transmits a resulting impulse (as for measurement or operating a control) [14]. The stated resulting input is usually called the output signal of the sensor. Some of them are electrical signals, mechanical signals, optical signals, etc. Additionally, a sensor can also be named as a transducer, but, in this case, the transducer acts as an energy convertor, while a sensor responds to a change of a specific physical property [15].

1.1. Sensor types and their functionality

Many types of sensors can be found in today’s industry fields. Their classification is usually very different, but classifications often end up taking into account the application segment, specifications, working physics, and the detection area. Another important classification aspect is the research object. Classifying sensors by the objective of the research would end up in a similar manner:

- Light sensor – IR sensor (IR transmitter/IR LED), photodiode (IR receiver), light dependent resistor;
- Temperature sensor – thermistor, thermocouple;
- Pressure/force/weight sensor – strain gauge (pressure sensor), load cells (weight sensor);
- Position sensor – potentiometer, encoder;
- Hall sensor (detect magnetic field);
- Flex sensor;
- Sound sensor (microphone);
- Ultrasonic sensor;
- Touch sensor;
- Passive infrared sensor (PIR);
- Tilt sensor – accelerometer;
- Gas sensor.

Although this list is not an official one, nor does it include all the possible sensor types, but it helps to paint the big picture of the vast number of possibilities for the application of sensors and their differences.

The light sensor is able to measure change or difference of one or several light sources. They have significant advantages compared to the conventional sensors. Some of the advantages are the greater sensitivity, electrical passiveness, freedom from electromagnetic interference, a wide dynamic range, and multiplexing capabilities. This type of sensors is used in a huge number of researches and commercial applications incorporating quality and process control, medical technologies, metrology or imaging [16–18]. Light sensors are also denoted by several different sensing abilities. In some structures, the sensor measures the intensity change of the light source. Other sensors may look for a change in the light source phase. Also, a sensing solution would be the light quantity measurement from a reflected surface.

Many industry fields benefit from a temperature monitoring system. Their common uses in the daily life include the monitoring of a car’s engine temperature or human health, food transportation, agriculture. These temperature monitoring systems usually include a thermocouple, a thermal resistor, a PN junction or any other lead-type temperature sensors [19]. A thermocouple outputs a temperature-dependent voltage which can be used to monitor the temperature. Monitoring is based on the following Equation (1.1.1):

$$V = \int_{T_{ref}}^{T_{sense}} (S_+(T) - S_-(T)) dT, \quad (1.1.1)$$

where T_{sense} is the sensing temperature of the thermocouple, T_{ref} is the reference temperature, T is the temperature dependency, and Seebeck coefficients (conversion of heat directly into electricity at the junction of different types of wires) are represented here with S_+ and S_- elements, and are taken off the conductors attached to the positive and negative terminals of the voltmeter [20].

A thermistor, on the other hand, senses the change of resistance, which depends on the temperature. A linear relationship of resistance and temperature can be expressed by Equation (1.1.2):

$$\Delta R = k\Delta T, \quad (1.1.2)$$

where k is the temperature coefficient of resistance, and T is the temperature.

The temperature coefficient of resistance determines the polarity of the thermistor. If the coefficient is positive, then the resistance increases with the increasing temperature. When the resistance decreases with the increasing temperature, the temperature coefficient of resistance is negative [21]. Thermistors are widely used as low-temperature thermometers, inrush current limiters [22], fluid temperature monitoring, or as a part of an inertial sensor [23].

Thousands of applications are incorporating pressure sensors for their stable work. In addition to the main purpose of pressure monitoring, they can also be used for fluid/gas flow, speed water level, and altitude measurement [24–26].

One of the examples could be the strain gauge which is used to measure the strain on an object. This type of sensor monitors the electrical resistance change during the deformation of an object. An output sensor voltage can be determined by Equation (1.1.3):

$$SV = EV \frac{GF \cdot \epsilon}{5}, \quad (1.1.3)$$

where EV is the bridge excitation voltage, GF is the Gauge Factor, and ϵ is the strain of the strain gauge [27].

Strain could be caused by external impact or internal change. It could be caused by forces, pressures, moments, heat or even structural changes of the material. Various applications of this kind of sensors are present: air cooling systems for mechanical strain measurements during the thermal cycle [28], laser forming [29], medical applications [30, 31]. New technology even allows drawing working strain gauges with a pencil [32].

The load cell, on the other hand, works as a force gauge. It produces an electrical signal which is linearly proportional to the measured force. A load cell can also be a strain gauge. The deformations cause change in the resistance, and the electrical value of the output change depends on the calibration. Mostly, this type of sensors is used in the weighting industry [33, 34]. Moreover, biomedical applications also benefit from load cells [35, 36].

A position sensor, as stated by its title, senses the change in the position or displacement of the unit. They can be absolute position sensors or relative position sensors. The sensor detects the movement of an object and converts it into an appropriate signal. There are also various types of position sensors:

- The potentiometric position sensor: its operation is based on the resistive effect [37].
- The capacitive position sensor: its operation is based on either the changing dielectric constant or on the changing overlapping area [38].
- The magnetostrictive position sensor: its operation is based on measurements between the head end of a sensing rod and the position magnet [39].
- The eddy current-based position sensor: its operation is based on the eddy current induced change of the secondary magnetic field caused by the presence or absence of a conducting material [40].
- The Hall effect-based magnetic position sensor: its operation is based on the movement of a body, which leads to the formation of a magnetic field [41].
- The optical position sensor: its operation is based on the change in one of the following characteristics: wavelength, intensity, phase, or polarization [42].

These and similar types of position sensors can be found in the vast majority of applications: medical equipment [43, 44], packaging machines [45], injection molding machines [46], etc.

Bending of a surface can be measured with a flex sensor (Fig. 1). As well as the previously defined sensors, this one is also directly proportional to the resistance which occurs due to bending.

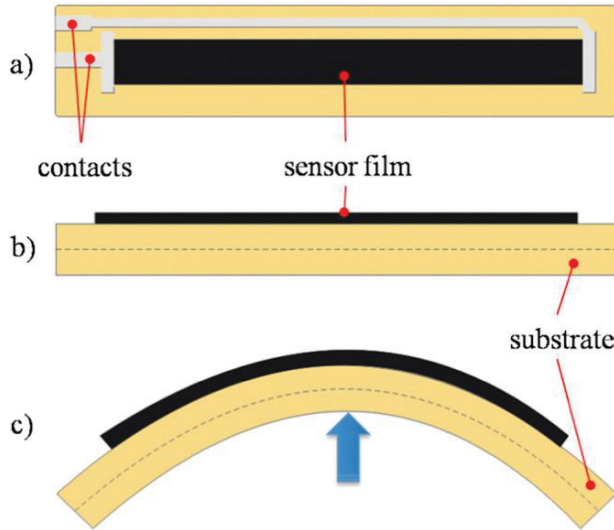


Fig. 1. Scheme of a resistive flex sensor: a) Top view, b) Lateral view, c) View in the working environment [47]

A flex sensor works based on the same principle as strain gauges. It can be used in computer interfaces, rehabilitation, security systems, or music interfaces [48].

Various sound sensors are also present in today’s industry. One can find dynamic microphones, condenser microphones, ribbon microphones, carbon microphones, and many other types of sound sensors. All of them convert sound into an electrical signal; they find application in medicine [49], environmental monitoring [50], music industry [51], aviation [52], and various other fields may also be noted [53].

The ultrasonic sensor, on the other hand, is employed to measure distance by using ultrasonic waves. An emitted ultrasonic wave travels to the target and back. The time between the emission and reception is measured and evaluated as the output of the sensor (Fig. 2).

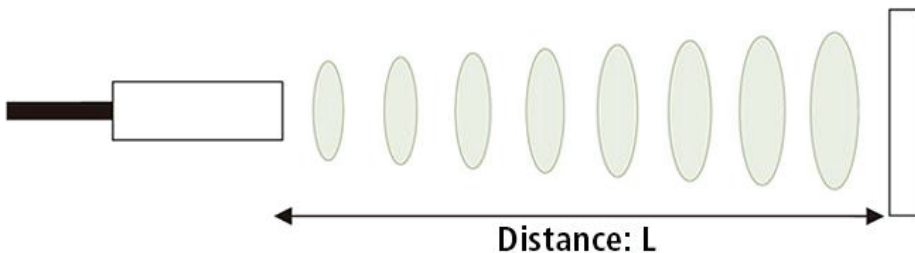


Fig. 2. Schematic representation of the working process of an ultrasonic sensor [54]

There is also a possibility that the transmitter and the receiver are in separate units, but they cooperate based on the calibration process.

A very common application is the parking sensors of a car. They measure the distance to the obstacle, and the received electrical output signal is converted either to the graphical view or a sound for the driver [55]. A similar application has also been developed to measure either the ultrasonic velocity in any material state or object detection in shallow or deep water [56]. Medicine is also benefiting by using ultrasonic sensors: imaging and therapy [57], measuring the Lung Clearance Index [58], or intravascular applications [59].

A touch sensor works when an object gets in physical contact with it. They are more sensitive, they can respond to various kinds of touch, such as tapping, swiping and pinching. Mainly, touch sensors can be located in tech devices (smartphones or tablet computers [60]). Yet they can also be found in household items [61], automobile industry [62], and many other industry fields.

If one wished to employ the infrared light, it is possible to measure its radiation change with a PIR. Even though infrared radiation (IR) is not visible to the human eye, every single object whose temperature is above the absolute zero emits heat energy in the form of radiation. A PIR sensor can detect this radiation with its sensor face.

A PIR sensor is mainly used for motion detection. Security alarms [63] or automatic lights [64] are based on this technology.

Tilt sensors produce an electrical signal which is dependent on the angular movement of the device. They measure the slope and tilt within a limited range of motion. Usually, a tilt sensor consists of a rolling ball with a conductive plate beneath them. By moving the sensor, the ball moves to the plates and forms an electrical circuit. Otherwise, the ball does not conclude the electrical circuit and there is no signal (Fig. 3).

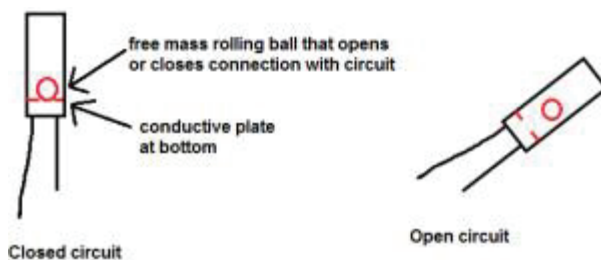


Fig. 3. Tilt sensor working principle [65]

Tilt sensors, as any of the above listed ones, are denoted by a variety of application capabilities. Some of them are suitable for solving environmental problems [66–68], medical applications [69], or even for gravitational wave detection [70].

The gas sensor helps to detect the presence of gases in the analyzed area. Often is a part of safety systems, i.e., a home security system involving protection against fire. A specific gas concentration level is measured, and the sensor serves as a reference scale. If the response surpasses a certain level which has been pre-set

before, the alarm will activate to warn the surroundings. Essentially, all types of sensors serve the same function. Usually, only the detector, which is a part of the sensor, changes depending on the required technology [71].

Each overviewed sensor has a common element – the transducer. It converts a property change into an electrical or other kind of signal, which can then be read by computer software or some following devices in the circuit.

1.2. Pressure sensors

Pressure in a pressure sensor is mainly sensed by mechanical elements, such as shells, tubes, and plates, which are designed to deform when pressure is applied. Deformation is then transduced to obtain an electrical or any other type of signal. In general, pressure sensors may differ in many fields: technology, design, performance, application, or costs. They can also be classified. One of the classification types is a classification based on transduction principles. These transduction principles can be resistive/piezoresistive, tunnel effect, capacitive, optical, ultrasonic, magnetic, and piezoelectric. The advantages and disadvantages of various transduction principles are listed in Table 1.

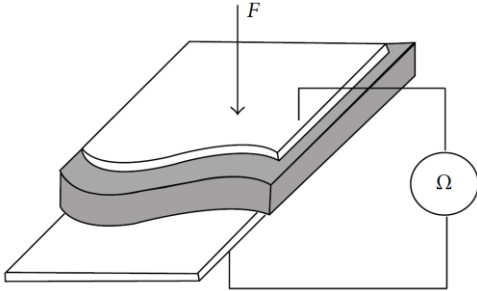
Table 1. Advantages and disadvantages of various pressure sensor types [72]

Type	Advantages	Disadvantages
Resistive	<ol style="list-style-type: none"> 1. Sensitive 2. Low cost 	<ol style="list-style-type: none"> 1. High power consumption 2. Generally detect single contact point 3. Lack of contact force measurement
Piezoresistive	<ol style="list-style-type: none"> 1. Low cost 2. Good sensitivity 3. Low noise 4. Simple electronics 	<ol style="list-style-type: none"> 1. Stiff and frail 2. Nonlinear response 3. Hysteresis 4. Temperature sensitive
Tunnel effect	<ol style="list-style-type: none"> 1. Sensitive 2. Physically flexible 	<ol style="list-style-type: none"> 1. Nonlinear response
Capacitive	<ol style="list-style-type: none"> 1. Sensitive 2. Low cost 3. Availability of commercial A/D chips 	<ol style="list-style-type: none"> 1. Hysteresis 2. Complex electronics
Optical	<ol style="list-style-type: none"> 1. Physically flexible 2. Sensitive 3. Fast 4. No interconnections 	<ol style="list-style-type: none"> 1. Loss of light by micro bending chirping 2. Power consumption 3. Complex computations
Ultrasonic	<ol style="list-style-type: none"> 1. Fast dynamic response 2. Good force resolution 	<ol style="list-style-type: none"> 1. Limited applicability at low frequency 2. Complex electronics 3. Temperature sensitivity
Magnetic	<ol style="list-style-type: none"> 1. High sensitivity 2. Good dynamic range 3. No mechanical hysteresis 4. Physical robustness 	<ol style="list-style-type: none"> 1. Suffer from magnetic interference 2. Complex computations 3. Somewhat bulky 4. Power consumption
Piezoelectric	<ol style="list-style-type: none"> 1. Dynamic response 2. High bandwidth 	<ol style="list-style-type: none"> 1. Temperature sensitivity 2. Not so robust electrical connection
Conductive rubber	<ol style="list-style-type: none"> 1. Physically flexible 	<ol style="list-style-type: none"> 1. Mechanical hysteresis 2. Nonlinear response

There are thousands of various technological approaches used in pressure sensor designs. These technological approaches cover the sensing element method, material, MEMS, nanotechnology, and many other aspects. In addition, a significant difference can be seen in different types of pressure sensor results which stem from a different material or with different functional properties.

Significant attention has been received by the MEMS technology using pressure sensors during the recent years. Due to their numerous advantages over conventional electromechanical sensing technologies, the rise of MEMS has been noted and significant. The abilities and properties of low volume, low weight, low cost, high performance, large scale integration, low power consumption, wider operating temperature, and higher output signal differentiate MEMS from other sensing technologies [73]. To understand the differences of the majority of sensors, we need to look deeper into a few sensor types. Table 2 shows three most common sensor types: piezoresistive, piezoelectric, and capacitive which are also denoted by similar advantages and disadvantages [74–76].

Table 2. Analysis of piezoresistive, piezoelectric, and capacitive pressure sensors

Type	Summary
Piezoresistive	<p>Piezoresistive sensors employ the change of electrical resistance in a material when it has been mechanically deformed. The resistance can be calculated with Equation (1.2.1):</p> $R = \frac{\rho \times l}{t \times \omega}, \quad (1.2.1)$ <p>where ρ, l, t, and ω in Equation (1.2.1) show the resistivity, length and thickness of the piezoresistor, and the width of the contact.</p> <p>An example of a piezoresistive sensor is given in Fig. 4.</p>  <p>Fig. 4. Piezoresistive pressure sensor [77]</p> <p>Low cost, good sensitivity, relatively simple construction, long-term stability with low noise, accuracy and reliability properties show strong development of this technology. Moreover, a piezoresistive sensor is easy to fabricate and integrate with into a MEMS system due to the characteristics of piezoresistive materials.</p>
Piezoelectric	<p>Piezoelectric sensors convert the applied stress or force into electric voltage. Fig. 5 shows the working principle of a piezoelectric disk.</p>

Type	Summary
	<div data-bbox="315 172 1056 546" data-label="Image"> </div> <p data-bbox="431 573 946 600">Fig. 5. Working principle of a piezoelectric disk [78]</p> <p data-bbox="296 618 1127 728">A piezoelectric material, also called a smart material, benefits of the piezoelectric effect, which helps it to be used as a sensor or even as an actuator. In addition, piezoelectric materials have high sensitivity and high voltage outputs when force is applied.</p> <p data-bbox="296 728 1127 864">These sensors are also denoted as a passive sensor. It can offer high reliability that is useful to apply in a vast number of applications. Many piezoceramic materials, for example, lead zirconate titanate (PZT), are suitable and used in this type of sensors. Additionally, composite materials consisting of PZT and polymers are now more and more commonly employed in various applications.</p> <p data-bbox="296 864 1127 946">Piezoelectric sensors offer excellent mechanical flexibility, high piezoelectric coefficients, dimensional stability, low weight, workability, chemical stability, and chemical inertness [79].</p>
Capacitive	<p data-bbox="296 955 1127 1064">Capacitive sensors are denoted by one distinguished feature: the movement caused by an external force or pressure causes the area or gap between two plates to change. This change is registered, and the change of capacitance is calculated by using Equation (1.2.2).</p> $C = \frac{\epsilon_0 K A}{d} \tag{1.2.2}$ <p data-bbox="296 1155 1127 1264">Here, C is capacitance, ϵ_0 is the relative permittivity of the free space constant, K is the dielectric constant of the material in the gap, A is the area of the plates, and d is the distance between the plates. A schematic example of a capacitive sensor with two parallel plates can be seen in Fig. 6.</p> <div data-bbox="476 1274 920 1583" data-label="Image"> </div> <p data-bbox="444 1601 972 1628">Fig. 6. Capacitive sensor with two parallel plates [80]</p> <p data-bbox="296 1647 1127 1674">Capacitive sensing technology has been improved for a long time now, with a result</p>

Type	Summary
	of excellent features of high spatial resolution, good frequency response, low power consumption, and a large dynamic range [81]. It is considered as one of the most sensitive techniques for detecting small deflections of structures [82].

To summarize the information presented in Table 2, one can state that there is no ideal pressure sensor technology that can be used in all applications since each application is denoted by specific advantages and constraints.

1.3. Transducers and actuators

The majority of actuators and sensor transducers consist of four groups: electrostatic, piezoelectric, thermal, and magnetic. When dividing them into families, a more detailed division of each of the groups can be shown as in Table 3.

Table 3. Families and classes of actuators and sensor transducers

Electrostatic	Piezoelectric	Thermal	Magnetic	Optical
Parallel plate [83]	Expansion [93]	Solid expansion [95]	External field [102]	Light emitting diodes [106]
Inchworm [84]	Bimorph [94]	Bimorph [96]	Electromagnetic [103]	Liquid crystal displays [107]
Distributed [85]		Fluid expansion [97]	Magnetostrictive [104]	Reflective micromechanical light modulators [108]
Repulsive force [86]		Topology optimized [98]	Magnetic relay [105]	
Comb drive [87]		Shape memory alloy [99]		
Impact [88]		State change [100]		
Scratch drive [89]		Thermal relay [101]		
Electrostatic relay [90]				
S-shaped [91]				
Curved electrode [92]				

This is a non-complete list of possible actuators and sensor transducers, as it is only an example of scattering of some of the possible solutions. It is based on grouping the actuators as much as possible.

Electrostatic actuation is based on the attraction of two oppositely charged plates. By incorporating MEMS devices, it is possible to fabricate conductive plates with a small gap between them. To calculate the force between the plates Equation (1.3.1) comes in play

$$F = \frac{\partial W}{\partial x} = \frac{1}{2} \frac{\partial C}{\partial x} V^2, \quad (1.3.1)$$

where C is the capacitance between the plates, V is the voltage of the charge, x is the distance between the plates, and energy W can be determined with Equation (1.3.2).

$$W = \frac{1}{2} CV^2 \quad (1.3.2)$$

On the other hand, comb-drive-type actuators employ a high number of fine interdigitated fingers which are actuated by the voltage applied between them (Fig. 7). The force generated by an actuator is directly proportional to the number of

fingers. The number of fingers is related to the value of capacitance as it is based on the area.

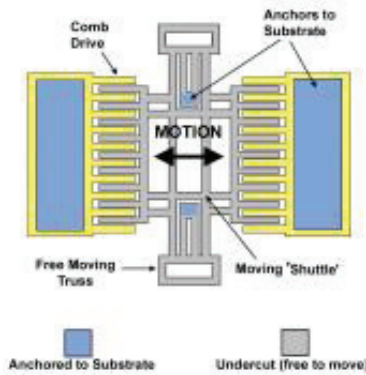


Fig. 7. Comb-drive electrostatic actuator [109]

Electrostatic rotary motors are another great example as they rely on a freely-moving rotor in the center and a surrounding circle of capacitive plates (Fig. 8). Their phase changes to drive the rotor. Harmonic motors turn in a larger stator ring, which allows to reduce the sliding friction as well as to increase the electrostatic force.

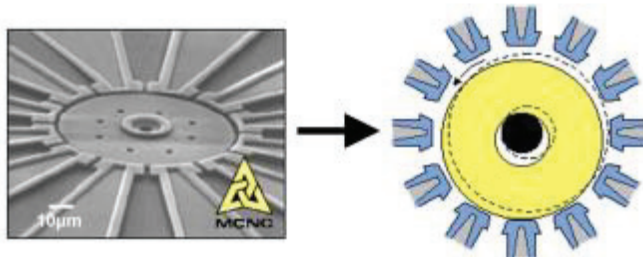


Fig. 8. Electrostatic harmonic motor [110]

Piezoelectric actuation works based on the piezoelectric effect. The electrically caused strain is directly proportional to the applied potential difference. High forces can be achieved by employing only lower voltages (in the 10^6 levels). Nevertheless, there are some disadvantages, such as the dependency on the geometry [111]. Additionally, the piezoelectric actuator is fairly complex to fabricate [112] and has only small actuation displacements [113]. To reach large displacements, multiple piezoelectric layers are used to form a piezoelectric bimorph [114].

Thermal actuators tend to feature tiny heaters or resistors in their structure. They can be controlled, and they can locally heat only specific areas. The basic thermal actuation uses the difference in the thermal coefficients for the expansion of two bonded materials. For example, a shape memory alloy changes its length as it contracts when heated.

A current-carrying conductor creates a magnetic field. Magnetic actuation here is based on this phenomenon. By interacting with another external magnetic field, a mechanical force is produced.

The final class of actuators in Table 3 is the optical actuators. They can be active or passive. For example, passive devices are couplers, mirrors, wavelength division multiplexers, polarizers, etc. The active class, on the other hand, are laser emitting diodes, photodiodes, and optical switches [115]. Their application is based on the control and analysis of the acquired optical data.

If we look more profoundly into the field of pressure sensors, they can be differentiated by transduction methods as well. In Table 4, there are some examples of designation of the development of pressure sensors.

Table 4. Pressure sensors with various applications based on various transduction methods

Transducer method [Reference]	Material type	Limitations	
		Advantages	Weaknesses
Piezoelectric [116]	Liquid crystal polymer	1. Detection of very low frequency (down to 0.1 Hz) in water 2. High resolution (3 mms ⁻¹) 3. Self-powered and passively sensing of underwater objects	1. Applied underwater
Resistive [117]	Conductive rubber	1. Flexibility and stretchability 2. Linearity	1. Needs external power 2. Maximum pressure is low
Strain gauge [118]	Polymer	1. Measurement of normal and shear loads simultaneously	1. Low force capacity (0.6 N)
Piezoresistive [119]	Silicon rubber	1. Highly sensitive sensor	1. Complex design 2. Inflexibility
Capacitive [120]	Polymer	1. Measure normal and shear force distribution	1. Nonuniform gap between electrodes
Piezoresistive [121]	Silicon	1. High spatial resolution (0.42 mm) 2. Large scale sensing array	1. Complex design
Piezoresistive [122]	Elastic rubber	1. Detection of a three-dimensional force 2. Good flexibility and taped on nonplanar surface	1. Large area skin with low density of receptors
Piezoresistive [123]	Polysilicon	1. High resolution shear and normal force 2. Stress	1. Sensor array is high (64 × 64) 2. Needs complex signal condition circuit
Capacitive [124]	Silicon	1. Low cost 2. Simple construction	1. Low resolution (0.05 mm) 2. Measures normal force only
Ultrasonic [125]	Ferroelectric polymer	1. Operation at higher frequencies	1. Low resolution (<3 mm) 2. Absorption of the ultrasonic signal in air

The above mentioned transducers and actuators are an essential part of a sensor. In the pressure sensor industry, they can be classified in two major groups: cantilevers or diaphragms.

1.4. Dynamic elements of a sensor

As mentioned in Paragraph 1.3, there are two major groups of dynamic elements. Both of them come with their own specific technical characteristics as well as their strengths and weaknesses.

To begin with, cantilevered beams are the most common structures in the field of MEMS. It is the simplest mechanical structure which is clamped at one end and is free at the other end (Fig. 9). It is a rectangular-shaped structure, much longer if compared to its width, and its thickness is much smaller than its other two parameters (length or width). Sensors based on cantilevers as their dynamic element have numerous applications in diverse fields. They range from engineering to natural and physical sciences. This kind of sensors is used for the detection of small masses, biomolecular binding events, and non-contact topographic and localized charge imaging when using atomic force microscopy [126].

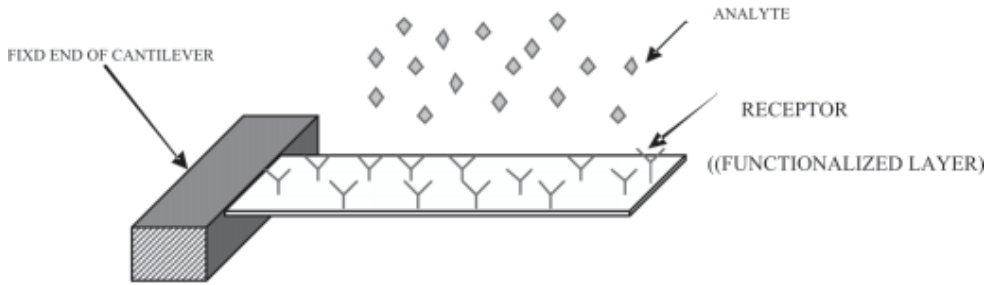


Fig. 9. Cantilever based sensor [127]

MEMS cantilevers are usually fabricated from such materials as silicon (Si), silicon nitride (Si_3N_4), or polymers.

In order to understand the effect of a cantilever, Stoney's formula can be used (Equation 1.4.1) to calculate the resulting surface stress change [127].

$$\Delta\sigma = \frac{Et^2}{[4R(1-\nu)]} \quad (1.4.1)$$

In the equation, ν is Poisson's ratio, E is Young's modulus, R is the bending radius of the cantilever, and t is the thickness of the cantilever.

In addition, the relation of cantilever's spring constant k to the cantilever's dimensions and material constants produces Equation (1.4.2).

$$k = \frac{F}{\delta} = \frac{E\omega t^3}{4L^3} \quad (1.4.2)$$

Here, F is the force, and δ is the deflection, ω is the width of the cantilever, E is the elastic modulus of the cantilever, t is the thickness of the cantilever, and L is its length. The cantilever's spring constant is also related to ω_0 , which is the resonant frequency of the cantilever. When using Equation (1.4.3), the cantilever resonance frequency can be calculated by knowing the $m_{equivalent}$ mass of the system.

$$\omega_0 = \sqrt{\frac{k}{m_{equivalent}}} \quad (1.4.3)$$

Change in the applied force to a cantilever can shift the resonant frequency.

The principal strength of cantilevers in MEMS is their inexpensive and easy fabrication in large numbers. Additionally, they feature lower stiffness and reduced sensitivity because of their temperature and residual stress. On the other hand, the weaknesses of these cantilevers are based on their practical applications. The superlinear dependencies (square and cubic dependencies of cantilever performance specifications on the dimensions) show that this dynamic element is highly sensitive to change in the process parameters, especially to the thickness of the cantilever [128].

Cantilever-based sensors are used in various applications: for the measurement of object-contacting forces [129], for measuring elastic body deformations, when it is embedded with the device [130], for measuring air flows and vibrations [131, 132], for measuring differential air pressure [133], for measuring the differential pressure between cavities and the external environment, etc. [134].

On the other hand, pressure sensors are primarily diaphragm-based [135]. MEMS offer a different fabrication process to the fabrication of diaphragms in various applications. The different shapes of diaphragms (square, rectangular, and circular shapes) play a significant role in the operation of different applications. The working principle of a diaphragm is based on the force applied on one side of the diaphragm, which causes its deflection. It is described by Midlin-Reissner theory for thick plates, which is an extension of Kirchhoff-Love plate theory that takes into account shear deformations through-the-thickness of a plate [136].

If we take into account the usage of vibrating diaphragms, they not only allow continuous vibration throughout the whole structure, but also offer the possibility of working in two environments at the same time (Fig. 10). One of the sides of the vibrating diaphragm can be immersed into the analyte which has to be analyzed, but the other side is freely working in ambient conditions or in vacuum where it can be connected to additional measuring tools or even can work in different pressure. A diaphragm-based resonating device would be able to measure the pressure of the analyte even in very large pressure areas, where additional overpressure from the free side of the diaphragm would be used in order to prevent structural failures.

The dynamic elements of diaphragms are characterized by high pressure sensitivity and significantly lower temperature sensitivity. They can operate up to temperatures of about 300 °C and remain almost free of hysteresis [137]. Additionally, the diaphragm can minimize the nonlinearity of a sensor [138].

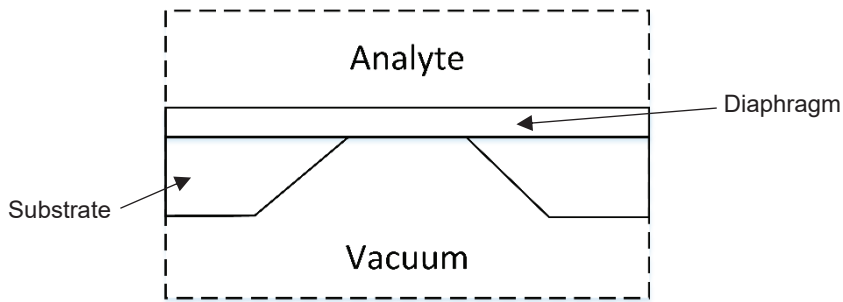


Fig. 10. Schematic view of a vibrating membrane working in two different environments at once

Diaphragms have been widely used in various applications for pressure sensors. One of the most promising industries for their application is biomedicine. Here, diaphragms are employed for pressure sensors to monitor health and tactile touch [139], blood pressure [140], or for any other medical application [141]. However, there are many other fields of science where the diaphragm type pressure sensors are common, such as acoustic pressure sensing and acoustic spectroscopy [142], gas pressure monitoring [143], and environmental applications [144].

The right choice of the material for the vibrating diaphragm can also help to control its geometrical, optical, and mechanical parameters across a wide range of oscillation frequency.

1.5. Materials for sensing elements

In MEMS, many different types of materials are used for their functional element fabrication. The tendency is that they have to be smart, adaptive, and intelligent materials or structures. On the other hand, they cannot work on their own and need to have supporting equipment, such as microprocessors, computers, or control algorithms in order to achieve the designated sensitivity, efficiency, and quality of performance. Sensors with control systems redefined the concept of MEMS from the traditional passive and inflexible system to the newly developed, functional, active and flexible system which is capable of self-diagnosis, self-sensing, and control [145–147]. Here, the above mentioned smart materials are classified into 10 classes: piezoelectric, shape memory, magnetostrictive, electrostrictive materials, electrorheological fluids, magnetorheological fluids, polyelectrolyte gels, photostrictive materials, photo-ferroelectric materials, pyroelectrics, magneto-optical materials, and superconducting materials.

1.5.1. Piezoelectric materials

Piezoelectricity is a phenomenon when an electric charge is being generated in a material due to an external mechanical force. Two types of piezoelectric effects are present in today's physics: direct and reverse piezoelectric effects. The direct piezoelectric effect is, actually, the same as the general definition of piezoelectricity. Electric charge is being generated due to the response of a material to a mechanical force. On the other hand, the reverse piezoelectric effect works from the other side:

the electrical potential induces mechanical stresses or strains in a material. Mostly, sensing platforms benefit from the direct piezoelectric effect, while the reverse piezoelectric effect is employed when a precise actuating platform is needed. Piezoelectricity is a first-order effect due to its applicability from the nano- to the milli-scale at a low electric field that produces a strain proportional to the electric field and the direction of the displacement dependent directly on the sign of the electric field [148].

Piezoelectricity can be found in a vast number of natural and synthetic materials. In general, there are four classes: natural crystals, liquid crystals, non-crystalline materials, and synthetic piezoelectric materials. Due to the easier fabrication of synthetic materials and polymers, they are widely used in many sensors and actuators [149].

Zinc oxide (ZnO), aluminum nitride (AlN), and lead zirconium titanate (PZT) are the most common materials used for the sensor industry. Lots of works have been done on ZnO, which was one of the first piezoelectric materials used commercially. ZnO is known for its less demanding vacuum conditions, good film quality, high sputtering rates, and ease of chemical etching. Despite that, ZnO has a high piezoelectric coupling factor, it cannot be widely used in the semiconductor technology due to the increased conductivity, and ZnO also raises issues due to its temperature dependencies.

Aluminum nitride (AlN), on the other hand, is stable under humid and temperature dependent conditions. It is also known for large resistivity and can be perfectly compatible with the processing of metal-oxide-semiconductors. Moreover, AlN has a high quality factor, which makes it useful in resonator applications, and it is denoted by high acoustic velocity. This feature is useful for high-frequency applications. However, AlN lacks electromechanical coupling. Its value is the lowest of the three presently listed materials here.

Extremely high piezoelectric coupling makes PZT the most popular and widely used thin film material. While comparing to ZnO and AlN, PZT exhibits much larger electromechanical coupling, what makes it suitable for energy harvesting applications. Due to the advantages of PZT, many researchers focus their work on developing effective processing methods. PZT can be fabricated by using radio frequency sputtering, screen printing, electron-beam evaporation, ion-beam deposition, magnetron sputtering, and many other techniques [150]. The processing method is selected depending on the application, but all of them focus on two main factors – the layer thickness and the annealing temperatures.

Many works have focused on the creation of the perfect piezoelectric material, which would have a high power factor with minimum energy loss. Despite the research, some of the remaining major concerns are the reduction of hysteresis and an increase of the mechanical quality factor by reinforcing resonance displacement.

1.5.2. Other smart materials

Shape memory materials can be described by their uncommon properties, such as their shape memory effect, high damping capacity, adaptive properties, or pseudo elasticity. As the name states, this kind of material is able to change depending on

the environment it is surrounded by. It can change the shape, position, strain, damping, stiffness, friction, natural frequency or other dynamical or static properties. The change is induced by temperature, mechanical impact, electric stimulus or magnetic field changes.

Electrostrictive materials belong to the category of ferroelectric materials. With the movement of ions in the material, caused by electrostriction, their displacement accumulates, which results in the overall strain (elongation). The consequential strain is proportional to the square of polarization. Materials with a high dielectric constant, such as relaxor ferroelectrics, can expose high electrostrictive constants. The most common materials in this segment are lead magnesium niobate (PMN), lead magnesium niobate-lead titanate (PMN-PT), and lead lanthanum zirconate titanate (PLZT).

The ability to convert magnetic energy into mechanical energy is called magnetostriction. This feature is the main property of magnetostrictive materials. With the help of such advantages as the large magnetomechanical coupling coefficient, large output stress, fast response, high Curie temperature, and high energy density, magnetostrictive materials attract more and more attention from various industry fields. Damping, pneumatics and hydraulics, electrical automation and various other applications are benefiting from magnetostrictive materials and their properties.

Electro and magnetorheological fluids contain micro-sized particles in the carrier liquid. When an external electric or magnetic field is applied, particles develop yield stress. We may thus wonder whether the viscosity of these electro and magnetorheological fluids can be controlled. These fluids can also be categorized into three groups: electrorheological, magnetorheological and ferrofluids. Ferrofluids contain small, nano-sized particles scattered in it. The ferrofluid can be manipulated when a magnetic field is present. These particles align due to the magnetic field; it also helps to increase or decrease the fluid viscosity. The change of viscosity takes only milliseconds, thus the change from liquid to solid, like a Newtonian fluid, is virtually instant. This feature is sought by engineering applications and is very promising for future prospects [151]. Depending on the application, one can choose which energy field is needed. An electrorheological fluid requires a high voltage and low current electric field. On the other hand, a magnetorheological fluid works with a magnetic field which could operate high fluid shear stress that can be generated by a battery. Thus, electrorheological fluids need lots of attention regarding safety. Additionally, magnetorheological fluids are superior due to high shear stresses at the maximum applied field. They also exhibit very low shear resistance at the zero field, chemical inertness, fast response time, temperature stability, and low hysteresis.

The polyelectrolyte gel is a polymer chain with a charged polymer network where macro ions are fixed. Additionally, the material contains micro counter ions which are localized in the network frame. One of the features of the polyelectrolyte gel is the absorption of high amounts of water. The polyelectrolyte gel is affected by the environmental surrounding where pH, the electrical field or the electrical charge alter the physical properties of materials.

Pyroelectric materials possess the ability to instantaneously polarize crystals due to the temperature differential. Pyroelectric materials are only a subgroup of piezoelectric materials. Ceramic materials based on lead zirconate, lithium tantalite, triglycine sulfide, polyvinylidene difluoride and strontium barium niobate are the main pyroelectric materials used in the contemporary scientific and industry projects [152].

There is a wide range of optoelectric/magneto materials. Due to the vast number of possible examples, they are classified into three main groups: photostrictive, magneto-optical, and photo-ferroelectric materials. The first group – photostrictive materials – are mainly used as a sensor or an actuator. The main feature of this kind of material is its working principle which is based on the photovoltaic effect and the converse of the piezoelectric effect. The two other groups can be used as a storage device. Magneto-optical materials exhibit the magneto-optical effect, which is also found in ferromagnetic materials. Due to this phenomenon, data storage based on these materials is denoted by a relatively high Curie point, and no matter how strong magnetic field is applied, it will not affect any stored data. Yet, it is only eligible for temperatures below the Curie point. Photo-ferroelectric materials become relatively polarized when impacted by a light impulse. It also enhances photo-conductivity, shifts ferroelectric phase transition temperatures, causes photo-striction, and may modify the domain structure at the nanoscale level [153].

Superconductivity can be defined by a decrease of resistance due to the vibration ions when the temperature is lowered. Superconducting materials reach the superconductive state when the temperature decreases below a certain value of the critical temperature. Most physical properties of superconducting materials vary depending on the material itself. Such properties as heat capacity, critical temperature, critical field, and critical current density are material dependent and can be different for two different materials.

1.5.3. Piezoelectric composites

Composite materials show improved or elevated properties, and, in some cases, additional functions if compared to single-phase materials. The piezocomposite, consisting of piezoelectric ceramic and a polymer, are this type of a material. It is a promising study field because of the material's excellent tailorable properties.

The geometry for two-phase composites can be classified according to the connectivity of each phase (1, 2, or 3 dimensionally) into 10 structures: 0-0, 0-1, 0-2, 0-3, 1-1, 1-2, 1-3, 2-2, 2-3, and 3-3. If taking an example of a 1-3 piezocomposite, in other words, PZT-rod/polymer-matrix composite is considered most useful [154]. This composite is distinguished by having a high coupling factor, low acoustic impedance, good matching to water or a human tissue, mechanical flexibility, and broad bandwidth in combination with a low mechanical quality factor.

There are three types of composite effects (Fig. 11): the sum effect, the combination effect, and the product effect.

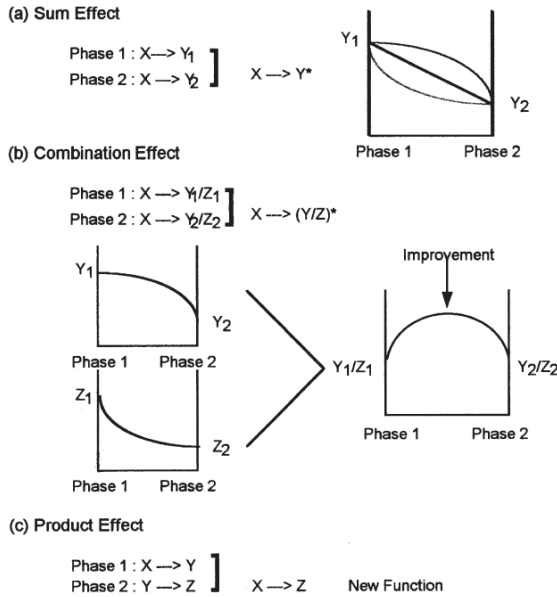


Fig. 11. Composite effects: a) sum, b) combinations, and c) products effects [154]

The sum effect is considered to be present when the composite material has features from all the forming materials. The combination effect takes place when the materials exhibit a specific feature which is then enhanced in the final product. And, finally, the product effect is when a combination of materials creates a completely new feature.

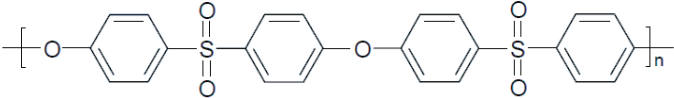
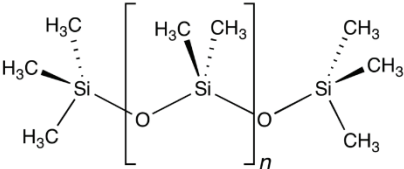
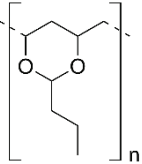
Polymer piezoelectric materials are highly suitable for sensor applications. A polymer itself lacks several properties depending on the materials, such as a small piezoelectric constant, low elastic stiffness, etc. Yet, in combination with PZT, they play a huge role in the design of transducers.

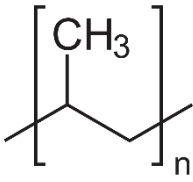
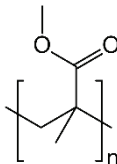
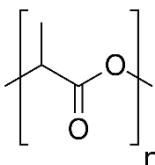
Although there are many different examples of piezoelectric composites (PZT-Epoxy, PZT-Silicone rubber, PZT-Rubber, etc.), all of them come with their own disadvantages. Some of them are rather stiff and brittle, whereas some of them are lacking piezoelectric properties but have good flexibility. In some cases, the material is very promising, but it cannot be used due to high fabrication costs and low applicability. Easy adhesion and strong piezoelectric features are always sought by material scientists around the world.

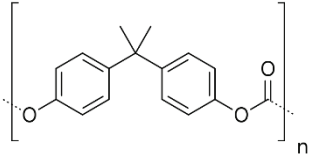
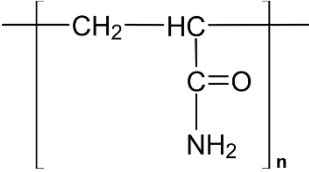
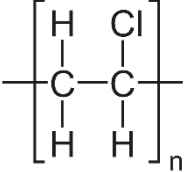
There are many different polymer types which can be used in piezoelectric nanocomposites. Some of them are described in Table 5. The list of polymers given in Table 5 is not an exhaustive list. It is used only to briefly describe the most common polymers used for piezoelectric composites. One can find many different examples in the literature and fabrication.

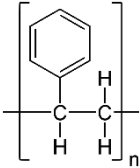
Table 5. Common polymer types for piezoelectric nanocomposites

Polymer	Description
Polyethersulfone	Polyethersulfone – a polymer of the family of thermoplastic polymers (Fig. 12). These polymers are known for their high thermal, oxidative and

Polymer	Description
	<p>hydrolytic stability. In addition, polyethersulfone is amorphous, transparent, and can be thermoformed into shapes.</p>  <p>Fig. 12. Chemical structure of polyethersulfone</p> <p>Polyethersulfone is suitable for medical and food/beverage contact applications due to its ability to be sterilized. It can withstand high temperatures and corrosive media, which makes it suitable for components in batteries, printers, etc. [155]. Polyethersulfone allows easy manufacturing of membranes. Such membranes can be used in various applications, ranging from hemodialysis to gas separation.</p>
Polydimethylsiloxane (PMDS)	<p>PMDS belongs to the family of organosilicon compounds or – as widely referred – silicones (Fig. 13). PMDS is clear, inert, non-toxic, and non-flammable. It is viscoelastic and acts as a viscous liquid in high temperatures. Low temperatures transform it to an elastic solid, similar to rubber.</p>  <p>Fig. 13. Chemical structure of polydimethylsiloxane</p> <p>PMDS is commonly used in soft lithography, where it acts as a stamp resin. Medicine and cosmetics are also an industry field which benefits from PMDS. It is used for over-the-counter drugs, contact lenses or even lubricants [156].</p>
Polyvinyl butyral (PVB)	<p>PVB (Fig. 14) is fabricated from the polyvinyl alcohol reaction with butyraldehyde. The most common uses for PVB are observed when strong binding is needed. Also, there exist applications benefiting from PVB features, such as optical clarity, adhesion to many surfaces, toughness and flexibility.</p>  <p>Fig. 14. Chemical structure of polyvinyl butyral</p> <p>PVB is used for laminated glass production [157]. It can be employed in graphite composites for solar thermal energy storage [158], or even for medical applications [159].</p>
Polypropylene	<p>Polypropylene is a thermoplastic polymer which belongs to the group of polyolefins (Fig. 15). It is very similar to polyethylene. Its density is low, which allows to achieve a lower weight of the produced parts from a</p>

Polymer	Description
	<p>certain mass.</p> <div style="text-align: center;">  </div> <p style="text-align: center;">Fig. 15. Chemical structure of polypropylene</p> <p>It is produced by using hydrocarbon or bulk slurry. Additionally, a gas phase, where gaseous propylene is in contact with the solid catalyst, fabricates solid polypropylene.</p> <p>By using extrusion or molding techniques polypropylene can be used for manufacturing of various parts. Hinges, piping systems, or plastic items for medical or laboratory uses are only a small fraction of all the possible polypropylene applications.</p>
Poly(methyl methacrylate) (PMMA)	<p>Poly(methyl methacrylate) is a transparent thermoplastic often known as acrylic, acrylic glass or plexiglass (Fig. 16). PMMA is cheaper to manufacture if compared to polycarbonate. It features higher tensile strength, flexular strength, transparency, polishability, and higher UV tolerance. Also, PMMA does not contain bisphenol-A, which is a harmful subunit.</p> <div style="text-align: center;">  </div> <p style="text-align: center;">Fig. 16. Chemical structure of poly(methyl methacrylate)</p> <p>PMMA can be used in a wide field of applications. It can be found in the vehicle industry, appliances, lenses of glasses, construction, furniture, etc.</p>
Polyactic acid (PLA) nanofibers	<p>Thermoplastic aliphatic polyester polyactic acid or polyactice (PLA) is fermented from plant, such as corn or sugarcane, starch (Fig. 17). PLA has a glass transition temperature of 60–65 °C, a melting temperature of 173–178 °C, and a tensile modulus of 2.7–16 GPa [160, 161].</p> <div style="text-align: center;">  </div> <p style="text-align: center;">Fig. 17. Chemical structure of polyactic acid</p> <p>PLA is used as a 3D printers' filament material [162]. Packaging is another industry field where manufacturers benefit from PLA. By casting or injection-molding, it is used to make cups and bags [163]. Also, as previously stated materials, PLA is widely used in medical applications. Medical implants, such as anchors, screws, plates, or mesh are fabricated from PLA [164]. It can break down inside the body within 2 years. The</p>

Polymer	Description
<p data-bbox="149 524 291 551">Polycarbonate</p>	<p data-bbox="394 171 1124 247">time interval changes depending on the type of PLA in use. It helps to avoid additional surgeries needed to remove the implanted structural elements.</p> <p data-bbox="394 256 1124 365">Polycarbonates designate a group of thermoplastic polymers which contain carbonate groups in their chemical structure (Fig. 18). Even though polycarbonate is a durable material it does not show a high scratch resistance. On the other hand, it is able to withstand a strong impact.</p> <div data-bbox="602 389 911 547" style="text-align: center;">  </div> <p data-bbox="539 584 973 611">Fig. 18. Chemical structure of polycarbonate</p> <p data-bbox="394 626 1124 815">Many applications are available for polycarbonate. Mostly, it is used for electronic components. Being a good electrical insulator it is used in various products associated with this industry field. Additionally, its properties of heat resistance and flame retardance offer a great impact for electrical solutions. Constructional structures are also extensively fabricated from polycarbonate. And, as well as many other polymers, polycarbonate is also used for medical applications.</p>
<p data-bbox="149 1021 303 1048">Polyacrylamide</p>	<p data-bbox="394 820 1124 930">Polyacrylamide is a polymer formed from acrylamide subunits (Fig. 19). It is high-level water-absorbent, and becomes a soft gel when in touch with water. Polyacrylamide, when in touch with food, can contaminate it with acrylamide which is a well-known neurotoxin and carcinogen.</p> <div data-bbox="602 953 911 1124" style="text-align: center;">  </div> <p data-bbox="533 1148 980 1175">Fig. 19. Chemical structure of polyacrylamide</p> <p data-bbox="394 1190 1124 1248">Mainly, polyacrylamide is used in water treatment. Also, paper making and screen printing benefit from this polymer.</p>
<p data-bbox="149 1448 329 1476">Polyvinyl chloride</p>	<p data-bbox="394 1253 1124 1412">One of the most widely produced synthetic plastic polymers is polyvinyl chloride (Fig. 20). It can be rigid or flexible. This is highly dependent on its application. It is a hard polymer. Its elastic modulus can reach 1500–3000 MPa. With the addition of heat stabilizers, it is possible to increase polyvinyl chloride resistance to high temperatures. The melting temperatures reach 100 °C to 260°C.</p> <div data-bbox="667 1435 851 1607" style="text-align: center;">  </div> <p data-bbox="520 1630 993 1658">Fig. 20. Chemical structure of polyvinyl chloride</p>

Polymer	Description
	<p>Mainly, polyvinyl chloride is used for pipes for municipal and industrial applications. It is also used as insulation for electrical cables. Electrical cables are not the only construction part benefiting from polyvinyl chloride. Being a strong but lightweight plastic, polyvinyl chloride is used as vinyl or vinyl sidings in construction works. It can even substitute wood.</p>
Polystyrene (PS)	<p>Polystyrene is a synthetic hydrocarbon polymer made from monomer styrene (Fig. 21). PS can take two material states – solid or foam. It is a clear, hard, but rather brittle material. It is one of the most widely used plastics. Despite the advantages of PS, it suffers from a relatively low melting point.</p> <div style="text-align: center;">  <p>The diagram shows the chemical structure of a polystyrene monomer unit within a polymer chain. It consists of a benzene ring (a hexagon with a circle inside) attached to a carbon atom. This carbon atom is part of a chain of two carbon atoms, each bonded to two hydrogen atoms. The entire unit is enclosed in large square brackets with a subscript 'n' at the bottom right, indicating it is a repeating unit in a polymer chain.</p> </div> <p>Fig. 21. Chemical structure of polystyrene</p> <p>Polystyrene is widely used in packaging because packing bags for peanuts or protective cases are made from it. Also, containers, lids, bottles, trays, tumblers, and disposable cutlery are made from polystyrene and then used across a broad range of industries.</p>

Addition of various polymers allows modifying some sought-for properties, i.e., a lowered dissipation factor, increased piezoelectric coefficients, the dielectric constant, the loss, etc. Thus, such polymers as PVB [165], polymethyl methacrylate (PMMA) [166], and polystyrene (PS) [167], have shown strong characteristics in microfabrication processes, i.e., strong binding, high adhesion, toughness, flexibility, etc. This interaction of these materials with lead zirconate titanate (PZT) allows changing the main properties of microresonators such as the surface morphology, chemical, optical, electrical, and mechanical properties when seeking to enhance its functionality as well as performance, and to simplify the design and fabrication process.

The search for new piezoelectric nanocomposites was also discussed in the dissertation of Alfredas Brunius titled “Research and development of piezoelectric composite material for biomedical application” [168]. In his thesis, Brunius sought development of high sensitivity, accuracy of measurements properties in a novel material by changing the material ratio of PZT and the polymer. His results have shown that the best properties can be achieved by using 80% of PZT and 20% of the polymer. These results were taken into account and used in this thesis.

1.6. Section conclusions

The following conclusions were drawn from the completed analysis:

- The review of sensors in today’s industry shows a broad number of possible types and their functionality, as well as their applicability to various fields of science and commerce. Pressure sensors are one of the most common types of sensors which are employed in a vast number of

applications. Even though there are many variants of pressure sensors, scientists still are in search for small size, low weight, low cost, high performance, low power consumption, and higher output signal properties of pressure sensors.

- In-depth analysis of sensor elements revealed two possible approaches for the sensing element: cantilevers and membranes. Pressure sensors are primarily based on membranes as their dynamic elements. Membranes can be of various geometry (square, rectangular, and circular shapes) and are capable of high pressure sensitivity. They can also minimize the nonlinearity of a sensor. It is also possible to control geometrical, optical and mechanical parameters of a vibrating membrane across a wide range of oscillation frequency if the suitable material to fabricate the membrane is chosen.
- Material selection for the sensing elements makes a significant impact to its following working properties and performance. Piezoelectric nanocomposites are among the most promising sensing materials as it combines both piezoelectric and polymer properties. From the review of polymers, polyvinyl butyral (PVB), polymethyl methacrylate (PMMA), and polystyrene (PS) have been chosen to create a novel piezoelectric composite due to their strong binding, high adhesion, toughness, and flexibility.

2. PIEZOELECTRIC NANOCOMPOSITE SYNTHESIS AND ANALYSIS

2.1. Synthesis and formation of piezoelectric composite film

The newly proposed piezoelectric nanocomposite material fabrication began with the preparation of powder. Milled PZT powder was mixed together with 3 different bonding materials in order to design the novel composite material. The two components were mixed in 20% to 80% proportions, where 20% of the polymer and 80% PZT were present. PVB in benzyl alcohol, polymethyl methacrylate (PMMA) in benzyl alcohol, and polystyrene (PS) in benzyl alcohol were used as the binding material for the created samples.

The axolate/hydroxide co-precipitation method [169] was used for lead zirconate titanate [$\text{Pb}(\text{Zr}_{0.52}\text{Ti}_{0.48})\text{O}_3$] synthesis. Lead (II) acetate $\text{Pb}(\text{CH}_3\text{COO})_2$, titanium butoxide $\text{Ti}(\text{C}_4\text{H}_9\text{O})_4$, zirconium butoxide $\text{Zr}(\text{C}_4\text{H}_9\text{O})_4$ (80% solution in n-butanol), oxalic acid dehydrate $\text{C}_2\text{H}_2\text{O}_4 \cdot 2\text{H}_2\text{O}$, 25% ammonia solution, and deionized water were used in this procedure as the main materials.

In 100 ml of deionized water, 8.62 g of lead (II) acetate was dissolved. In another glass beaker with 500 ml of deionized water, 32 g of oxalic acid dehydrate was also dissolved. This solution was then heated to 50 °C. Oxalic acid solution was supplemented by 5.1 g of titanium butoxide and 7.65 g of zirconium butoxide 80% solution by dropwise addition. The reaction mixture was vigorously stirred up to the point when a clear yellow solution could be seen. The lead acetate solution was afterwards poured into the solution of titanium and zirconia alkoxides. At the same moment, the pH of the mixed solution had to be adjusted to 9 ÷ 10 by the addition of 25% ammonia solution. The presently explained reaction took additional 60 minutes. During that time, white amorphous precipitation of PZT began to appear. It was filtered under vacuum, then washed with deionized water and acetone, and dried for 12 hours in 100 °C temperature. As the next step, the calcination of the dried powder took additional 9 hours at 1000 °C temperature. The obtained PZT powder was milled. It was then used to prepare the screen-printing paste by mixing it together with 30% solution of PVB in benzyl alcohol, polymethyl methacrylate (PMMA) in benzyl alcohol, and polystyrene (PS) in benzyl alcohol. Three separate mixtures were prepared. As mentioned above, the components in the mixture were calculated to get 20% of binder material and 80% of PZT in the dry coating, i.e., 0.83 g of 30% PVB solution for 1 g of PZT powder. Finally, the viscosity of the paste had to be adjusted to ensure the possibility of screen printing. It was done with a Brookfield viscometer and an ABZ spindle (at 10 rpm and 25 ± 1 °C) to reach 40 ± 5 Pa s of viscosity.

Conventional screen printing was used to apply the created paste to copper foil substrates. Three different types of polyester monofilament screens were used: with 32/70, 48/70, and 140/34 meshes. Then, again, the coatings were dried in an electric oven for 30 min at 100 °C temperature. The fabricated samples (Figs. 22–24) were of high quality and showed strong PZT dominance as shown in Paragraph 2.4.

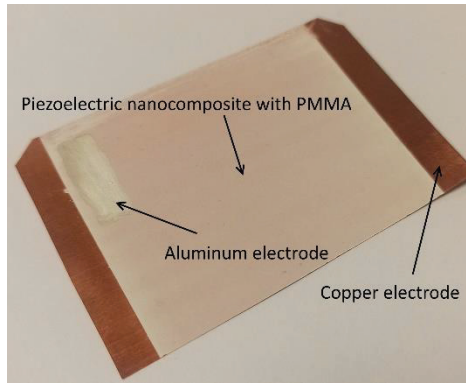


Fig. 22. Fabricated sample with piezoelectric nanocomposite with PMMA

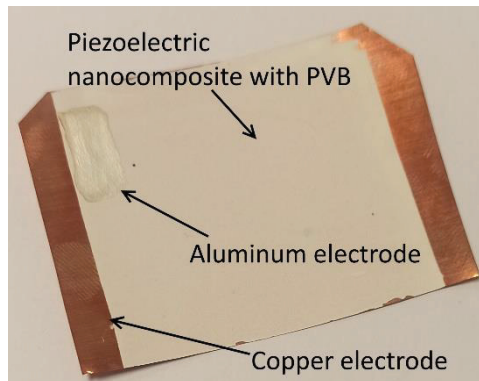


Fig. 23. Fabricated sample with piezoelectric nanocomposite with PVB

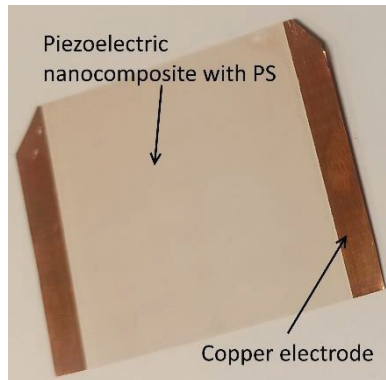


Fig. 24. Fabricated sample with piezoelectric nanocomposite with PS

2.2. Testing methodology and tools

2.2.1. Scanning electron microscopy (SEM)

In order to analyze the synthesized composite material topography and chemical composition, a Scanning Electron Microscope (SEM) *Quanta 200 FEG* was used (Fig. 25). Additionally, this *Quanta 200 FEG* SEM features an integrated

energy dispersive X-ray spectrometer (EDS) detector *X-Flash 4030* which is manufactured by *Bruker Corporation*, USA. SEM is widely used in topography analysis when high amplification is needed. The technical characteristics of *Quanta 200 FEG SEM* are listed in Table 6.



Fig. 25. Scanning electron microscope *Bruker Quanta 200 FEG*

A beam of electrons is concentrated on the sample which has to be analyzed, and it transfers energy to the focused area. The primary electrons attributed to those in the electron beam are used to dislodge electrons from the sample. These dislodged electrons become the secondary electrons (SE). They are magnetized during the process and then collected via a grid or a detector which has a positive potential. Furthermore, these captured electrons are converted into a signal.

The signal conversion to an image through SEM is done by tracing the electron beam across the analyzed area. Then, the signal is amplified to increase the quality and is translated to a surface topography image which could be easily understandable and suitable for further analysis. The number of SE depends on the amount of energy which the primary electrons bring through the electron beam. Additionally, there is direct dependence of the radiance of SE to the energy of primary electrons until a certain limit. If that energy point has been passed, the quantity of SE decreases even though the energy value of the primary electrons increases. This can be explained by the depth of penetration of the primary electron beam. Due to the deep penetration of the beam, the electrons from the furthest points from the surface recombine themselves even before the emission [170].

Three different processes for generating information via SEM are present:

- Images from backscattering electrons (BSE),
- Images generated from emitted secondary electrons (SE),
- Images generated from elemental X-ray mapping.

Table 6. Technical characteristics of *Quanta 200 FEG* scanning electron microscope

Electron source	Field emission gun
Accelerating voltage	500 V–30 kV
Resolution	2 nm at 30 kV (SE)
Imaging detectors	Everhart-Thornley (SE/BSE), Solid State BSE, Large Field, Gaseous SE, Gaseous BSE, Gaseous Analytical and CCD Camera
Imaging modes	High, low vacuum and environmental
Analytical capabilities	Energy dispersive X-rays (Oxford Instruments 80 mm ² X-Max silicon drift detector, MnK _α resolution at 124 eV)

There is an obvious difference between BSE and SE methods.

Two separate dissipation variants are possible: inelastic and elastic. They both occur when a primary electron with high energy interacts with an atom. Inelastic dissipation, though, occurs during the interaction of a primary electron with an atomic electron. On the other hand, elastic dissipation is observed when a primary electron interacts with the nucleus of an atom. Elastic dissipation is also connected with electrons which do not lose the kinetic energy of the atom nucleus. In general conditions, BSE is related with higher than 50 eV energy of the emitted electron, and also the energy values pertaining to this method can be compared to that of the primary beam.

BSE is also connected with the atomic number of the chemical element. The probability of backscattering to occur increases together with the increase in the atomic number of the chemical element. Because of this, BSE can indicate multiple phases of a mixture structure of different materials [171].

On the other hand, SE interacts with the material only several nanometers below the material's surface. During the collision between the primary and the secondary electron, some energy is transferred to the latter. If this energy amount is not sufficient to surpass the energy surrounding it, the electron will be unable to launch itself out through the material's surface. Only when the energy is strong enough, then the emitting electron can be registered as passing the surface area. SE is situated with an energy level lower than 50 eV [172].

2.2.2. Atomic force microscopy (AFM)

Atomic force microscopy (AFM) is a type of scanning probe microscopy (SPM) with a resolution level in the order of nanometers. It is based on the cantilever/tip assembly that interacts with the sample. This assembly is called the probe. The raster scanning motion, which is up/down and side-to-side motion of the AFM tip as it scans the surface, is the method by which AFM interacts with the sample. Scanning along the surface is monitored by the reflection of a laser beam off the cantilever. This beam is traced by a position sensitive photo-detector which can determine vertical and lateral motion. AFM has three major features: force measurement, imaging, and manipulation.

Force measurement employs AFMs to measure the forces between the probe and the sample as a function of their mutual separation. This can be used to measure the mechanical properties of the sample, such as the sample's Young's modulus.

Imaging is used to form a topography image of the sample surface at a high resolution. This is completed by scanning the position of the sample with respect to the tip of the probe and recording the height of the probe that corresponds to the constant probe-sample interaction. In addition, other properties of the sample can be measured locally and displayed as an image. Mechanical properties, such as stiffness or adhesion strength, and electrical properties, such as conductivity or surface potential, can be analyzed and plotted by AFM.

During the manipulation, it is possible to change the properties of the sample in a controlled way by using the forces between the probe tip and the sample. Such applications as scanning probe lithography and local stimulation of cells benefit from this approach.

To analyze the mechanical properties of the samples, a *JPK NanoWizard 3* AFM was used (Fig. 26). *JPK NanoWizard 3* was developed by the same company as the SEM *Quanta 200 FEG*, i.e., *Bruker*, USA.



Fig. 26. Atomic force microscope *JPK Nanowizard 3*

AFM can be used in a wide range of natural science fields including solid-state physics, semiconductor science and technology, molecular engineering, polymer chemistry and physics, surface chemistry, molecular biology, cell biology, and medicine.

Its applications include the identification of atoms at a surface [173], determination of mechanical properties [174], or even medical applications where normal and cancerous cells can be differentiated [175].

2.2.3. Energy dispersive X-ray spectroscopy (EDS)

Energy dispersive X-ray spectroscopy (EDS) is an analytical method of sample analysis and characterization. An excited X-ray is interacting with a sample, which provokes a unique element to emit its electromagnetic emission spectrum. As each chemical element is unique with its own atomic number and structure, this allows to

clearly differentiate each of them with their unique set of peaks. As low as 0.001 percent concentration can be detected by EDS. This analysis is a non-destructive method which is used for solving a variety of physico-chemical problems across a broad spectrum of industries [176].

To cause the emission of the electromagnetic energy spectrum, the sample has to be bombarded with a high-energy beam (electrons or protons), or concentrated X-ray. Before the excitation, during the unexcited state of an atom, all of its structure follows its own path. All atoms have electrons only on specific levels, and electrons are bound to the atomic nucleus. The electron shell, which is the closest to the nucleus, is designated as the K shell, and the following shell is the L shell. The other subsequent shells are also noted by Latin alphabet letters. During excitation, electrons also become excited, which causes them to leave their regular position and either to eject from their space, or to take over another electron position. Electrons from the outer shell fill in the missing position and, with that, they emit the energy difference. This energy is released in the form of X-ray. These X-ray lines are noted by the Latin alphabet letter which indicates the shell containing the vacancy of the electron. Additionally, a Greek letter (α , β , etc.) specifying the intensity of the group to which the line belongs (Fig. 27), is used. These released X-ray beams are registered in the emission spectrum with an energy-dispersive spectrometer.

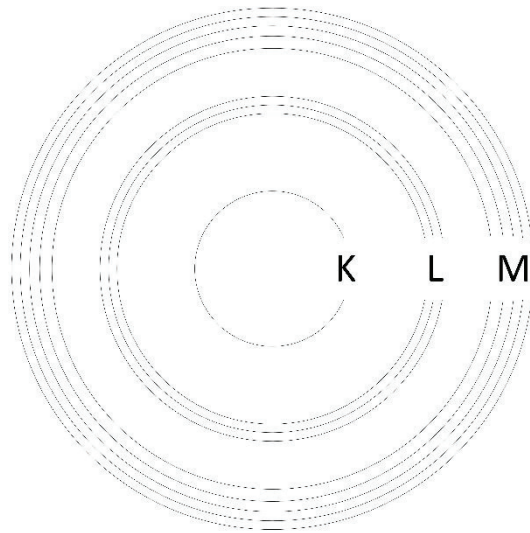


Fig. 27. X-ray characteristic lines

In order to calculate the numerical value of the energy difference when electrons shift from one shell to another, it is possible to use Equation (2.2.2.1) [177].

$$E_{\gamma} = E(n_i) - E(n_f) = 13.6 \cdot (Z - s)^2 \left(\frac{1}{n_f^2} - \frac{1}{n_i^2} \right), \quad (2.2.2.1)$$

where n_i – initial principle quantum number, n_f – final principle quantum number, s – screening factor, and Z is the atomic number.

During the analysis, SEM with an integrated dispersive X-ray spectrometer detector was used. The whole unit is presented in Fig. 26. The energy dispersive X-ray spectrometer detector *X-Flash 4030* is presented in Fig. 28.



Fig. 28. Energy dispersive X-ray spectrometer *X-Flash 4030* [178]

During the analysis, this 30 mm² modern solid state drift detector was cooled with a Peltier element. The detector was capable to provide 133 eV (at MnK α) energy resolution at 100000 cps. The technical data of the *X-Flash 4030* detector is given in Table 7.

Table 7. Technical data of *X-Flash 4030* detector

Technical data	Value and description
Energy resolution	133 eV (Mn K α) guaranteed at 100000 cps, stable over whole throughput range at a given shaping time
Max. pulse load	1000000 cps
Active area	30 mm ²
Detection range	From Boron (5) to Americium (95)
Cooling	Peltier cooling (no liquid nitrogen or other cooling agents required)
Weight	Low weight (approx. 2.5 kg)

2.2.4. Fourier transform infrared spectroscopy (FTIR)

Fourier transform infrared spectroscopy is an analysis method which allows registering infrared spectra. The infrared light passes through the interferometer and then through the sample. Additionally, a moving mirror in the inside of the interferometer changes the amount of light passing through the machine. The recorded signal that shows the light output as a function of the mirror position is called the interferogram. By using the Fourier transform technique, the gathered data is remastered to the sought spectra which represent the light output as a function of infrared wavelength.

Analytical calculations for extracting the spectrum from the sample are based on the following calculations of the total intensity (the function of the path length difference) at the detector (Equation (2.2.3.1))

$$I_p = \left(p, \int_0^\infty I(p, \tilde{\nu}) d\tilde{\nu} \right) = \left(p, \int_0^\infty I(\tilde{\nu}) [1 + \cos(2\pi\tilde{\nu}p)] d\tilde{\nu} \right), \quad (2.2.3.1)$$

where p is the path length difference in the interferometer, $\tilde{\nu}$ is the wavenumber, and $I(\tilde{\nu})$ is the spectrum to be determined. The previously stated formula is applicable for any desired values of p [179].

FTIR can be used to analyze and identify chemicals. A major advantage of this technique is that the analyzed samples can be of any material phase – solid, liquid, or gas. FTIR analysis is widely used in organic and inorganic chemistry. This helps to implement it in various industry fields. It can be used to identify and measure the concentration of various compounds in various food products in the food industry [180, 181]. Another example of its application lies in the field of semiconductor microelectronics, where FTIR can be applied to silicon, silicon nitride, etc. semiconductors [182]. Additionally, FTIR has already been used for some time in art analysis, where pigments identification is needed in paintings [183], other art objects [184], or illuminated manuscripts [185].

The total infrared regions are in the 12800–10 cm^{-1} wavelength and can be split into three smaller intervals: 12800–400 cm^{-1} , which is near the infrared region, 4000–200 cm^{-1} , which is the middle of the infrared region, and 1000–50 cm^{-1} , which is the far infrared region. Various spectrometers work in the stated infrared regions.

FTIR *Vertex 70* is made by the same company as mentioned above, i.e., *Bruker*, USA (Fig. 29).

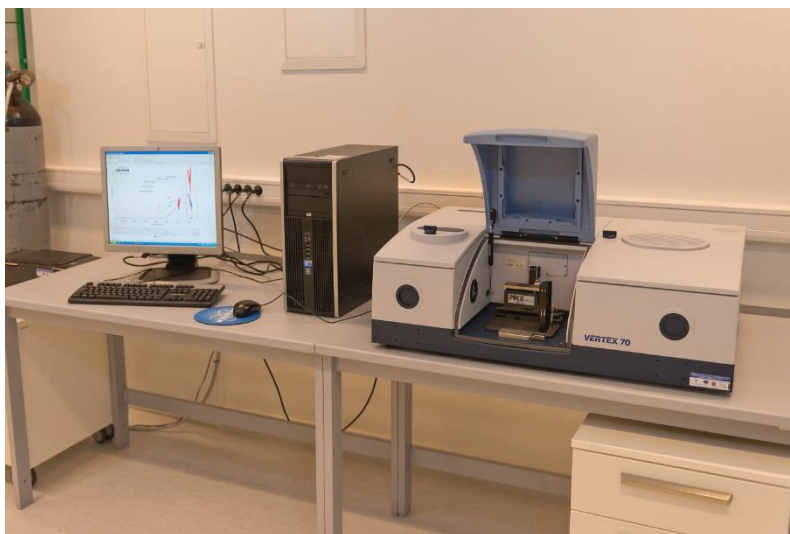


Fig. 29. Fourier transform infrared spectrometer *Vertex 70*

Some technical characteristics of FTIR is given in Table 8.

Table 8. Technical characteristics of Fourier transform infrared spectrometer *Vertex 70*

Technical characteristic	Value and description
Spectral range	Mid-IR, NIR, Far-IR/THz, Visible/UV 10 cm^{-1} to 28000 cm^{-1} (360 nm)
Spectral resolution	Better than 0.4 cm^{-1} (apodized), optional 0.16 cm^{-1}
Input ports	Up to 2
Output ports	Up to 5
Rapid scan	>70 spectra/sec at 16 cm^{-1} spectral resolution
Slow scan & step scan	100 Hz (0.0063 cm/sec), Phase modulation and internal demodulation, Temporal resolution $6\text{ }\mu\text{sec}/2.5\text{ nsec}$

2.2.5. Keithley meter scanner

The piezoresistive characteristics of the fabricated samples were investigated with an 8½-Digit High Performance Multimeter from *Keithley 2002* series, manufactured by *Tektronix*, USA (Fig. 30).

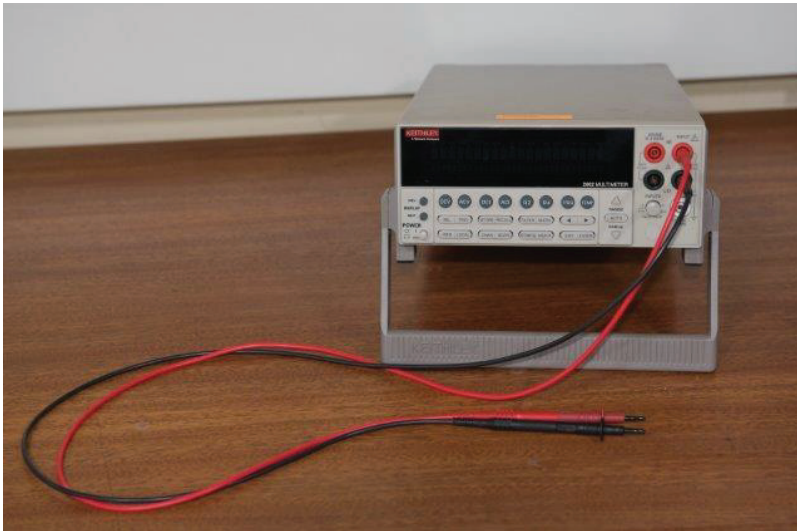


Fig. 30. Keithley 2002 Series 8½-Digit High Performance Multimeter

With the use of this precision multimeter, it is possible to complete various types of electric unit measurements. It can be direct or alternating current, voltage, resistance, or frequency. It is also possible to analyze the temperature. All the analyses use the approach of mathematical functions (averages, spread, polynomial calculations, etc.).

In order to analyze the piezoresistive characteristics of the samples (Fig. 31), the following experimental setup was created:

The experimental setup consisted of a sample tested in the direct piezoelectric mode applying single hits, excitation, a measurement system, and a data acquisition device, i.e., this method investigates the changes of resistance and/or voltage when force F is applied to the surface of the sample, and after it is released (the reverse piezoelectric effect) (Fig. 32). The applied mechanical energy to the piezoelectric layer was converted into electrical energy due to layer deformation.

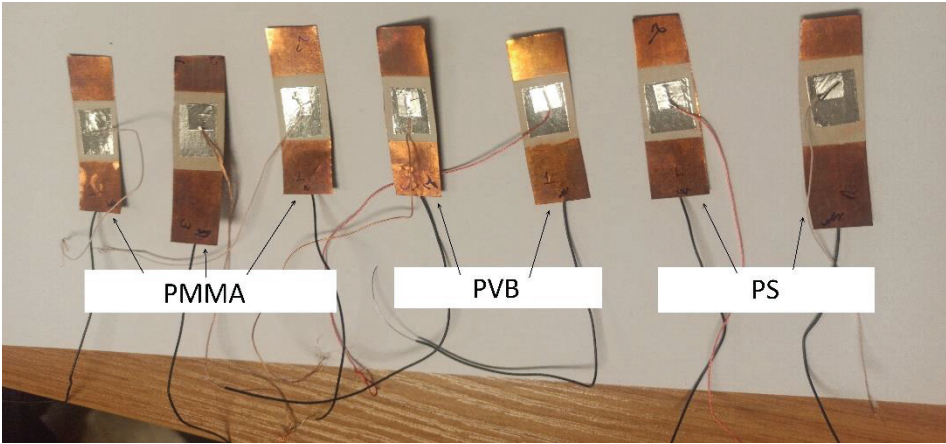


Fig. 31. Prepared samples for analysis of piezoresistive characteristics

Operational conditions were examined during this analysis, and they were compared with the other samples.

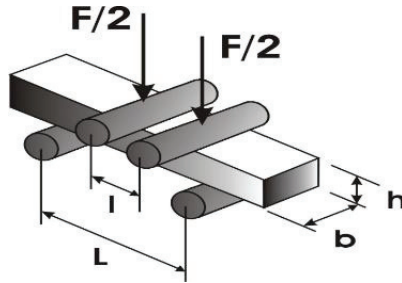


Fig. 32. Schematics of analysis of piezoresistive characteristics

A gauge factor (GF) (the ratio of the relative change in electrical resistance R versus mechanical strain ε) here was calculated according to Equation (2.2.4.1) given below [186]:

$$GF = \frac{\Delta R/R}{\Delta L/L} = \frac{\Delta R/R}{\varepsilon} = 1 + 2\nu + \frac{\Delta\rho/\rho}{\varepsilon} \quad (2.2.4.1)$$

The material's ability to demonstrate a strong piezoresistive effect is affected by strain, which is stated by adding the $\frac{\Delta\rho/\rho}{\varepsilon}$ term. Otherwise, the change of resistance would only be based on geometric terms.

The mechanical strain ε was then calculated [186] (Equation (2.2.4.2):

$$\varepsilon = \frac{\Delta l}{l} = \frac{3F(L-l)}{2bh^2E} \quad (2.2.4.2)$$

The units in Equation (2.1.2.4.1) and Equation (2.1.2.4.2) are explained as follows: ΔR is the resistance change due to the strain, R is the initial resistance, ΔL is the change in length, L is the original length of the wire or foil, and $\Delta L/L$ is the unit

strain to which the sample is subjected, ν is Poisson's ratio, ρ is the resistivity, while h is the sample height, and b the sample width.

A negative gauge factor indicates that resistance decreases when the applied strain is increased and vice versa.

2.2.6. Laser triangulation sensor LK-G3000 and PicoScope 3424 oscilloscope

A laser triangular displacement sensor *LK-G3000* developed by *Keyence*, Illinois, USA, was used for the analysis of dynamic and electric characteristics of all the three samples. This sensor is assembled of a sensor head *LK-G82* (Fig. 33) and a control block *LK-G3001P* (Fig. 34). The LK series sensor enables the measurement of multicolored or patterned targets. Also, no additional adjustment is needed to measure low reflectance targets, such as black rubber.



Fig. 33. *LK-G82* sensor head [187]



Fig. 34. *LK-G3001P* control block [188]

Technical characteristics of the *LK-G82* sensor head and the *LK-G3001P* control block are given in Table 9 and Table 10, respectively.

Table 9. Technical characteristics of *LK-G82* sensor head

Technical characteristic	Value and description
Reference distance	Diffused reflection: 80 mm Specular reflection: 75.2 mm
Measuring range	Diffused reflection: ± 15 mm Specular reflection: ± 14 mm
Light source type	Red semiconductor laser
Light source wavelength	650 nm
Light source laser class	Class II (FDA CDRH 21CFR PART1040.10)
Light source output	0.95 mW
Linearity	$\pm 0.05\%$ of F. S. (F. S. = ± 15 mm)
Repeatability	0.2 μm
Ambient temperature	0 to +50 $^{\circ}\text{C}$

An LK series sensor was used to measure the piezoelectric properties of the fabricated samples. The employed experimental setup for the measurement of piezoelectric properties is given in Fig. 35.

Table 10. Technical characteristics of LK-G3001P control block

Technical characteristic	Value and description
Analog voltage output	$\pm 10 \text{ V} \times 2$
Analog current output	$4 \text{ to } 20 \text{ mA} \times 2$
Power voltage	$24 \text{ VDC} \pm 10\%$
Current consumption	500 mA or less
Ambient temperature	0 to $+50 \text{ }^\circ\text{C}$

The experimental setup consists of three main systems: a piezoelectric element, excitation device, and a measurement system with connection to the data analysis software. Excitation is mainly generated by an electromagnetic shaker which excites the clamped sample.

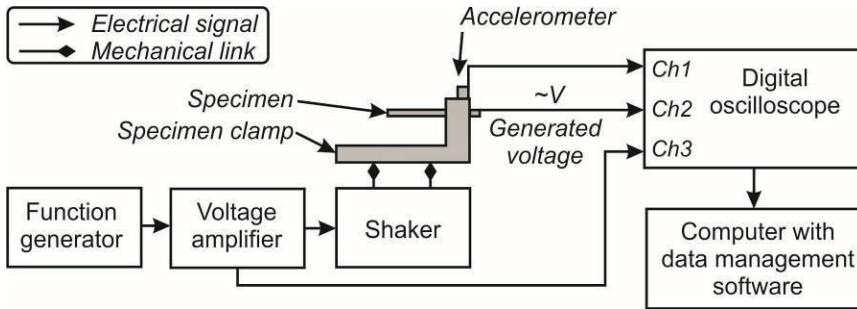


Fig. 35. Experimental setup for measurement of piezoelectric properties [189]

The signal of harmonic excitation is transferred to the shaker and is controlled by an *AGILENT 33220A* function generator through a voltage amplifier *VPA3100MN* from *HQPower*. Acceleration at the top of the clamp was measured by a single axis miniature accelerometer *KD-35*. Its working frequency range is from 5 Hz to 5 kHz, and the sensitivity reaches $50 \text{ mV/g} \pm 2\%$. The retrieved experimental data from the accelerometer, the sample, and the voltage amplifier was collected by a 4 channel oscilloscope (analogue to a digital converter) *PICO 3424*, which also forwarded the information to the computer. *Picoscope 6* software processed the raw data from *PICO 3424*, which helped to generate the graphical data and obtain the final results. The experimental setup is given in Fig. 36.

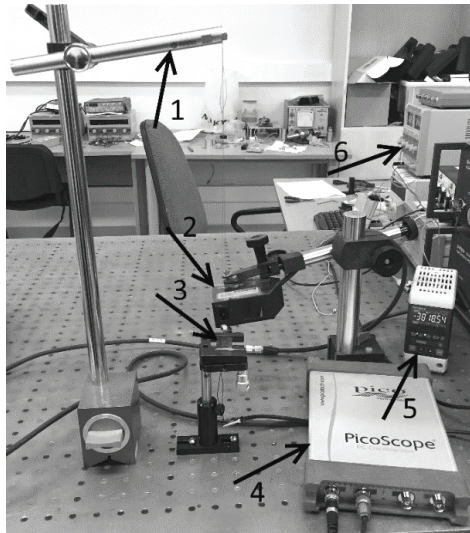


Fig. 36. Experimental setup for piezoelectric response measurement: (1) pendulum, (2) *LK-G82* sensor head, (3) sample, (4) *PicoScope* oscilloscope, (5) *LK-G3000* control block, and (6) power supply block

The technical characteristics of the *PICO 3424* oscilloscope are given in Table 11.

Table 11. *PICO 3424* oscilloscope technical characteristics

Technical characteristic	Value and description
Voltage accuracy	1%
Maximum sampling rate	20 MS/s
Buffer memory	512 kilo sample, captures long, complex waveforms at high speed
Measuring range	± 20 Mv TO ± 20 V

2.2.7. Electronic speckle pattern interferometry system *PRISM*

The mechanical response of the samples caused by electrical excitation was evaluated by the electronic speckle pattern interferometry system *PRISM* fabricated by *Hytec Company*, USA (Fig. 37). During the analysis, the resonant frequency of the sample was analyzed. The system *PRISM* allows measuring the vibrations and deformations of the sample with only an insignificant preparation of the sample. Also, there is no direct contact between the sample and the system *PRISM*. This helps to avoid possible sample violations or destruction. The measurement sensitivity of the *PRISM* system is less than 20 nm, while the measurement range exceeds the 100 μ m range.

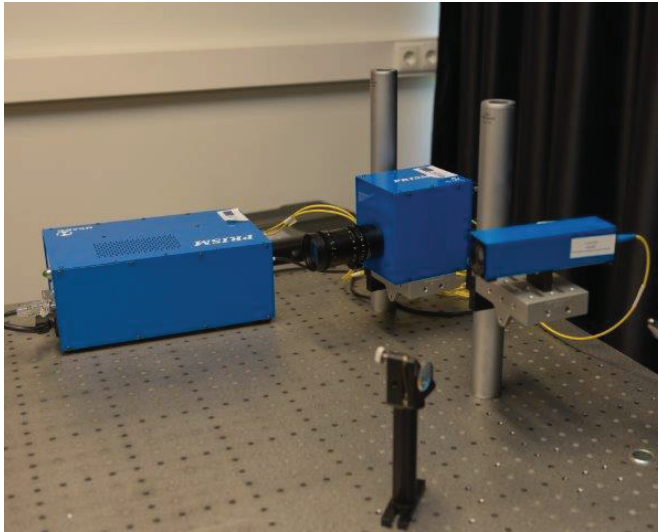


Fig. 37. Electronic speckle pattern interferometry system *PRISM*

The experimental setup for electrical excitation response measurement was constructed as follows. Green laser light (532 nm, 20 mV) was used for the measurements. The laser beam directed to the object is called the object beam. A laser beam directed to the camera is called the reference beam. In Fig. 38, the laser beam directed at the object and the reference beam goes directly to the camera. Laser light is scattered from the object and collected by the camera lens which images the object onto CCD camera sensors. The image is then sent from the camera to the computer, where it is analyzed with *PRISM DAQ* software. This *PRISM* setup can also be defined as a high-speed holographic technique. The used samples are presented in Figs. 39–41.

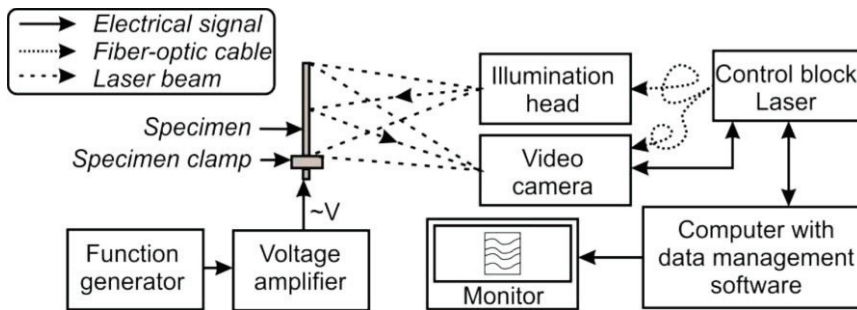


Fig. 38. Schematic view of the experimental setup for *PRISM* system

This technique can be applied to several applications where nondestructive testing of objects is required. Its universality has increased with the advances in coherent light sources and their calculations, detector technologies, and imaging [190, 191]. The technical properties of this kind of system allow exploring this methodology in the micrometric setup for MEMS analysis in terms of their structure and fabrication materials [192].



Fig. 39. Prepared sample for *PRISM* system analysis with PMMA



Fig. 40. Prepared sample for *PRISM* system analysis with PVB

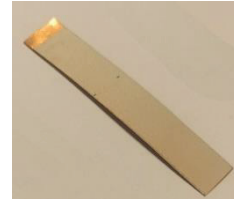


Fig. 41. Prepared sample for *PRISM* system analysis with PS

2.2.8. Voltage standing wave ratio (VSWR)

The voltage standing wave ratio (VSWR) methodology was used to measure the sheet resistance of the sample. A *P2-67 VSWR* meter was used which was fabricated by *RF* and *CIS* from Moscow, Russia. The technical characteristics of the *P2-67 VSWR* meter are listed in Table 12.

Table 12. Voltage standing wave ratio meter *P2-67* technical characteristics

Technical characteristic	Value and description
Frequency range	12.05–17.44 GHz
Cross section of waveguide paths	16 × 8 mm 17 × 8 mm
Measurement limits	KSVN 1.06–5
Attenuation	-35 ... 0 dB
Accuracy	0.5%

The voltage standing wave ratio can be calculated first by calculating the reflection coefficient with Equation (2.2.7.1) [193]

$$\Gamma = \frac{V_{ref}}{V_{fwd}}, \quad (2.2.7.1)$$

where V_{ref} is the magnitude of the reverse wave of DC voltage, and V_{fwd} is the magnitude of the forward wave of DC voltage.

The actual voltage as a function consists of a sine wave at frequency ν with the magnitude and phase of the complex voltage function. According to the superposition principle and the standing wave pattern theory, the net voltage present at any point on the transmission line is equal to the sum of the voltages of the forward and reflected waves. As the net voltage varies in time, the max and min values are the ones to consider. In order to find out the values, it is needed to calculate the squared magnitude of the net voltage. The following Equation (2.2.7.2) represents the complex mathematical function of the net voltage squared magnitude which then translates to a fairly simple Equation (2.2.7.3) by replacing and simplifying some of the terms.

$$|V_{net}(x)|^2 = V_{net}(x)V_{net}^*(x) = e^{-ik(x-x_0)}(1 + \Gamma e^{i2k(x-x_0)})Ae^{+ik(x-x_0)}(1 + \Gamma^* e^{-i2k(x-x_0)})A^* = [1 + [\Gamma]^2 + 2\mathcal{R}(\Gamma e^{i2k(x-x_0)})]|A|^2, \quad (2.2.7.2)$$

where x is the position along the transmission line, x_0 is the end of the transmission line where the load is located, k is the wavenumber due to the guided wavelength along the transmission line, Γ is the reflection coefficient, A is the amplitude, and \mathcal{R} represents the real part of the term. Then, the following Equation (2.2.7.3) can be used to calculate the voltage standing wave ratio [192]

$$VSWR = \frac{|V_{max}|}{|V_{min}|} = \frac{1+\Gamma}{1-\Gamma}, \quad (2.2.7.3)$$

where V_{max} is the max voltage, V_{min} is the minimal voltage, and Γ is the reflection coefficient. Mostly, VSWR is used when installing and tuning transmitting antennas [194]. Although it could have a significant impact for medical applications, it does have a major impact on the performance of microwave-based medical devices. Microwave electrosurgery is one of those applications where the presence of the standing wave ratio can impact the reliability of the devices in use [195].

2.2.9. Microhardness measurement

Microhardness, or indentation hardness, analysis is the analysis of the hardness of a material to deformation. Macroscopic and microscopic scale analysis can be performed by indenting the material until the surface forms an impression. In some cases, hardness can also be measured linearly to the tensile strength of the material [196].

Two classes of microhardness tests are established: microindentation and macroindentation. They differ by the forces in use. Less than 2 N corresponds to microindentation, and a higher force corresponds to macroindentation. Both of these classes of analysis have the advantage of no or low level surface finish. The surface finish does not have an effect on the hardness measurement, although the scratch or the indentation has to be large compared to the surface roughness [197].

Various microhardness tests are available:

- Vickers hardness test (HV)
- Brinell hardness test (HB)
- Knoop hardness test (HK)
- Janka hardness test
- Meyer hardness test
- Rockwell hardness test
- Shore hardness test
- Barcol hardness test.

In this thesis, the HV test was used. It involves the same basic principles: the target is to analyze a material's ability to resist plastic deformation from a standard source. It can be used for all metals and has one of the widest scales of all tests. The

achieved result is the Vickers Pyramid Number (HV). The HV number is determined by the ratio of the force applied to the diamond (the indenter) and the surface area of the resulting indentation. By using Equation (2.2.8.1), the Vickers Pyramid Number can be calculated:

$$HV \approx \frac{F}{A} \approx 0.1891 \frac{F}{d^2}, \quad (2.2.8.1)$$

where F is the force applied to the diamond, A is the surface area of the resulting indentation, and d is the average length of the diagonal left by the indenter. The surface area of the resulting indentation depends on the indenter diamond angles and can be calculated by Equation (2.2.8.2):

$$A = \frac{d^2}{2\sin(136^\circ/2)}, \quad (2.2.8.2)$$

where d is the average length of the diagonal left by the indenter. Additionally, the Martens hardness (HM) test was implemented. The HM test can also be named the Hardness Under Test Force. Whereas the HV test is evaluated only after the force has been removed, the HM test follows the effect of elastic deformation under the indenter [198]. The analytical background of the HM test is similar to the HV test.

The samples were measured by using a dynamic microhardness meter with *HM 2000S* base devised by *Fischer*, Lymington, UK (Fig. 42).



Fig. 42. *Fischerscope HM 2000S* microhardness meter

Dynamic microhardness meter can analyze various mechanical and elastic properties of materials. With the advantage of its easy-to-handle construction and sample positioning, it is suitable for evaluating such material parameters as HV or HM.

2.2.10. Micro-scratch tester MST^3

Adhesion failure of the designed coatings was tested with a micro-scratch tester MST^3 made by *Anton Paar GmbH*, Germany (Fig. 43). The *Anton Paar* device allows making reliable measurements even on curved or uneven surfaces.



Fig. 43. Micro-scratch tester MST^3 [199]

The technical characteristics of micro-scratch tester MST^3 are given in Table 13. Some of the typical applications for this kind of tester vary from automobile bumper paint adhesion testing to thermal/plasma spray coatings testing. The stated noise floor value is specified under ideal laboratory conditions when using an anti-vibration table.

Table 13. Technical characteristics of micro-scratch tester MST^3

Technical characteristic	Fine range	Large range
Maximum penetration depth, μm	100	1000
Depth resolution, nm	0.05	0.5
Noise floor, rms	1.5	
Maximum normal load, N	10	30
Load resolution, mN	0.01	0.03
Noise floor, rms	100	
Maximum friction load, N	10	30
Resolution friction load, mN	0.01	0.03

To determine the adhesion of the coatings which would ensure a long lifetime of surface adherence to the substrate, the following methodology was used. A *Rockwell* type diamond indenter (*AD-295*) with a $200\ \mu\text{m}$ radius was used. The given load was $0.02\ \text{N}$, which was increased in $0.02\ \text{N}$ steps until reaching $6\ \text{N}$. The loading rate was $11.96\ \text{N}/\text{min}$.

2.3. Structural Composition

Three samples were manufactured with PZT, and three separate binding materials (PVB, PMMA, and PS) were used. Fig. 44 shows the SEM picture of every sample. A relatively even surface was registered in the sample with the PVB binder which only had small pileups of particles ranging from 10 to 20 μm diameter on the top (Fig. 44a). The PMMA-bonded PZT sample showed the smoothest surface of these three samples. Only diminutive pileups of particles were registered which reached only up to 5 μm diameter on the surface of the sample. The pileups also appeared very seldom (Fig. 44b). The last sample, PZT with the PS binder, looked similarly to the first sample, PZT with PVB. Here, pileups from 5 to 15 μm diameter particles were found (Fig. 44c). This analysis showed that the best result of the surface finish was registered in the sample with a PMMA bonding material. This can be explained by the bonding material loading into the PZT matrix. This caused the irregular shape and nucleation, as well as growth in the solution. The bonding material PMMA due to the previously stated conditions formed much smaller grain and generally developed a smoother and flatter surface by comparing it to the sample of PVB with PZT and PS with PZT.

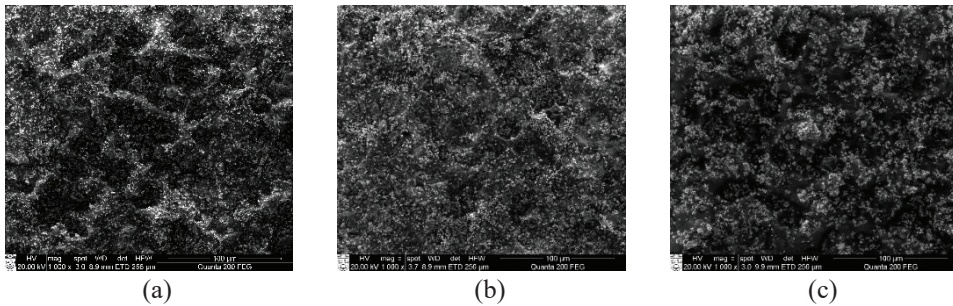


Fig. 44. Sample views in SEM: PZT with PVB polymer (a), PZT with PMMA polymer (b), and PZT with PS polymer (c)

2.4. Chemical Composition

By using the EDS with pulse height analysis, the chemical composition of all the three samples was investigated. Ionization caused by incident X-Ray photons created an electrical charge. In the following EDS spectrum, the x axis shows the X-Ray energy in channels 1–6, while the y axis represents the number of counts per channel, from 0 to 6 keV and up to 18 cps/keV, respectively. Carbon (C), Oxygen (O), Titanium (Ti), Zirconium (Zr), and Lead (Pb) were found in all the three samples. These spectra are presented in Fig. 45.

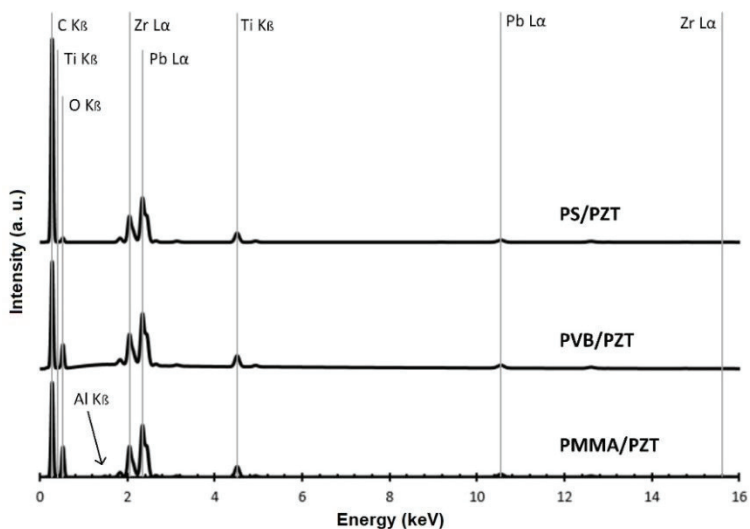


Fig. 45. Energy dispersive spectra of PMMA/PZT, PVB/PZT, and PS/PZT samples

The Carbon K_{β} peak was registered at about 0.2 keV for PVB/PZT sample. Energy resolution of the Oxygen (O) K_{β} peak was approximately at 0.5 keV. The Titanium K_{β} energy resolution peak was specified at two positions – 0.3 keV and 4.5 keV. Zr L_{α} showed energy resolution peaks at two positions as well. They were registered at 2.1 keV and 15.8 keV. Lead (Pb) was also registered twice. The first peak for Pb L_{α} was at 2.4 keV, and the second peak was at 10.5 keV. The map of the distribution and the relative proportion of the chemical elements over the scanned area is presented in Table 14 and Fig. 46.

Table 14. Chemical characterization of PVB/PZT sample

Element	C	O	Ti	Zr	Pb	Sum
Series	K	K	K	L	L	
Normalized Concentration (norm. wt.%)	42.24	31.81	3.35	7.82	14.79	100
The Atomic Weight Percent (norm. at.%)	61.36	34.68	1.22	1.49	1.24	100
Error in the Weight Percent Concentration (%)	5.51	33.64	0.13	0.36	0.57	-
Figure	Fig. 46a	Fig. 46b	Fig. 46c	Fig. 46d	Fig. 46e	-

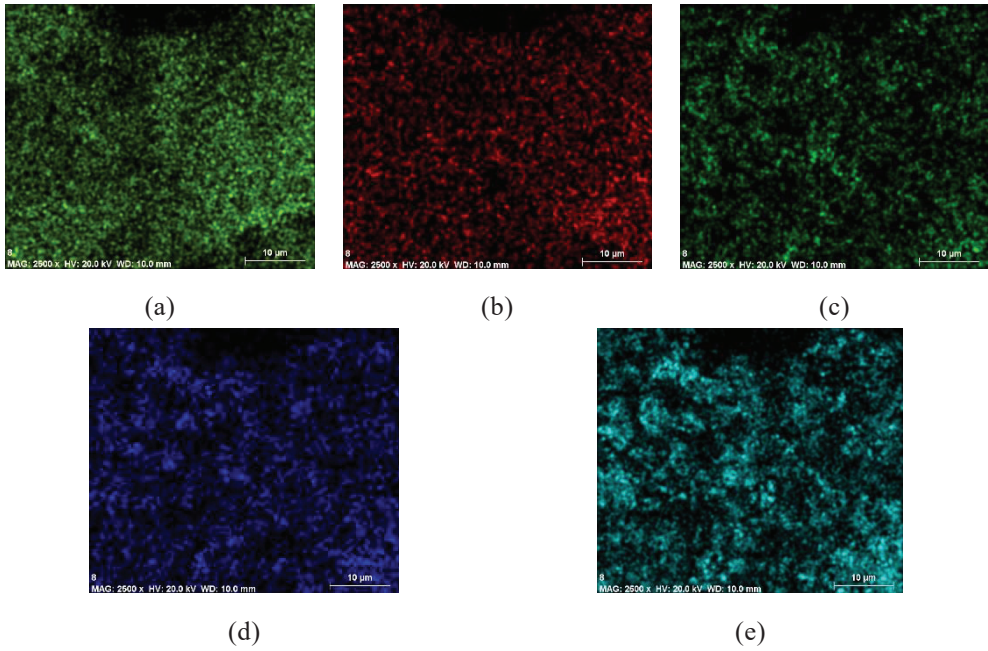


Fig. 46. Relative proportion (intensity) and distribution maps of PVB/PZT samples

Following the energy dispersive spectra of the PMMA/PZT sample in Fig. 45, the Carbon K_{β} peak was registered at about 0.2 keV. The energy resolution of the Oxygen K_{β} peak was approximately at 0.5 keV. The Titanium K_{β} energy resolution peak was specified at two positions – 0.4 keV and 4.5 keV. Zr L_{α} showed energy resolution peaks at two positions as well. They were registered at 2.1 keV and 15.8 keV. Lead (Pb) was also registered twice. The first peak for Pb L_{α} was at 2.4 keV, and the second peak was at 10.5 keV. Both samples showed almost identical values in the energy dispersive spectra, although here Aluminum (Al) element also appeared. Its small peak was registered in the region of 1.4 keV energy. A map of the distribution and relative proportion of chemical elements over the scanned area is presented in Table 15 and Fig. 47.

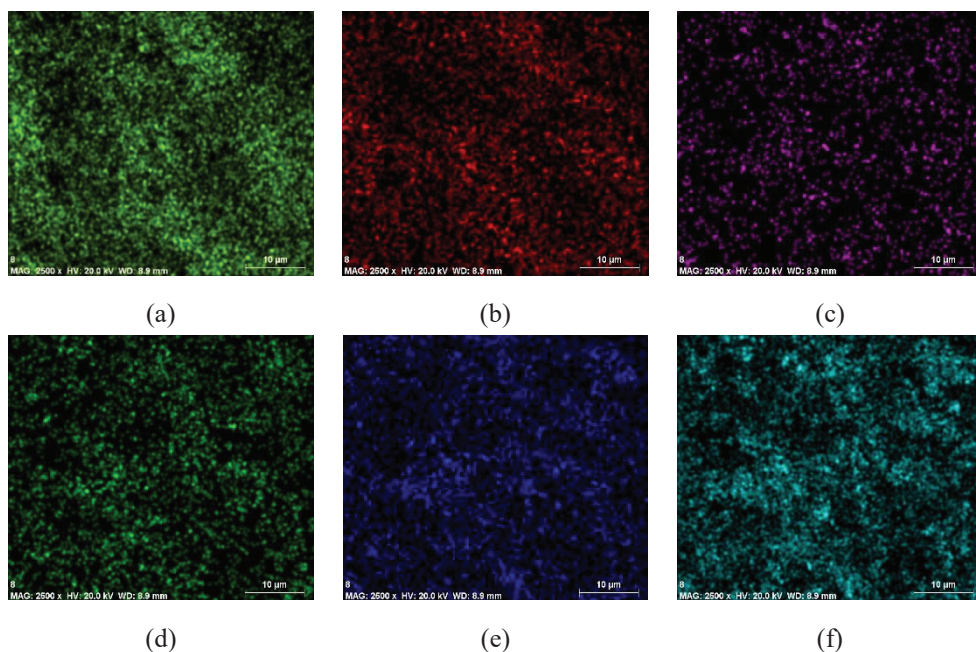


Fig. 47. Relative proportion (intensity) and distribution maps of the PMMA/PZT sample

Table 15. Chemical characterization of the PMMA/PZT sample

Element	C	O	Ti	Zr	Pb	Al	Sum
Series	K	K	K	L	L	K	
Normalized Concentration (norm. wt.%)	37.38	35.56	3.17	8.05	15.71	0.14	100.00
The Atomic Weight Percent (norm. at.%)	55.88	39.90	1.19	1.58	1.36	0.09	100.00
Error in the Weight Percent Concentration (%)	5.07	34.41	0.13	0.38	0.62	0.04	-
Figure	Fig. 47a	Fig. 47b	Fig. 47c	Fig. 47d	Fig. 47e	Fig. 47f	-

The energy dispersive spectra of the PS/PZT sample in Fig. 45 shows slightly different results than the two samples before. The Carbon K_{β} peak was registered at about 0.2 keV. The energy resolution of the Oxygen K_{β} peak was approximately at 0.4 keV. The Titanium K_{β} energy resolution peak was specified at two positions – 0.4 keV and 4.5 keV. Zr L_{α} showed its energy resolution peaks at two positions as well. They were registered at 2.1 keV and 15.7 keV. Lead (Pb) was also registered twice. The first peak for Pb L_{α} was at 2.4 keV, and the second peak was at 10.6 keV. Nevertheless, the received values were still in the same range as for the PVB/PZT and PMMA/PZT samples. The map of the distribution and the relative proportion of the chemical elements over the scanned area is presented in Table 16 and Fig. 48.

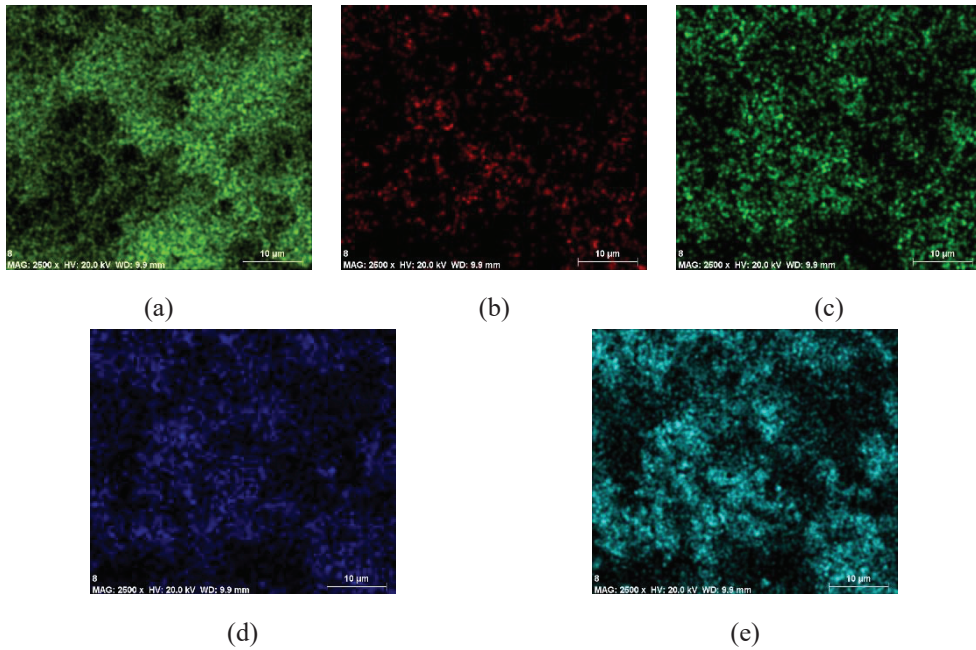


Fig. 48. Relative proportion (intensity) and distribution maps of PS/PZT sample

Table 16. Chemical characterization of PS/PZT sample

Element	C	O	Ti	Zr	Pb	Sum
Series	K	K	K	L	L	
Normalized Concentration (norm. wt.%)	69.40	10.65	2.65	6.21	11.08	100.00
Atomic Weight Percent (norm. at.%)	87.27	10.05	0.84	1.03	0.81	100.00
An Error in the Weight Percent Concentration (%)	8.91	19.44	0.12	0.31	0.46	-
Figure	Fig. 48a	Fig. 48b	Fig. 48c	Fig. 48d	Fig. 48e	-

The defined position of every element stated in the tables had its own characteristic peak in the sample corresponding to the transition in its electron shell. Five main elements were registered in each sample: Carbon (C), Oxygen (O), Titanium (Ti), Zirconium (Zr), and Lead (Pb). The registered intensity value was highly dependent on the excited X-Ray intensity, as well as on the X-Ray detector efficiency on the energy spectrum and on the geometry of the investigated sample itself.

FTIR analysis on all three samples was completed. The results are shown in Figs. 48–50. The absorbance spectrum of FTIR analysis was selected as 4000–500 cm^{-1} as it is the typical spectrum for this kind of analysis.

Strong and wide absorption peaks were registered in the PVB/PZT sample across the whole FTIR spectrum (Fig. 48). Peaks at 3502 cm^{-1} , 2971 cm^{-1} ,

1726 cm^{-1} , 1436 cm^{-1} , 1382 cm^{-1} , 1154 cm^{-1} , and 1006 cm^{-1} were registered for the O-H stretch, C-H stretch, C=O stretch, CH_3 bend, CH_2 bend, C-O-C stretch, and C-O stretch, respectively. The entire range of these results corresponded to the FTIR absorbance spectra of PVB, which is the bonding material in this sample [200].

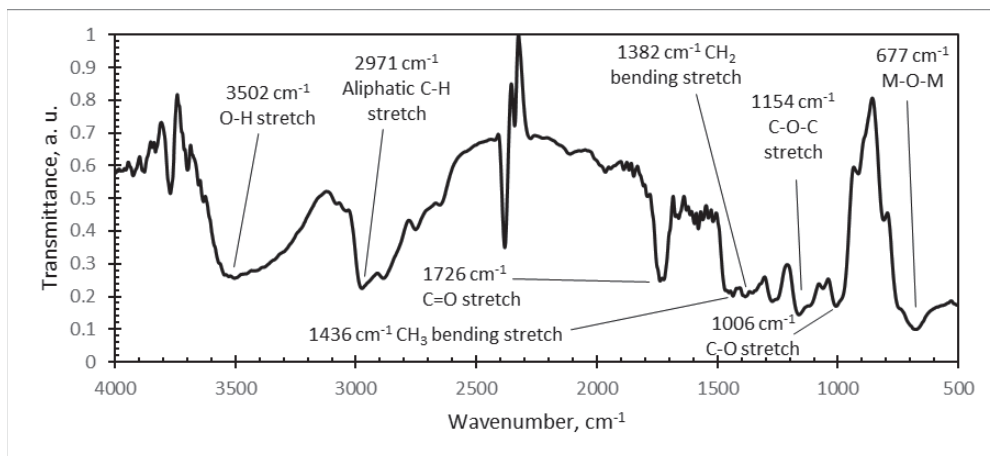


Fig. 48. FTIR spectra of PVB/PZT sample with 80 wt.% PZT

Strong and wide absorption peaks were registered in the PMMA/PZT sample across the whole FTIR spectrum (Fig. 49). Peaks at 3451 cm^{-1} , 3009 cm^{-1} , 1752 cm^{-1} , 1652 cm^{-1} , and 1209 cm^{-1} were registered for the -OH stretch, C-H stretch, C-H bend, -OH bend, and C-O-C stretch respectively. The entire range of these results corresponded to the FTIR absorbance spectra of polymethyl methacrylate (PMMA), which is the bonding material in this sample [201].

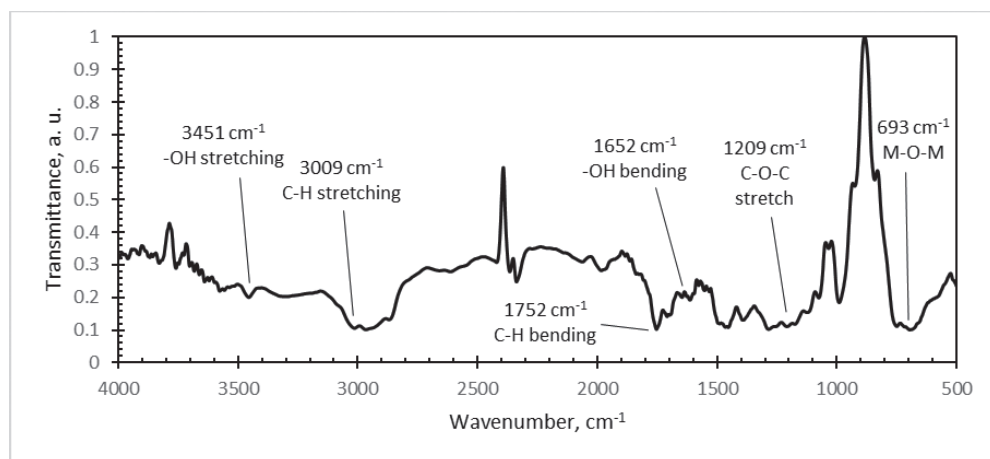


Fig. 49. Fourier Transform Infrared Spectroscopy spectra of PMMA/PZT sample with 80 wt.% PZT

Strong and wide absorption peaks were registered in the PS/PZT sample across the whole FTIR spectrum (Fig. 50). Peaks at 2941 cm^{-1} , 1732 cm^{-1} , 1601 cm^{-1} ,

1271 cm^{-1} , and 764 cm^{-1} were registered for C-H stretch, C=C bend, C=C stretch, -CH₂ stretch, and C-H stretch, respectively. The entire range of these results corresponded to the FTIR absorbance spectrum of polystyrene (PS) which is the bonding material in this sample [202].

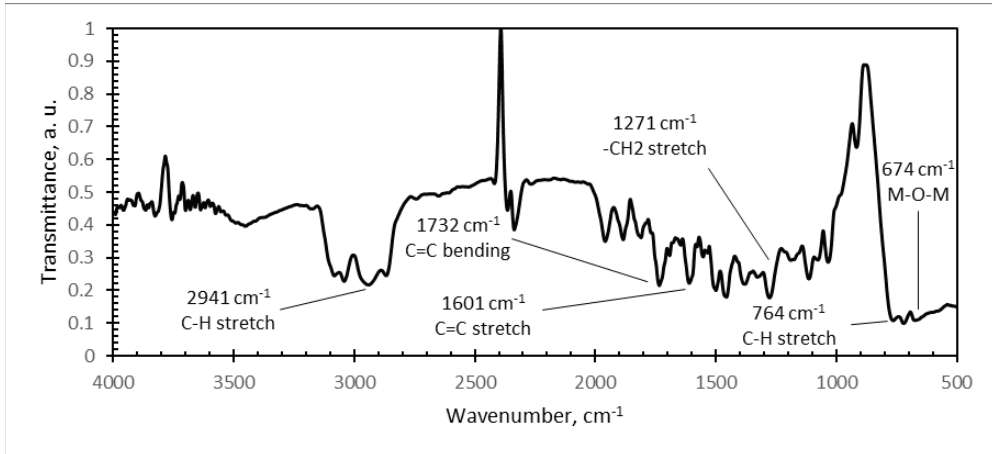


Fig. 50. Fourier Transform Infrared Spectroscopy spectra of PS/PZT sample with 80 wt.% PZT

The presence of polymers was defined by the infrared spectra of all the three samples in the interval of 4000–1000 cm^{-1} . A strong impact on the absorbance of the spectra was registered at about 700 cm^{-1} due to the presence of PZT. This also identifies the difficulty of results registering at the 511 cm^{-1} band for the composites with 20 wt.% and higher content of ceramics. The range of 800–550 cm^{-1} shows wide and very strong peaks which correspond to M-O-M bonds (where M is a metal) of PZT (e.g., Ti-O, Ti-O-Ti, Zr-O, and Zr-O-Zr) [203]. A conclusion can be suggested here that the increased PZT part of the composite makes the binders' material absorbance peaks weak because of PZT dominance. Weak absorbance peaks show that there are more M-O-M bonds in the concentration than there are organic compounds.

2.5. Piezoresistive characteristics of piezoelectric composite

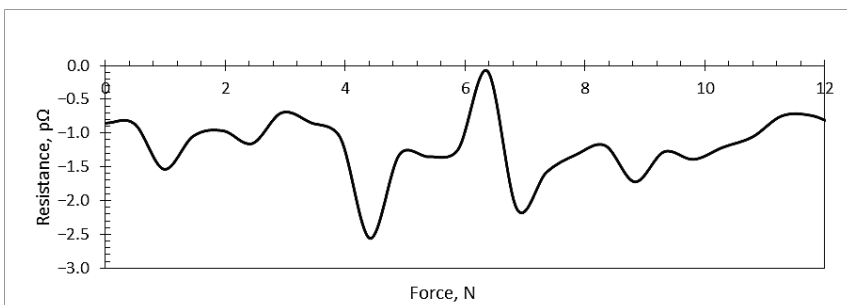
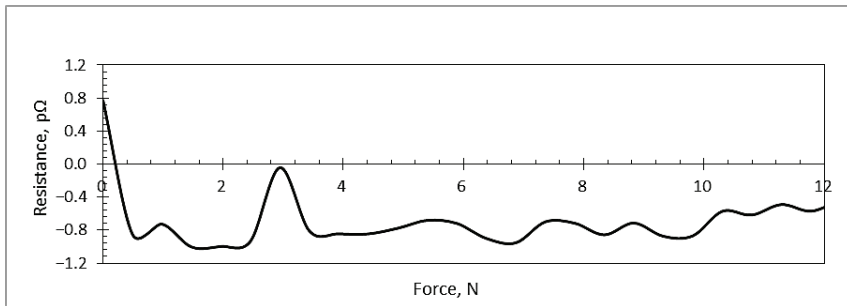
A *Keithley* meter scanner was used to analyze the piezoresistive characteristics of the sample with all the three different binder materials. In terms of the schematic view of the sample given in Fig. 31, all the samples were made with the width and height of 24 and 0.5 mm, respectively. The acting force points were separated by 42 and 24 mm, and they were designated as L and l. The obtained experimental data is presented in Table 17.

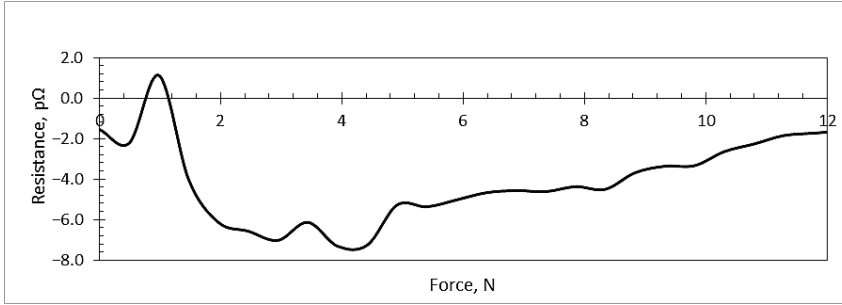
Table 17. Gauge factor (GF)

Value	PVB/PZT Coating	PMMA/PZT Coating	PS/PZT Coating
GF	-139.5	1151.0	-3458.8

A negative gauge factor value which was registered in the PVB/PZT and PS/PZT samples indicates that resistance decreases when the applied strain is increased. The PVB/PZT sample gauge factor was the lowest, specifically, -139.5, while for the PMMA/PZT sample the gauge factor was 1151. The sample with PS binder registered a gauge factor of -3458.8, which is almost 27 times higher than the gauge factor of the PVB/PZT sample.

The dependency between resistance and force was linear in all the three samples. Nevertheless, the relationship curve started to ascend only from a specific point (Fig. 51). This point for PVB/PZT coating was 3 N. After the increase in force resulted in an increase of resistance, only very minor changes were observed (Fig. 51 (a)). During the analysis of the PMMA/PZT sample, the resistance value decreased significantly when the force reached ~ 4.2 N. From this point, the resistance started to increase again, but with high fluctuations of values (Fig. 51 (b)). The highest turning point was registered for the sample with PS binder. Here, a significant change was registered at ~ 7 N of force. Same as before, after this point, the resistance level began to climb up once again (Fig. 51 (c)). The results showed that these samples, piezoelectric films, have a clear start threshold where force is needed to drop the resistance at a certain point to 7 p Ω and then to ascend linearly. Also, it is clearly seen that the threshold is highly dependent on the material of the binder. This analysis was performed 15 times for each case in order to ensure high repeatability and objective results. Only the average values are given in the figures below.





(c)

Fig. 51. The resistance-force relationship: (a) PVB/PZT sample, (b) PMMA/PZT sample, and (c) PS/PZT sample

The value of capacitance, which is an important aspect of any piezoelectric material, was also analyzed with the samples given in Fig. 52.

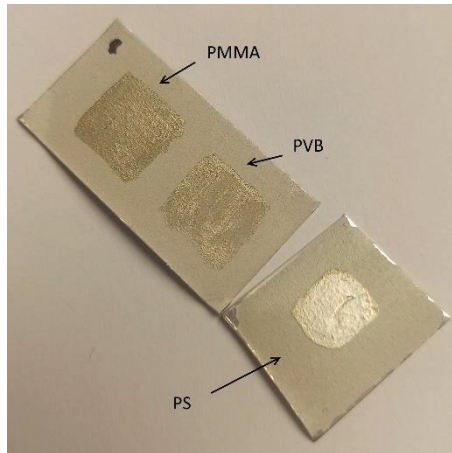


Fig. 52. Prepared samples for analysis of capacitance

The piezoelectric material does work as a capacitor when it operates well below its resonant frequency. In order to calculate the capacitance of a piezoelectric layer, Equation (2.5.1) was used [204]. The value of capacitance is directly dependent on the surface area and on the thickness of the piezoelectric coating and its material properties

$$C \approx n \cdot \epsilon_{33} \cdot \frac{A}{d_s}, \quad (2.5.1)$$

where C is the capacitance, n is the number of coating layers, ϵ_{33} is the dielectric constant, A is the electrode surface area of a layer, and d_s is the layer thickness. The calculated values of the capacitance of each sample are given in the table below (Table 18).

Table 18. Capacitance of each sample

Coating	Capacitance C, pF
PVB/PZT	0.13
PMMA/PZT	0.20
PS/PZT	0.10

From the obtained results, it can be stated that the capacitance value of every piezoelectric coating which was 70 μm thick was virtually the same, and only small changes were registered. Nevertheless, the highest capacitance of 0.20 pF was calculated from the sample with PMMA binder.

The current–voltage curve was obtained by using the same *Keithley* meter scanner as in the previous analysis. By sourcing the voltage in the 0–200 V interval by a 2 V step, each piezoelectric nanocomposite coating could be evaluated (Fig. 53).

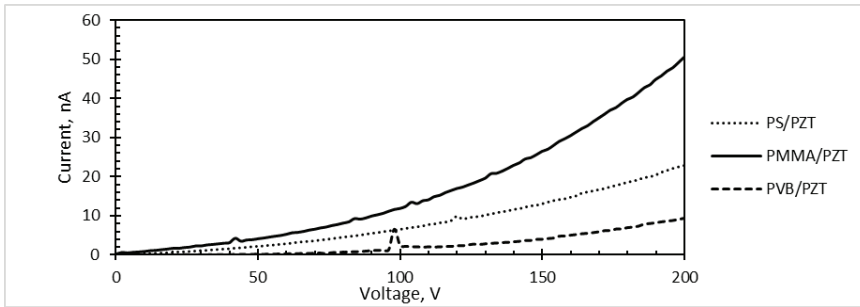
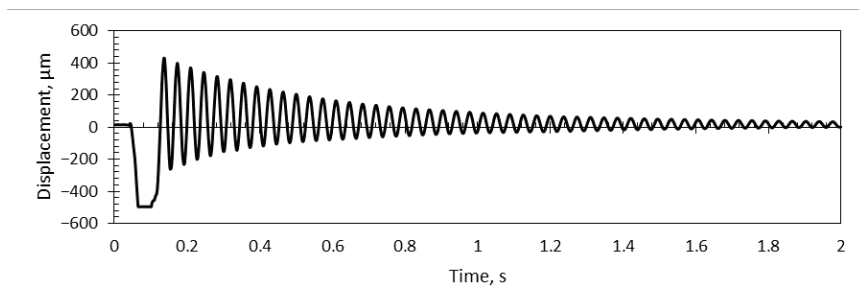


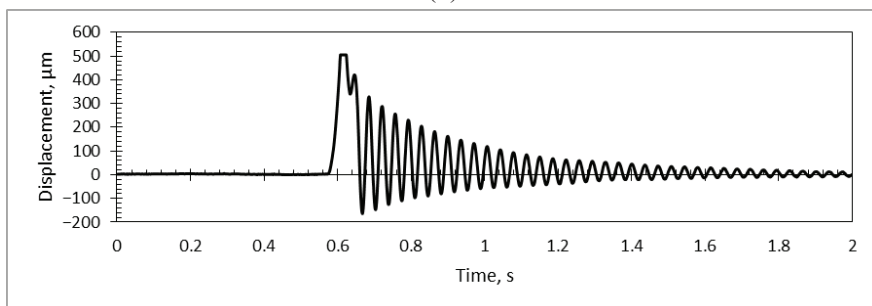
Fig. 53. Current–voltage characteristics of each piezoelectric coating

The curves in Fig. 53 are defined as current I which goes through the device relationship to voltage V across the terminals of devices. Each of the evaluations was completed 10 times, i.e., 5 times for each terminal. To calculate the results, the voltage had to be increased in steps across the device from one level to another, and then we had to measure the currents in this process (a sweep). Therefore, the sweep of the voltage in the interval of 0–200 V resulted in the following values: the current of PS/PZT increased linearly up to ~ 23 nA; the PMMA/PZT current also increased linearly till ~ 51 nA. On the other hand, the PVB/PZT linearity extended only to 0.94 nA, which is 24 and 54 times less than the other samples, respectively. The obtained values are similar to those found in literature [205, 206]. Due to the significant increase in the current in PMMA/PZT binder, a suggestion to make an active element for a pressure sensor based on piezoelectric nanocomposite from PMMA/PZT material arose as it could increase the sensing performance of the created device.

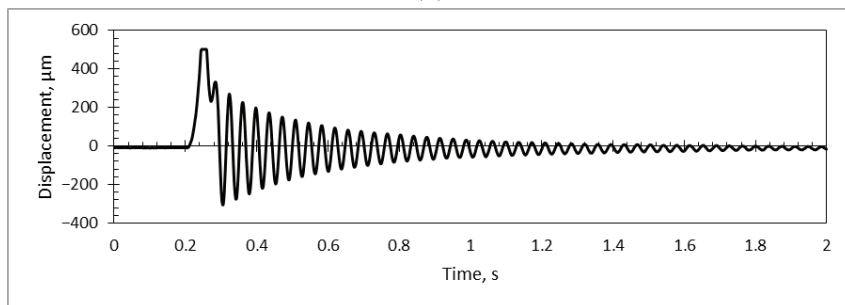
The dynamical analysis of each sample was performed with the stand presented in Paragraph 2.2.6. A pendulum with a suspended mass was released and had to hit the sample. The pendulum was stopped after the contact. The impulse excitation to the sample created a free vibration response which was registered by the PicoScope system. Fig. 54 (a), 54 (b), and 54 (c) represents the mechanical response of the sample.



(a)



(b)



(c)

Fig. 54. Vibrational response of the (a) PVB/PZT, (b) PMMA/PZT, and (c) PS/PZT coating to a mechanical impulse

The main factors of the quality of a microresonator could be evaluated by defining the damping ratios and Young's modulus of each sample (Table 19). Constructional or environmental damping imposes the top limit on the quality [207]. It means that the quality is ameliorated if the negative damping feedback is increased. Young's modulus impacts the stiffness of the created coating. By using the values received from experiment analysis, the values of the damping coefficient and Young's modulus, as outlined above, are calculated (Table 19).

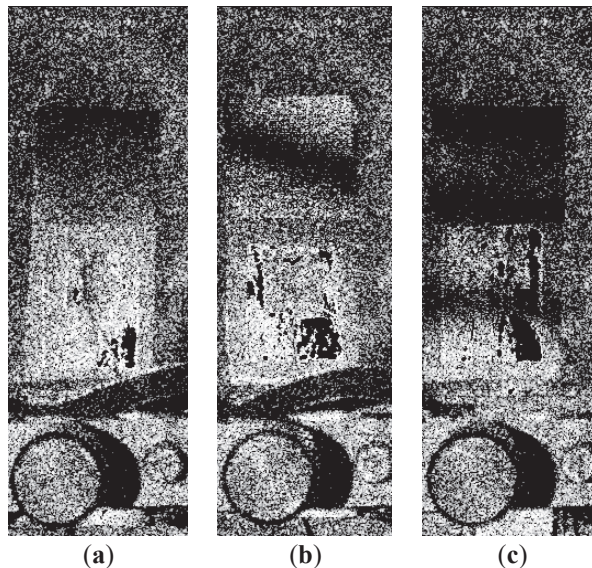
Table 19. Main factors of created coatings

Coating	Binding Material	Density, ρ , kg/m ³	Damping Ratio, ζ	Resonant Frequency, f , Hz	Young's Modulus, E , GPa
PVB/PZT	PVB	6298	0.0052 ± 0.0003	26.5 ± 0.4	3.9 ± 0.3
PMMA/PZT	PMMA	6316	0.0077 ± 0.0006	29.4 ± 0.9	6.3 ± 0.8
PS/PZT	PS	6288	0.0080 ± 0.0004	28.3 ± 0.6	5.3 ± 0.4

6.3 GPa, the highest value of Young's modulus, was calculated for the PMMA/PZT coating. Although polystyrene coating (PS/PZT) showed similar results (5.3 GPa), the value for PVB/PZT coating was 1.6 times lower than for PMMA/PZT sample, i.e., it was only 3.9 GPa. The results calculated in this analysis do correspond to the tendency observed in literature: the PMMA binder material with the highest Young's modulus [208], the PS binder with a lower one [209], and PVB with the lowest of the three [210]. The correlation of the obtained analytical and theoretical results shows the veracity of the performed calculations.

Holographic interferograms (shown in Fig. 55 (a), 55 (b), and 55 (c)) were obtained with the help of the PRISM system described in Paragraph 2.2.7. From the registered interferograms, the resonant frequencies of all the samples could also be acquired.

The amplitude of vibrations for the PVB/PZT coating sample reached 100 nm at 114 Hz resonant frequency. This was registered at 100 V of voltage. By using the same conditions for the two other coatings (PMMA/PZT and PS/PZT), the obtained results were 164 nm at 114 Hz of the resonant frequency and 366 nm at 114 Hz of the resonant frequency, respectively.

**Fig. 55.** Holographic interferograms of the (a) PVB/PZT, (b) PMMA/PZT, and (c) PS/PZT coating samples

The direct piezoelectric effect was applied for further investigations of the created piezoelectric nanocomposites. The obtained results showed that the samples are able to generate electrical voltage when they are mechanically excited. This is achieved due to the piezoelectric effect which comes from the 80% PZT part of the coating (Fig. 56). The generated electrical energy from each sample was 3 mV, 2.1 mV, and 2.5 mV for PS/PZT, PVB/PZT, and PMMA/PZT coatings, respectively. All of the coatings showed similar results, although the highest value was obtained for the polystyrene sample, and the lowest value was received for the PVB/PZT sample.

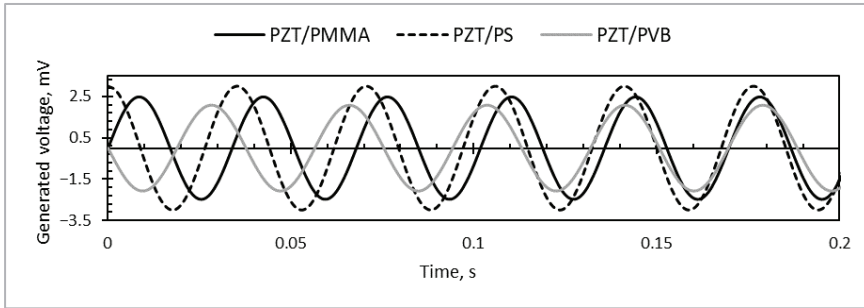


Fig. 56. Generated electrical energy from each of the samples by periodical excitation

VSWR meter *P2-67* was used to measure the sheet resistivity of each coating. The analysis was done for each sample by placing it between a $\lambda/4$ jumper and the open end of a waveguide with a $16 \times 8 \text{ mm}^2$ inner cross-section. The results showed that the sheet resistance for each sample exceeded $20,000 \text{ k}\Omega/\text{sq}$ (Table 20). The uniformity of the conductive coating for quality assurance is defined by these results.

Table 20. Sheet resistivity values of each coating sample

Coating	Sheet Resistivity, (Ω/sq)
PVB/PZT	$>20,000$
PMMA/PZT	$>20,000$
PS/PZT	$>20,000$

2.6. Microhardness of Coatings

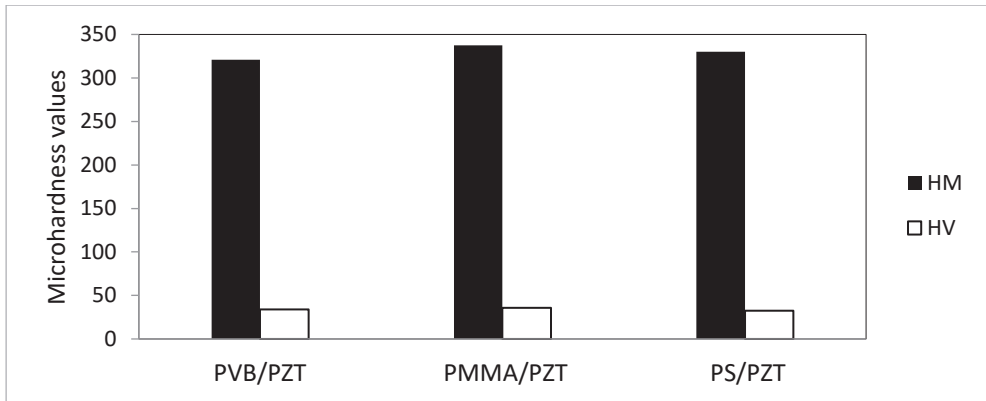
A dynamic microhardness meter with its base *HM 2000S* was used to perform the microhardness analysis of each coating sample. The measurements took place 10 times each with a maximum indentation depth of $4 \text{ }\mu\text{m}$. The analysis was performed under a maximum load of 200 g increased gradually. Two types of microhardness were measured: Martins microhardness (HM), and Vickers microhardness (HV) (Table 21).

Table 21. Martins and Vickers microhardness measurement results

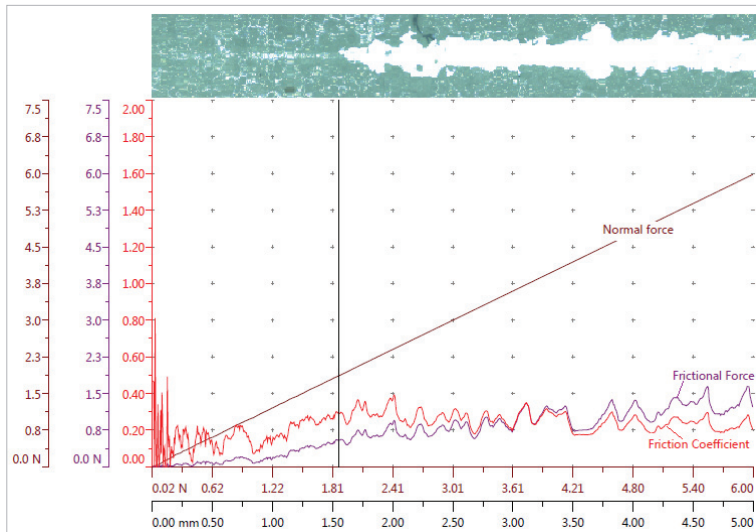
	PVB/PZT			PMMA/PZT			PS/PZT		
	HM	HV	h_{max}	HM	HV	h_{max}	HM	HV	h_{max}
$n = 10$	N/mm ²		μm	N/mm ²		μm	N/mm ²		μm
X.	320.81	33.87	4.32	337.40	35.77	4.34	330.22	32.54	4.43
q	108.81	12.11	0.18	84.87	9.58	0.13	81.26	7.81	0.10
s	152.07	16.93	0.25	118.61	13.40	0.18	113.56	10.91	0.14
V/%	47.40	49.98	5.76	35.15	37.45	4.16	34.39	33.54	3.20
Min.	108.60	11.90	4.10	133.80	14.90	4.00	132.50	12.00	4.27
Max.	515.00	55.30	4.95	567.40	61.30	4.61	514.30	47.90	4.67
R	406.38	43.90	0.85	433.59	46.33	0.61	381.74	35.87	0.40
R/%	126.67	128.12	19.73	128.51	129.51	14.04	115.60	110.24	9.08

Here, HM is microhardness in the Martins scale; HV is microhardness in the Vickers scale; n is the number of single readings per block; X. means the value of the individual mean values, i.e., the so-called arithmetic mean value; q is a random measurement error (within a certain probability (confidence level), the likely ‘true’ value m of the measured quantity is in an interval (a two-sided confidence interval) around the measured mean value X of a measurement series, and the borders of this interval have distance q from the ‘true’ value); s is the standard deviation, a measure for the deviation of the spread of the single readings of a measurement series around their common mean value X; V/% is the coefficient of variation describing the spread of a measurement series in percentage; Min. is the lowest reading of the block; Max. is the highest reading of the block; R is the range, the difference between the highest and the lowest reading of the block; R/% is the range in percentage.

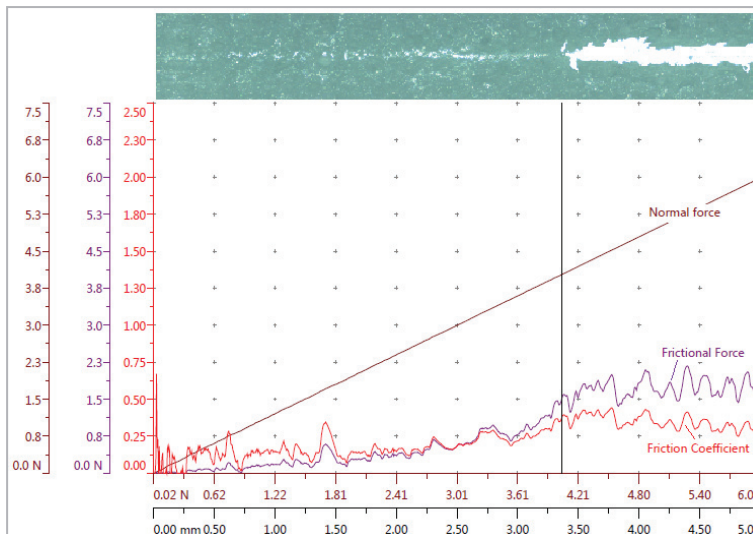
From the obtained results, it is clear that there is only an insignificant difference of Martins and Vickers microhardness values between the different coatings. Martins microhardness differs only by about 17 N/mm², and Vickers microhardness difference was even lower – only about 3 N/mm² (Fig. 57). On the other hand, the PMMA/PZT coating showed stronger elastic deformation than other binding materials.

**Fig. 57.** Martins and Vickers microhardness of each coating

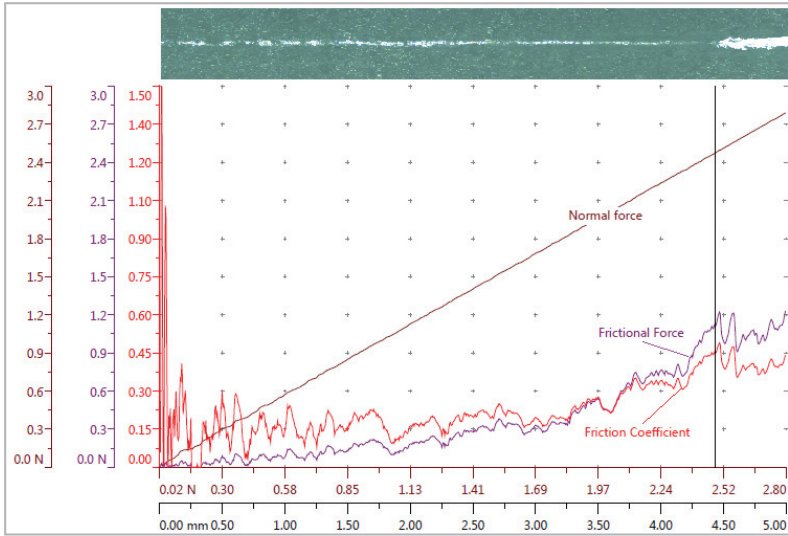
The critical load with the coefficient of friction, as well as the frictional and normal forces on the created coating samples could be identified during the scratch test. In order to determine whether the coating failed several types of analysis were performed, optical microscopy, acoustic emission, and analysis on the penetration depth variation were conducted. A scratch test was performed on a sample with 2 μm coating thickness with all the three materials (PVB, PMMA, and PS). A 0.2 mm radius diamond was used for a 5 mm scratch length. The scratch test took 30 s, and, in that time, the normal load was increased from 0 to 6 N. Each sample was analyzed 4 times, and the mean data for the scratch tests of each sample is presented in Fig. 58.



(a)



(b)



(c)

Fig. 58. Frictional force, normal force, friction coefficient, and the corresponding panorama image of (a) PVB/PZT, (b) PMMA/PZT, and (c) PS/PZT coatings recorded during the scratch test of each sample

The highest resistance to scratching was recorded in the sample with the PMMA binder material. Here, the average critical load reached 3.988 N. That is 36% more than the second highest result and almost twice as high as the sample with the lowest critical load. The PS/PZT sample withstood a 2.556 N force and PVB/PZT of only 1.865 N. These results suggest that, from the three samples, the PMMA/PZT sample is the hardest and most resistant to scratching. The panorama pictures given in Fig. 58 clearly show these results. Here, the scratch track can be seen where the brighter area (the scratched material) corresponds to the vertical line of the critical load. The point where the scratch becomes wide is the critical failure, and it is there that the critical load reached its maximum value. To achieve qualitative results, several tests were completed. The values showed excellent repeatability. All the values and registered results are presented in Table 22.

Table 22. Critical load values of PVB/PZT, PMMA/PZT, and PS/PZT samples

Coating	Critical Load 1, N	Critical Load 2, N	Critical Load 3, N	Critical Load 4, N	Average Critical load, N
PVB/PZT	1.88	1.89	1.76	1.93	1.87
PMMA/PZT	4.04	3.91	3.97	4.03	3.99
PS/PZT	2.48	2.67	2.55	2.53	2.56

2.7. Section conclusions

The following conclusions were drawn from the completed analysis:

- Effective and relevant scientific equipment and methodology were selected and incorporated for the fabrication and analysis of the novel piezoelectric

composite. Composite material fabrication, thin layer formation and analytical equipment for material properties evaluation were chosen.

- The main factors for choosing the materials are functional properties and costs. Three different piezoelectric composite materials were fabricated: PVB/PZT, PMMA/PZT, and PS/PZT. A rather simple screen-printing technique, which is also low cost and effective, was chosen.
- For the analysis of the fabricated samples various types of methodology and tools were selected: SEM with *Quanta 200 FEG, Bruker Corporation*, AFM with *JPK NanoWizard 3, Bruker Corporation*, EDS with *X-Flash 4030, Bruker Corporation*, FTIR with *Vertex 70, Bruker Corporation*, Keithley meter scanner 2002 series, *Tektronix*, laser triangular displacement sensor *LK-G3000, Keyence*, with a *PicoScope 3424* oscilloscope, *Picotech*, electronic speckle pattern interferometry system *PRISM, Hytec*, voltage standing wave ratio methodology with a *P2-67* meter, *RF and CIS*, Vickers and Martins microhardness analysis with a *Fischerscope HM 2000S* microhardness meter, and micro-scratch tester *MST³, Fischer Technology*.
- The structural composition, chemical composition, piezoresistive characteristics, capacitance, current–voltage characteristics, mechanical response, mechanical properties, piezoelectric response, sheet resistivity, and microhardness were analyzed for each novel piezoelectric composite.
- The analysis results determined a superior sample of all the three options – the PMMA/PZT piezoelectric composite which showed the highest operation characteristics in almost all of the performed analyses. For further analysis and research, the PMMA/PZT piezoelectric nanocomposite was selected for the fabrication of the active membrane for a pressure sensor.

3. MODELING AND ANALYSIS OF OSCILLATING MEMBRANE FOR PRESSURE SENSOR

3.1. Methodology and tools

3.1.1. Mindlin-Reissner theory for thick plates

In the theory of thick plates, a.k.a. the theory of Raymond Mindlin and Eric Reissner, the normal to the mid-surface remains straight but not necessarily perpendicular to the mid-surface. Mindlin-Reissner theory was selected as it is stated as a more accurate, particularly for moderately thick plates [211].

For uniformly thick, homogenous, and isotropic plates, the stress-strain relations in the plane of the plate are calculated by Equation (3.1.1.1)

$$\begin{bmatrix} \sigma_{11} \\ \sigma_{22} \\ \sigma_{33} \end{bmatrix} = \frac{E}{1-\nu^2} \begin{bmatrix} 1 & \nu & 0 \\ \nu & 1 & 0 \\ 0 & 0 & 1-\nu \end{bmatrix} \begin{bmatrix} \varepsilon_{11} \\ \varepsilon_{22} \\ \varepsilon_{33} \end{bmatrix}, \quad (3.1.1.1)$$

where E is Young's modulus, ν is Poisson's ratio, and $\varepsilon_{\alpha\beta}$ are the in-plane strains. The through-the-thickness shear stresses and strains are related by Equation (3.1.1.2) and Equation (3.1.1.3)

$$\sigma_{31} = 2G\varepsilon_{31}, \quad (3.1.1.2)$$

$$\sigma_{32} = 2G\varepsilon_{32}; \quad (3.1.1.3)$$

where the shear modulus G can be replaced as Equation (3.1.1.4).

$$G = \frac{E}{2(1+\nu)} \quad (3.1.1.4)$$

The relations between the stress resultants and the generalized displacements for an isotropic Mindlin-Reissner plate are represented by Equation (3.1.1.5) and Equation (3.1.1.6)

$$\begin{bmatrix} N_{11} \\ N_{22} \\ N_{12} \end{bmatrix} = \frac{2Eh}{1-\nu^2} \begin{bmatrix} 1 & \nu & 0 \\ \nu & 1 & 0 \\ 0 & 0 & 1-\nu \end{bmatrix} \begin{bmatrix} u_{1,1}^0 \\ u_{2,2}^0 \\ \frac{1}{2}(u_{1,2}^0 + u_{2,1}^0) \end{bmatrix}, \quad (3.1.1.5)$$

$$\begin{bmatrix} M_{11} \\ M_{22} \\ M_{12} \end{bmatrix} = -\frac{2Eh^3}{3(1-\nu^2)} \begin{bmatrix} 1 & \nu & 0 \\ \nu & 1 & 0 \\ 0 & 0 & 1-\nu \end{bmatrix} \begin{bmatrix} \varphi_{1,1} \\ \varphi_{2,2} \\ \frac{1}{2}(\varphi_{1,2} + \varphi_{2,1}) \end{bmatrix}; \quad (3.1.1.6)$$

where E is Young's modulus, ν is Poisson's ratio, and h is the thickness of the plate. Additionally, we employ Equation (3.1.1.7)

$$\begin{bmatrix} Q_1 \\ Q_2 \end{bmatrix} = \kappa Gh \begin{bmatrix} \omega_{,1}^0 - \varphi_1 \\ \omega_{,2}^0 - \varphi_2 \end{bmatrix}, \quad (3.1.1.7)$$

where κ is the shear correction factor, G is the shear modulus, and h is the thickness of the plate. The simplification of Equations (3.1.1.5), (3.1.1.6), and (3.1.1.7) yields the result of Equation (3.1.1.8). Here, the bending rigidity is defined as quantity D .

$$D = \frac{2Eh^3}{3(1 - \nu^2)} \quad (3.1.1.8)$$

If h in Equation (3.1.1.9) is considered as half of thickness H , then the bending rigidity becomes as in Equation (3.1.1.10)

$$h = \frac{H}{2} \quad (3.1.1.9)$$

$$D = \frac{EH^3}{12(1 - \nu^2)} \quad (3.1.1.10)$$

3.1.2. Membrane formation

Silicon dioxide is one of the most common structural or sacrificial layers in thin film fabrication [212]. Mainly, it is used as a sacrificial layer in order to obtain aluminum membranes.

Before the deposition process taking place, samples have to be prepared by removing any contamination. All the samples are cleaned by using plasma cleaning techniques. They incorporate energetic plasma which removes impurities and contaminants from surfaces. Such gases as argon or oxygen are used as well as their mixtures. Plasma is then created by using electric fields of the GHz level to ionize low pressure gas. The energized ions react with the material on surfaces by evaporating them and thus creating gaseous products which are removed by vacuum. The process requires extremely high temperatures.

Even though the samples have been prepared, the issue of the thickness ratio of the membrane is still present. This could lead to fragile and unstable structures. Thus, photolithography, photoresist application and etching processes were used for the formation of a membrane.

Photolithography is a process to remove parts of a thin film selectively. Light is used to transfer the required geometric pattern from a photo mask to a light-sensitive chemical on the substrate. Then, the geometric pattern is engraved in the material. Photolithography is well known for its control ability of the geometrical parameters of the final product and also for its ability of pattern creation on the entire surface although a flat substrate is needed for that. Additionally, sterile operating conditions are required. Cleanliness is ensured by plasma cleaning techniques.

Photolithography is based on the processes of photoresist application, exposure and developing, etching, and photoresist removal. First of all, the substrate is covered with a photoresist. The sample is immersed into a liquid solution of the photoresist and then spun rapidly. This makes the photoresist layer uniform. Furthermore, the substrate is soft-baked so that to remove the excess solvent. It was completed in an IR drying/heating oven *LADA*. This process was performed two times under the same conditions in order to deposit the photoresist on both sides of the substrate. The subsequent process was superpositioning and exposure. The

removal of the photoresist was completed by using a mask alignment and exposure system *JUB 76G*. Due to chemical reactions, it becomes possible to remove some parts of it. The removal is completed by a solution of clean deionized water and 0.8% of sodium hydroxide (NaOH). Finally, etching of the silicon layer was performed. First of all, the silicon layer was removed with tetramethylammonium hydroxide (TMAH). It left the SiO_2 layer untouched. By using the reactive ion etching (RIE) technology, the silicon dioxide layer was removed. Strong radio frequency (RF) radiation was applied to the substrate, which caused the formation of plasma.

Thin film deposition is commonly performed by using the vacuum evaporation method. The evaporated metal particles with the help of vacuum travel directly to the substrate where they condensate back to a solid. Evaporation is used in microfabrication and to make macro-scale products, such as metallized plastic films.

Two main processes are involved in vacuum evaporation: firstly, it is the evaporation of the source material by using high temperatures, and, secondly, it condenses back to the solid on the substrate. This resembles the process of liquid water appearance on the lid of a boiling pot. Although the tools and environment are different, both processes are denoted by very similar approaches. A schematic view of the vacuum evaporation process is given in Fig. 59.

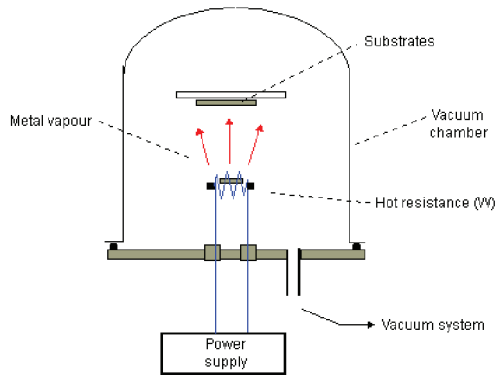


Fig. 59. Schematic view of vacuum evaporation process [213]

As the name states, the evaporation process takes place in vacuum. It means that almost all other vapors are removed before the process begins. This helps the material's particles travel directly to the deposition substrate without being involved in any additional processes. In the case of low vacuum, the evaporated atoms are in danger of colliding with any unwanted particles, which can cause a reaction. A simple example is aluminum evaporation when the atoms of aluminum collide with oxygen, which causes aluminum oxide to form. Additionally, unwanted reactions interfere with the process stability. In low vacuum, or in an unstable system, the thickness of the final product is impossible to control. On the other hand, if the process is stable and proceeds as intended, it is easy to control and calculate the final thickness of the metal film. Another drawback of the process caused by the rough

surface of a substrate is the non-uniformly deposited material. This is again caused by a low level of the preparation and quality of the process.

Vacuum evaporation of the membrane was performed by using vacuum evaporation equipment *YBH-71D3* (Fig. 60).



Fig. 60. Vacuum evaporation equipment *YBH-71D3*

Vacuum evaporation is incorporated in various fields of industry. It is mainly used for material creation and fabrication [214]. Also, food industry is benefiting from vacuum evaporation, i.e., it is used for production of cherry juice [215]. Electronics [216] and environmental problems can also be solved by this method [217].

3.1.3. Thermal embossing for microstructure imprinting

Thermal embossing is a process for periodical microstructure formation on the surface of a sample. Heating up a sample causes the polymer to reach its melting temperature. The heated mold is pressed onto the surface at the melting temperature point. The time interval for pressing can be different depending on the process regime. Afterwards, the mold is removed, and the sample is left with the imprint of the periodical microstructure which resembles the original geometry. The process of thermal embossing is shown in Fig. 61.

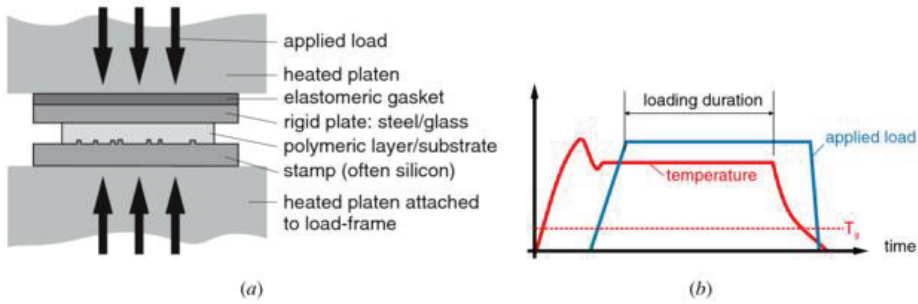


Fig. 61. Schematic view (a) and process graph (b) of thermal embossing technique [218]

Thermal embossing is widely used due to its simple set-up and short implementation time [219]. It is also able to replicate various materials in the ranges from several nanometers to hundreds of micrometers. Unfortunately, in some cases, this method takes too long, which is a drawback for the stamping industry [220].

For the thermal imprinting of periodical microstructure into a multilayered membrane, the technology used by Sodah was employed [221]. Three main steps are taken into account: heating, imprinting, and demolding:

1. Heating starts at ambient temperature. At the time the stamp reaches the membrane surface, it starts to heat up. During this process, the heat transfers to the multilayered membrane, where the imprint of the stamp begins to form.
2. During the imprinting process, the force acting between both samples (the stamp and the multilayered membrane) is increased. Plastic deformations start to form in the multilayered membrane.
3. Demolding happens after the imprinting when the stamp is being removed. The multilayered membrane is left to cool down and is left with an imprint in the form of the periodical microstructure.

A schematic representation of the imprinting process is given in Fig. 62.

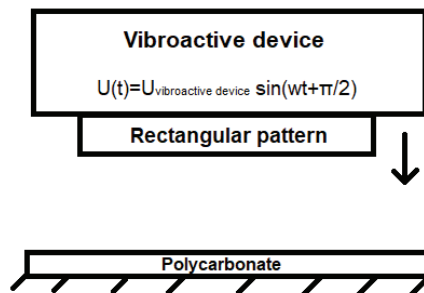


Fig. 62. Schematic diagram of thermal imprinting with high frequency vibration assistance [221]

The imprinting process (Fig. 63) can be used for a vast number of materials. This is an advantage of this technique because other replication technologies are incapable of such differentiation of materials.

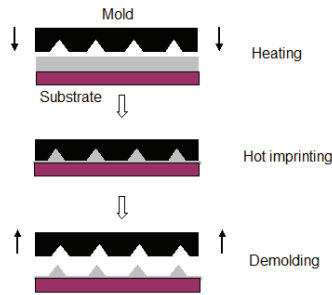


Fig. 63. Schematic view of imprinting process

3.1.4. Laser Doppler vibrometer

Frequency response analysis of the fabricated membranes was performed by using a *Polytec* scanning laser Doppler vibrometer (Fig. 64).



Fig. 64. Experimental setup of *Polytec* scanning laser Doppler vibrometer

The tested sample was fixed on the platform which was attached to a piezoelectric actuator *PSt 150/4/20VS9* (produced by *Piezomechanik GmbH*, Munich, Germany). It was excited by using a periodical signal which was generated by a function waveform generator *Agilent 33220A* and amplified by a linear amplifier *EPA-104* (made by *Piezo Systems Inc.*, Woburn, MA, USA). The interference optical laser signals generated and registered by a *Polytec OFV 512* fiber-optic interferometer were transformed into an electrical signal using a *Polytec OFV 5000* vibrometer controller via an *MSV-Z-40 Scanner* controller. Furthermore, it was transmitted to a *Polytec Vibrascan DAQ* PC for further analysis. For adjusting the laser beam and the sample, a *Nikon* microscope *Eclipse LV100* with a digital video camera *Pixelink PL-A662* was used. The center of the membrane was positioned for the concentrated laser beam. The electrical signal generated by the

piezoelectric layer of the energy harvester was collected by an oscilloscope *PicoScope 3424* (developed by *PicoTechnology Ltd.*, St Neots, UK).

3.2. Shape of the membrane

As stated in Paragraph 1.4, there are three different approaches towards the membrane. The geometry can be selected as a rectangle, a square, or a circle. The most common approach for pressure sensors is the square membrane. Square membranes are denoted by a superior sensitivity in comparison with the two other variants with the same thickness. Also, it is easier to fabricate a square or rectangle membrane than a circular one.

To fully compare all the three geometries of the membrane, their maximum stresses and maximum deflections can be calculated and compared. Maximum stresses and the maximum deflection of a circular membrane are calculated by using Equation (3.2.1) and Equation (3.2.2), respectively. Equation (3.2.3) and Equation (3.2.4) are for a rectangle membrane, whereas Equation (3.2.5) and Equation (3.2.6) are for a square membrane.

$$\sigma_{circular} = \frac{3W}{4\pi h^2}, \quad (3.2.1)$$

$$W_{circular} = -\frac{3W(m^2-1)a^2}{16\pi E m^2 h^3}, \quad (3.2.2)$$

$$\sigma_{rectangle} = \beta \frac{pb^2}{h^2}, \quad (3.2.3)$$

$$W_{rectangle} = \alpha \frac{pb^4}{Eh^3}, \quad (3.2.4)$$

$$\sigma_{square} = \frac{0.308pa^2}{h^2}, \quad (3.2.5)$$

$$W_{square} = -\frac{0.0138pa^4}{Eh^3}; \quad (3.2.6)$$

where W is the total force acting in a membrane, h is the thickness of the membrane, E is Young's modulus, α and β correspond to the ratio between the length and the width of the membrane, p is the acting pressure, a and b correspond to the dimensions of the membrane, and m is expression $\frac{1}{\nu}$, where ν is Poisson's ratio. The total force acting in a membrane can be expressed by Equation (3.2.7).

$$W = \pi a^2 p \quad (3.2.7)$$

The negative sign in Equation (3.2.2) and Equation (3.2.6) shows only the direction of the deflection. It can be neglected by taking the modulus of the final result. A comparison of all the three shapes of geometry is given in Table 23.

Table 23. Geometric effect on membrane stresses and deflection

Geometry	Dimensions	Surface area	Maximum stress (MPa)	Maximum deflection (μm)	Reference
Circular	$d = 600 \mu\text{m}$	$0.283 \mu\text{m}^2$	0.43	69	Fig. 65
Rectangle	$a = 752 \mu\text{m}$ $b = 376 \mu\text{m}$	$0.283 \mu\text{m}^2$	5.62	27	Fig. 66
Square	$a = 532 \mu\text{m}$	$0.283 \mu\text{m}^2$	6.96	54	Fig. 67

The calculations in Table 23 are based on the same $26 \mu\text{m}$ thickness of the membrane. The boundary conditions are the same for all the three samples and are taken only as arbitrary values used for a comparison of the geometry. All of these three shapes feature the same surface area. Piezoelectric composite is taken as the material of which the membrane is fabricated, and aluminum is neglected because of its low impact on the final values (aluminum constitutes only 4% of the material in the membrane). Young's modulus was calculated in Paragraph 2.5. The maximum pressure is taken as 54 kPa . All of the edges of the structure are fixed. Poisson's ratio is taken as 0.25.

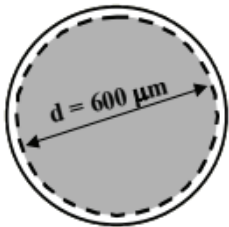


Fig. 65. Circular membrane for comparative analysis

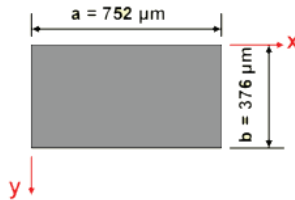


Fig. 66. Rectangle membrane for comparative analysis

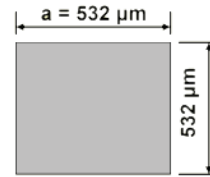


Fig. 67. Square membrane for comparative analysis

The square membrane has the highest induced stress of all the three cases. It is a favored geometry for pressure sensors because the high stresses generated by applied pressure loading result in high sensitivity. Even though the maximum deflection is not the highest for the square shape, it is still of a higher level in comparison with the other two geometry types (circular and rectangle). Combining both the maximum induced stress and the highest deflection ensures the highest electrical and optical sensitivity of the square-shaped membrane.

3.3. Finite element model of membrane

In order to analyze potential structure specifications of the membrane for a pressure sensor, *COMSOL Multiphysics* software was used to mimic the possible conditions of the working oscillating element. For that, a model of the membrane had to be created. A schematic view of the membrane is presented in Fig. 68.

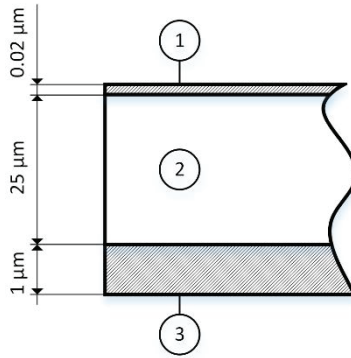


Fig. 68. Schematic drawing of multilayered vibrating membrane: 1 – aluminum layer, 2 – PZT nanocomposite layer, 3 – aluminum layer

The model is $250 \times 250 \mu\text{m}$ in length and width. The top layer of the membrane is an aluminum electrode, the middle is piezoelectric composite with the PMMA binding material, the bottom is an aluminum electrode. The thickness of the layers is $1 \mu\text{m}$ of aluminum and $25 \mu\text{m}$ of piezoelectric composite. Even though there is a second aluminum layer, it is neglected in the final model to save computational time and resources. Only a very insignificant part of the final material structure (0.0008%) makes up the second aluminum layer; that is why it can be neglected in the final computations.

A 3D view of the model in the *COMSOL Multiphysics* environment is shown in Fig. 69.

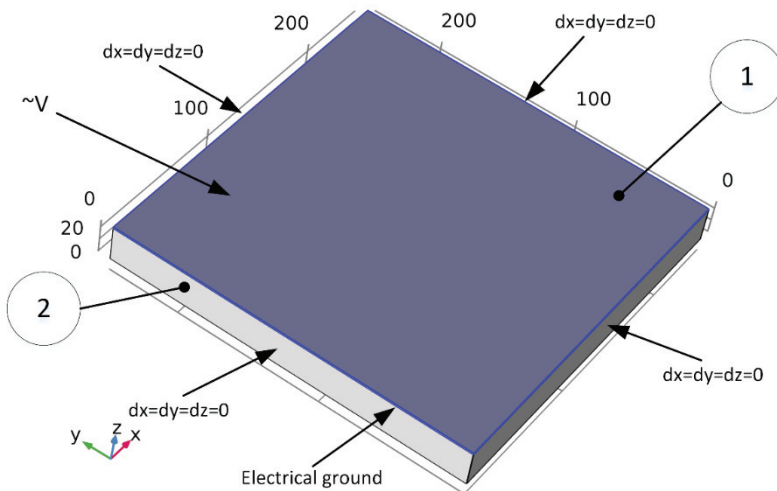


Fig. 69. 3D view of the model with the corresponding boundary conditions and structure: 1 – aluminum, 2 – PMMA/PZT

The used mesh for simulations was constructed from hexahedral (Fig. 70) and quadrilateral (Fig. 71) elements with an average element quality of 0.4882. The total statistics of the mesh is given in Table 24.

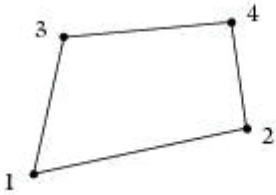


Fig. 70. Quadrilateral finite element schematic representation (numbers show the numbering of nodes)

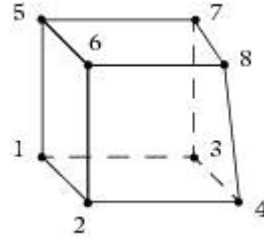


Fig. 71. Hexahedral finite element schematic representation (numbers show the numbering of nodes)

The mesh constructed for this model consisted of two parts. Section No. 1 was constructed of a fine mesh, section No. 2 was a coarse mesh (Fig. 72). This was done in order to obtain a more detailed image of the junction of two layers as well as the aluminum layer changes during the analysis. The total number of degrees of freedom (DOF) was 75684.

Table 23. Mesh statistics

Description	Value
Minimum element quality	0.1014
Average element quality	0.4882
Hexahedral	5400
Quadrilateral	3982
Edge element	434
Vertex element	12

In order to achieve the results, the Structural Mechanics model was chosen in *COMSOL Multiphysics* together with the Piezoceramics Devices model.

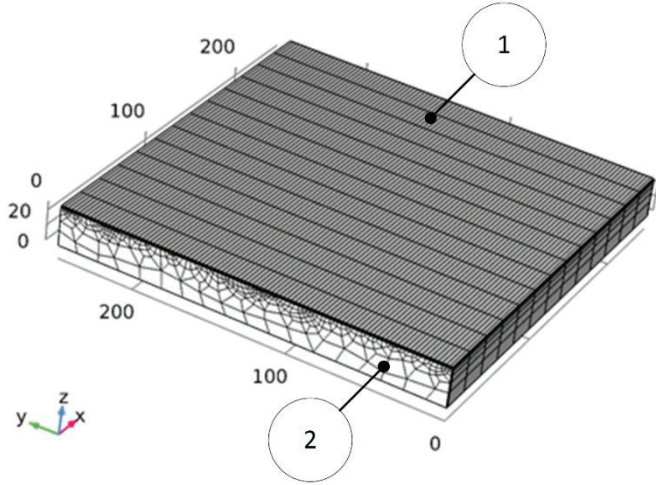


Fig. 72. Mesh of the structure used for finite element model

For both small and finite deformations, the total Lagrangian formulation is used. The computed stress and deformation state is then referred to the material configuration without taking its current position in space into account. The gradient of the displacement in 3D is always computed with respect to the material coordinates (Equation (3.3.1))

$$\nabla u = \begin{bmatrix} \frac{\partial u}{\partial X} & \frac{\partial u}{\partial Y} & \frac{\partial u}{\partial Z} \\ \frac{\partial v}{\partial X} & \frac{\partial v}{\partial Y} & \frac{\partial v}{\partial Z} \\ \frac{\partial \omega}{\partial X} & \frac{\partial \omega}{\partial Y} & \frac{\partial \omega}{\partial Z} \end{bmatrix}, \quad (3.3.1)$$

where u , v , and ω are the displacements in the corresponding X , Y , and Z axes.

3.4. Harmonic analysis of multilayered membrane

The resonant frequencies show the highest kinetic energy in the system. In order to fully represent the kinetic energy change during the oscillation, the shift between the modes Equation (3.4.1) and Equation (3.4.2) was used

$$dB = 10 \lg \left(\frac{E_{kinetic}}{E_{input}} \right)^2, \quad (3.4.1)$$

$$E_{input} = C_{PZT/PMMA} U_{input}^2; \quad (3.4.2)$$

where $E_{kinetic}$ is the resulting kinetic energy, E_{input} is the input kinetic energy, $C_{PZT/PMMA}$ is the capacitance of PMMA/PZT material, and U_{input} is the input voltage. Taking into account the previously calculated value of capacitance in Paragraph 2.5, the input energy was calculated to equal 80 pJ. The kinetic energy represented in decibels is given in Fig. 73.

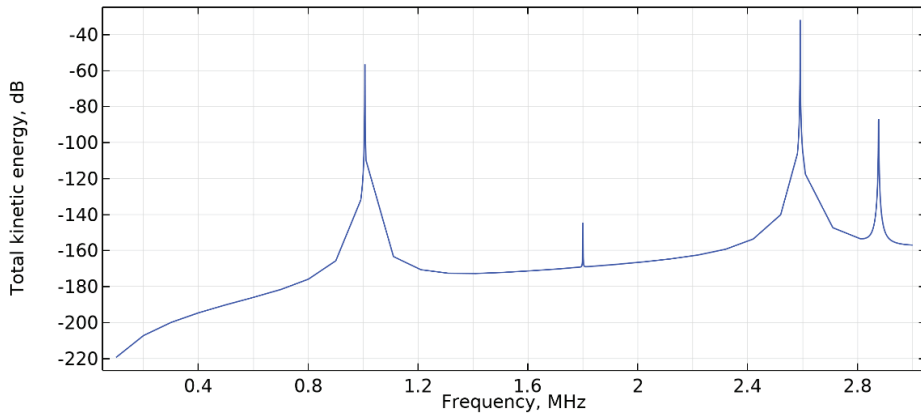


Fig. 73. Kinetic energy in resonant frequencies of multilayered membrane

The negative sign in the results shows that the input energy was higher than the one registered after the simulation. The kinetic energy registered in the 1st and 3rd vibration modes is similar as it reached approximately -58 to -35 dB. Other vibration modes are significantly lower.

The natural frequency modes of the multilayer membrane were calculated by using the kinetic energy peaks found in Fig. 73. The model was damped by using the conditions given in Paragraph 2.5 Piezoresistive characteristics of microresonators.

The membrane was given 20 V voltage harmonic excitation on its electrodes. Four vibration modes of the multilayer membrane were calculated. They are given in Figs. 74–75.

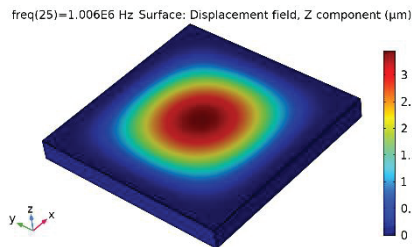


Fig. 74. 1st vibration mode of multilayered membrane

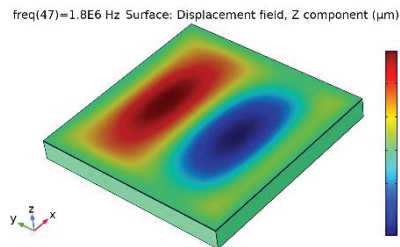


Fig. 75. 2nd vibration mode of multilayered membrane

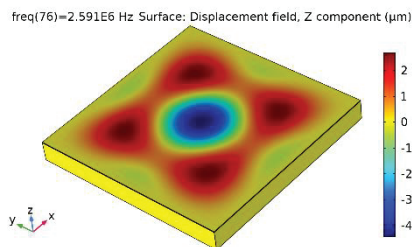


Fig. 76. 3rd vibration mode of multilayered membrane

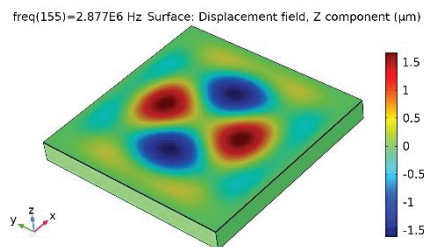


Fig. 77. 4th vibration mode of multilayered membrane

The 1st vibration mode of the multilayered membrane was registered at 1.006 MHz, 2nd at 1.800 MHz, 3rd at 2.591 MHz, and 4th at 2.877 MHz. For the subsequent numerical studies, only the 1st vibration mode will be considered.

The highest stress is recorded on the fixed edges in the model. Additionally, a clear stress zone can be seen in the middle of the membrane where it reaches approximately 3.5 MPa. The simulation was completed by calculating results in the interval of external pressure starting from 10 kPa to 100 kPa in 10 kPa steps. The Aluminum yield strength was 7 MPa. The maximum allowed external pressure was calculated to equal 54 kPa. Fig. 78 represents von Mises stress distribution in the membrane at its maximum value just before break. The change of stress at the edge of the membrane affected by the change of external pressure is given in Fig. 79.

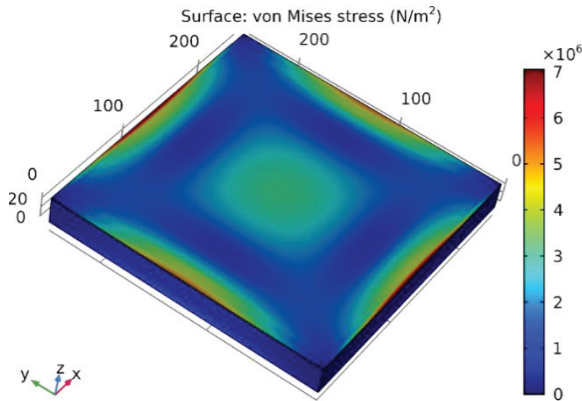


Fig. 78. Von Mises stress distribution on the membrane

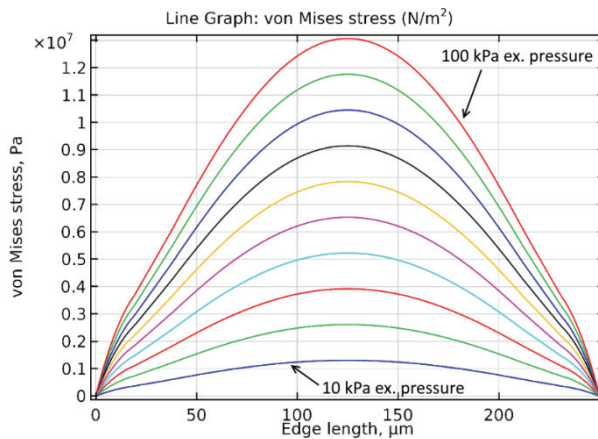


Fig. 79. Stress distribution on the edge of the membrane

In Fig. 79, it is clearly seen that the highest stress zone is in the middle of the edge – i.e., at the 125 μm point. Linear dependence of the stress magnitude on external pressure is also seen from all the curves given in the plot.

By taking a closer look at the center point of the membrane, the stress distribution here is also affected by the composition of the layers in the membrane (Fig. 80).

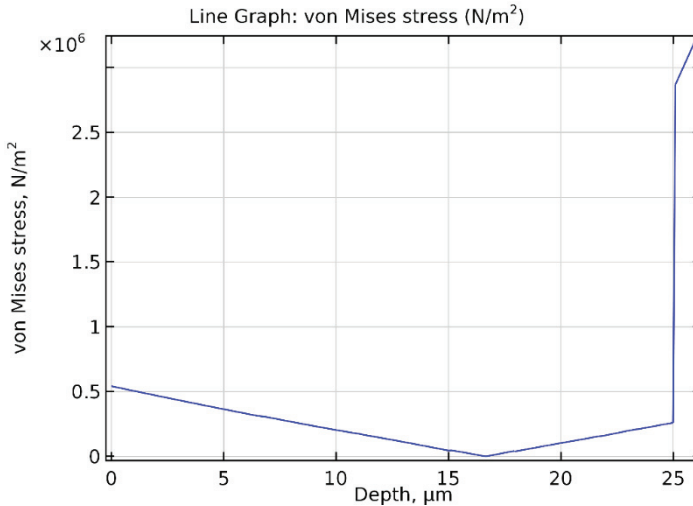


Fig. 80. Line graph of stress distribution by the depth of the membrane

The stress on the surface of the nanocomposite is higher compared to the middle part of it, as it is clearly stated by the decreasing value of stress. On the other hand, the stress starts to increase when the middle of the nanocomposite has been passed. At 25 μm depth, we reach Aluminum, where the stress becomes the highest as here rests the metal part of the membrane.

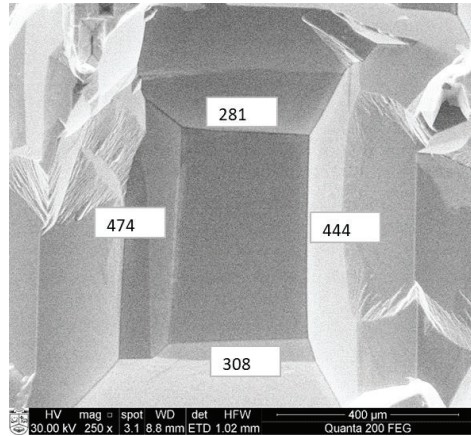
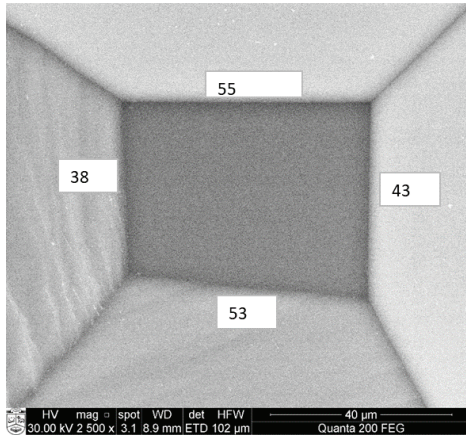
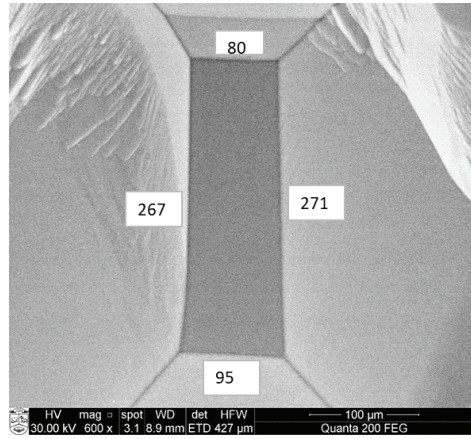
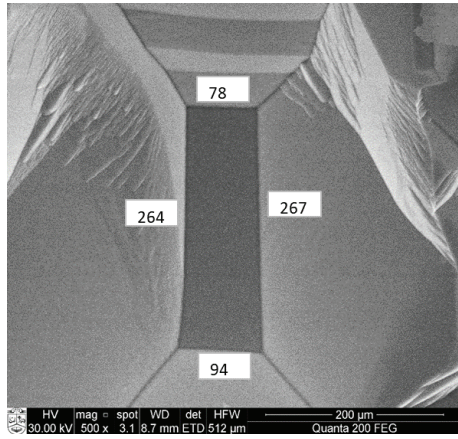
3.5. Fabrication of multilayered membrane

The results in Section 3.4. offer a clear picture of the possible performance of the multilayered membrane. Although the finite element model used for modeling the membrane does include boundary conditions which mimic the real world conditions, the properties of the simulated membrane can still be different from those received in our empirical analysis.

For the fabrication of a multilayered membrane from Aluminum and the novel piezoelectric composite, the vacuum evaporation methodology was employed. The in-depth description of this method is given in Section 3.1.2. The n-type $\langle 100 \rangle$ silicon substrate with a thickness of 380 μm was used for the membrane formation. The Low Pressure Chemical Vapor Deposition (LPCVD) process was used to deposit the low stress thermal silicon nitride (Si_3N_4) layer with a thickness of 500 nm on both sides of the double-sided polished substrate following backside photolithography by using a photomask with defined dimensions. The bottom layer of Si_3N_4 was etched by using the CF_4/O_2 plasma, thus making openings for the deep

etching of silicon. The deep etching of silicon was done through the substrate up to the top layer of Si_3N_4 by using 30% KOH solution ($T= 80\text{ }^\circ\text{C}$). Then, e-beam evaporation was used to deposit the Al layer (thickness 800 nm) on the top Si_3N_4 layer. Finally, the membrane was released by using CF_4/O_2 plasma in order to remove the top layer of Si_3N_4 .

Due to the limited accuracy during the fabrication process, it was hard to fabricate a membrane which would be the same as the one in the *COMSOL Multiphysics* model. Images of several defective membranes can be seen in Fig. 81.



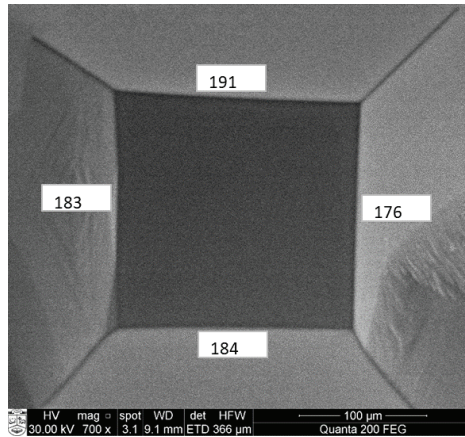


Fig. 81. Fabricated defective membranes

The defects shown in the pictures are the variability of edge dimensions. Also, they deviate from the intended outcome – i.e., 250 μm. All of them are in micrometers. The membranes in Fig. 80 could be used, but the properties of these membranes would differ significantly. Even though the membrane was fabricated with the intention to be of the square shape, all of those above, except for one, happened to be similar to the rectangle geometry. The last one, which is similar to a square membrane, features a much smaller edge than the one which was modeled. The defects occur due to irregular etching.

The best results were achieved with the membrane shown in Fig. 82. The edges of the fabricated membrane were 267 μm, 282 μm, 281 μm, and 252 μm. The fabricated membrane was taken as the analysis object as the error of the edge difference does fall into the acceptable range.

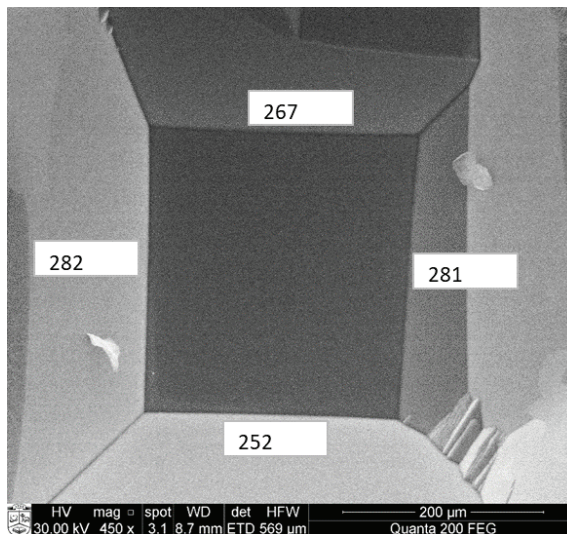


Fig. 82. Fabricated multilayered membrane with the closest geometry to the model

3.6. Finite element model verification

The fabricated membrane was analyzed with a laser Doppler vibrometer to calculate its frequency response to mechanical excitation. The membrane was excited with a periodical signal, and its center point was analyzed.

The steady-state response of the fabricated membrane due to harmonic mechanical excitation showed similar results to those achieved with the finite element model of the membrane (Fig. 83). The analysis represents a 4 μs time interval, during which, 4 periods of oscillation take place. The amplitude of the velocity changed from 3.2 m/s for the finite element model results to 2.8 m/s for the fabricated membrane. This is only 0.4 m/s difference, or 12.5% if we measure in percentage.

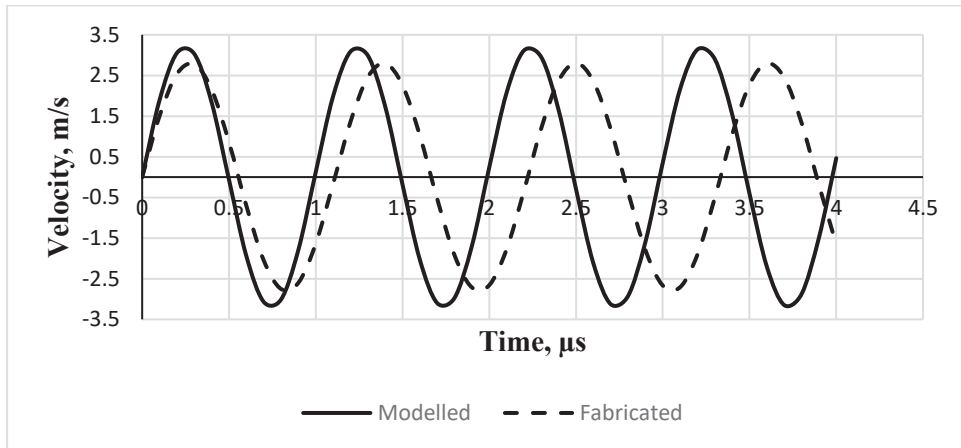


Fig. 83. Comparison of transient response of the finite element model membrane and the fabricated membrane

The resonant frequency of the multilayered membrane for the finite element model reaches 1006 kHz, while for the fabricated membrane it equals 900 kHz. It is a 106 kHz difference, or 11.5% difference between the two values.

Taking into account the fabrication and measurement errors, the differences are acceptable. The finite element model can be used for any further analysis as adequate representation of the oscillating membrane.

3.7. Vibrational analysis of loaded multilayered membrane

Resonant frequency analysis of a loaded multilayered membrane was completed. The membrane was acted upon by outside pressure. The pressure was increased from 0 Pa to 54 kPa in equal increments of 13.5 kPa. Table 24 shows the resonant frequency shift depending on the outside pressure magnitude.

Table 24. Resonant frequency shift of loaded multilayered membrane

Pressure, kPa	Resonant frequency, Hz	Δf , Hz
0	1005806	-
13.5	1005778	28
27	1005749.5	56.5
40.5	1005721	85
54	1005693	113

Here, only the 1st vibration mode is taken into account and analyzed. The change in kinetic energy is also evident (Fig. 84).

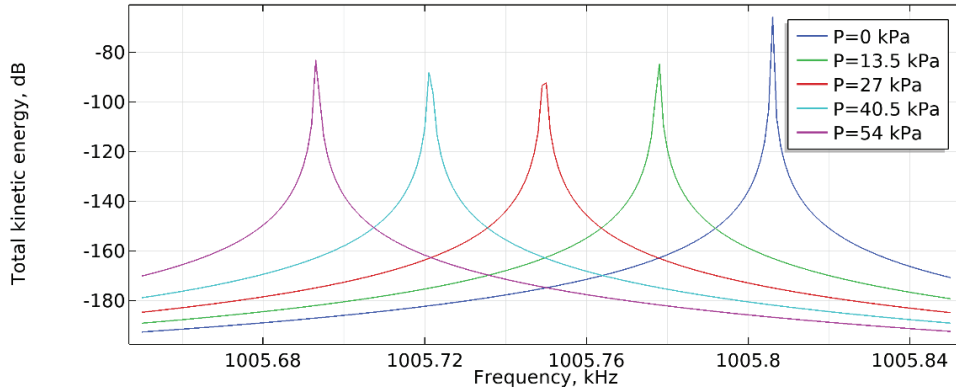


Fig. 84. Kinetic energy of the multilayered membrane dependency on the acting pressure

The lowest kinetic energy was registered during the loading of 27 kPa. The highest value was retrieved when the membrane was loaded with the maximum withstanding pressure of 54 kPa. A higher pressure is not possible as the membrane will rupture.

When calculating the vibrational amplitude for the multilayered membrane, an unloaded membrane was analyzed first (Fig. 85). The harmonically excited membrane can reach an amplitude of 3.6 μm . The highest value of the amplitude is located at the center of the membrane.

P(1)=0 kPa freq(115)=1005.8 kHz Surface: Displacement field, Z component (μm)

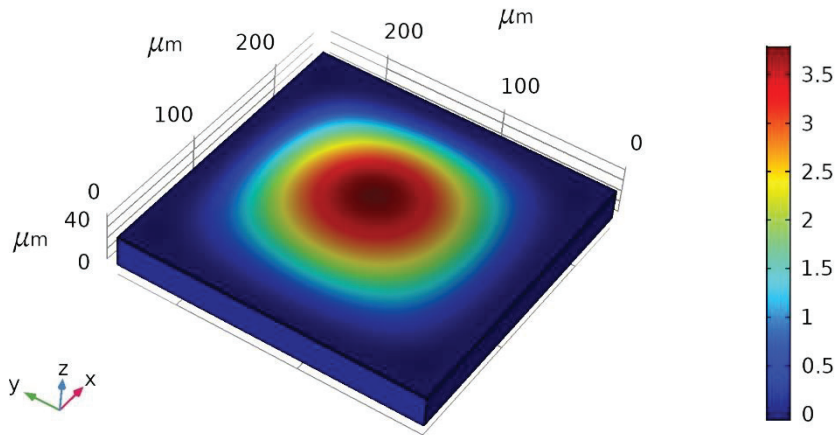


Fig. 85. Vibrational amplitude distribution of unloaded multilayered membrane

Loading the membrane with the maximum allowable external pressure of 54 kPa brought smaller values of the amplitude. The recorded value was 1.4 μm . These results are given in Fig. 86.

P(5)=54 kPa freq(115)=1005.8 Surface: Displacement field, Z component (μm)

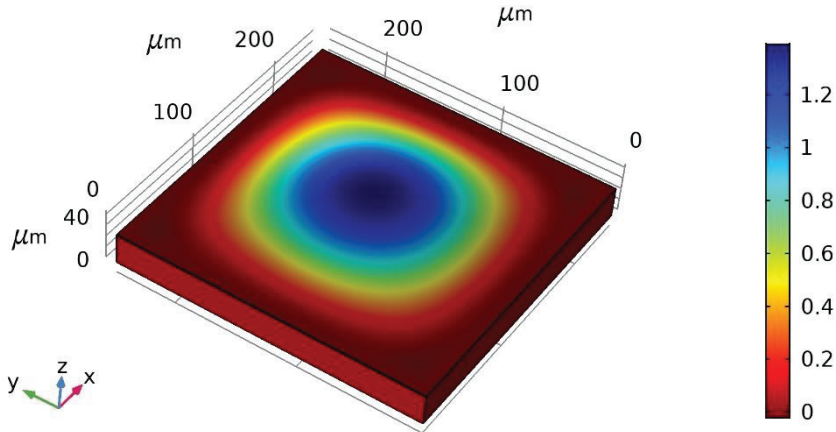


Fig. 86. Vibrational amplitude distribution of loaded multilayer membrane with 54 kPa external pressure

In order to fully understand how the amplitude of oscillations is dependent on the external pressure load, analysis of each external pressure load was completed (Fig. 87). The amplitude is exponentially dependable on the external load as it can be seen in the line graph. A significant decrease of the amplitude from a free oscillating to the maximally loaded element is also noted.

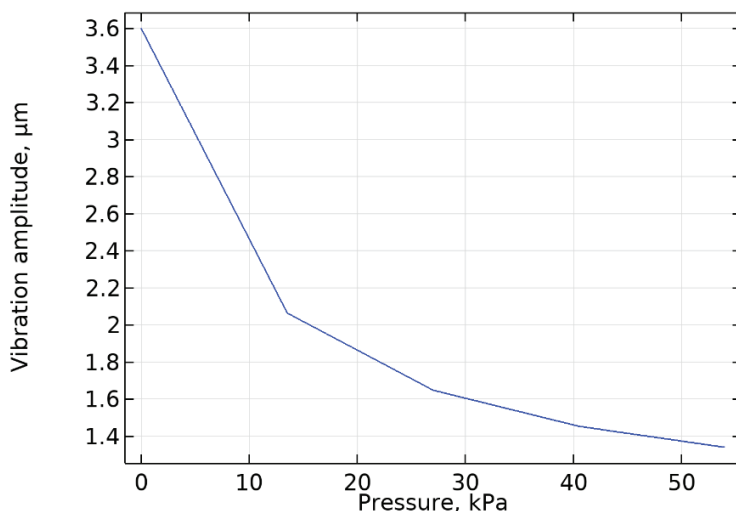


Fig. 87. Oscillations amplitude dependency on external pressure load

3.8. Optical properties of multilayered membrane

In order to ensure optical output from the sensor, the oscillating element has to feature adequate optical properties. Forming a periodical microstructure in the multilayered membrane allows registering diffraction efficiency changes when the oscillating element exhibits vibrations.

Due to the simultaneously working electrical and optical measurement techniques, the effectiveness of the sensing device increases significantly. Hot embossing, as stated in Paragraph 3.1.3. “Thermal embossing for microstructure imprinting,” was used to form a lamellar periodical microstructure (period $4\ \mu\text{m}$, depth $574\ \text{nm}$) in the PZT composite material at a temperature of $150\ ^\circ\text{C}$, $5\ \text{atm}$ pressure, and a holding time of $10\ \text{s}$ (Fig. 88).

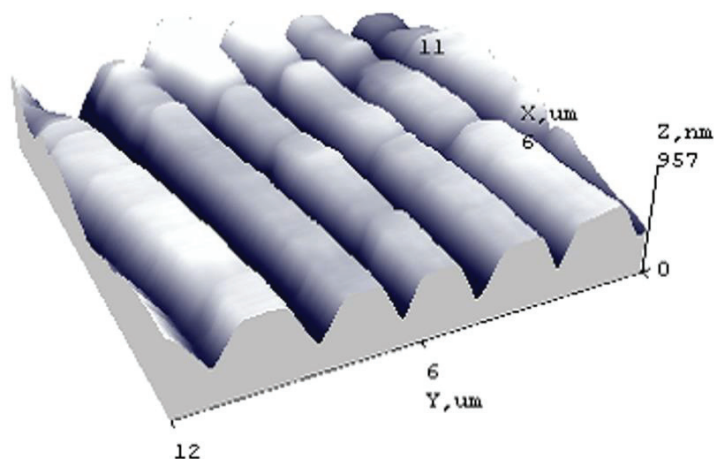


Fig. 88. 3D view of the periodical microstructure imprinted by using hot embossing technique in PMMA/PZT multilayered membrane

The periodical microstructure was imprinted in the composite material, which enables us to control the optical parameters as well as the mechanical properties of the microfluidic device as it was already analyzed in Paragraph 2.

In order to retrieve high quality optical output, the dependency of the diffraction efficiency and the angle of diffraction on the period change caused by the electrical signal was analyzed (Fig. 89).

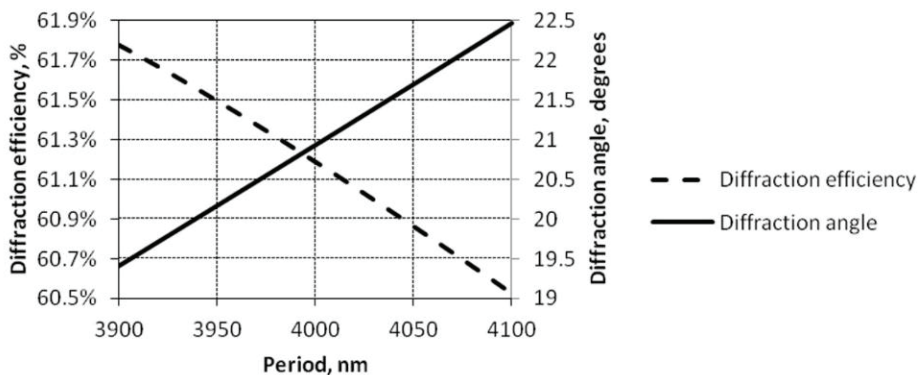


Fig. 89. Diffraction efficiency and diffraction angle versus period of periodical microstructure

The first diffraction maxima, as it is the main diffraction maxima used in technological approaches, was analyzed. A change of 0.1% of diffraction efficiency and about 0.15° diffraction angle was registered when the period changed by 10 nm.

3.9. Section conclusions

The following conclusions were drawn from the completed analysis:

- Further analysis of the selected piezoelectric composite PMMA/PZT has been completed. A pressure sensing membrane has been selected with the shape of a square. Three different shapes were compared: circular, rectangular, and square; the square shape ensures higher maximum stress and maximum deflection.
- A finite element model was created in the *COMSOL Multiphysics* software environment. A multilayered model consisting of aluminum – piezoelectric composite – aluminum has been developed.
- The highest kinetic energy during the modal analysis has been registered in the first and third vibration modes. Additionally, stress analysis has shown the highest stress concentration at the center of the membrane as well as in the middle of each edge.
- A multilayered membrane for a pressure sensor has been fabricated, and its frequency response has been analyzed. Only an insignificant error has been registered while comparing the frequency response of the modeled membrane and the fabricated one. This has verified the reliability of the

finite element model. All further analysis has been completed by using the finite element model.

- A clear amplitude dependency on the preload has been registered. The amplitude decreases with an increase of the membrane preload. The highest sustainable value of pressure which could be handled by the created membrane was 54 kPa. At this pressure, the vibration amplitude has reached 1.4 μm .
- The imprinted periodical microstructure has given the possibility for an optical output from the oscillating membrane. During membrane oscillations, its geometrical parameters change, which results in the change of the diffraction maxima efficiency and the diffraction angle change.

GENERAL CONCLUSIONS

A review of sensors in today's industry shows a vast number of possible types and their broad functionality, as well as their applicability to various science and commercial fields, such as pressure sensing. Even though there are many variants of pressure sensors, scientists still are in the search for small volume, low weight, low cost, high performance, low power consumption, and higher output signal properties of pressure sensors. In-depth analysis of sensor active elements revealed two possible approaches for the sensing element: cantilevers and membranes. The material selection for the sensing element makes a significant impact on its subsequent working properties and performance. Piezoelectric nanocomposites are the most promising sensing material which combines both, piezoelectric and polymer properties.

1. Three polymers have been selected for new piezoelectric nanocomposite formation. Polyvinyl butyral (PVB), polymethyl methacrylate (PMMA), and polystyrene (PS) have been selected due to their explicit properties of excellent flexibility, toughness, and strong binding, respectively. The structural and chemical composition, mechanical and electrical properties, and optical parameters have been selected to analyze the created novel piezoelectric nanocomposites.
2. Three piezoelectric nanocomposite materials have been developed: PS/PZT, PMMA/PZT, and PVB/PZT. The chemical analysis has shown that five elements were dominant in all samples: C, O, Ti, Zr, Pb. Chemical and morphological analysis has shown that the smoothest surface was achieved with the PMMA sample. Elemental bonds were the same in all the three samples as registered by FTIR. Investigation of the piezoresistive characteristics showed that the gauge factor of the PS/PZT sample was -3458.8 thus being the highest value. The resistance-force analysis revealed that all the samples had a clear start threshold which highly depends on the material of the binder. The highest capacitance was observed in the PMMA/PZT coating; it reached 0.20 pF. When investigating microresonators in the reverse piezoelectric effect, the measured current of PMMA/PZT linearly increased up to ~51 nA. The PMMA/PZT sample generated up to 2.5 mV voltage. The scratch test showed that the PMMA/PZT coating was almost twice as hard if compared to the other two values, i.e., the average critical load was 3.988 N. The vibrational amplitude and Young's modulus were investigated, and the registered results for the PMMA/PZT sample were 6.3 GPa and 164 nm. The PMMA/PZT sample has been selected for further fabrication and analysis.
3. When comparing geometrical shapes on the basis of Miedler-Reissner theory of analytical calculations, the shape of the square has been selected as the optimal geometry for the piezo-active membrane. The finite element method has been used to determine the vibration modes of the piezo-active membrane. The 1st vibration mode of the multilayered membrane has been

registered at 1.006 MHz. The modeled piezo-active membrane is able to withstand a pressure of 54 kPa.

4. The active element has been fabricated and analyzed regarding its capacity to behave under an external pressure load. Clear exponential dependency of the vibrational amplitude on an external pressure load has been determined. The resonant frequency shifts in the range of 0 to 54 Hz. The vibration amplitude decreases with the increased preload. At the maximum allowable external pressure, the membrane's oscillation amplitude is 1.4 μm . Periodical microstructure formation on the membrane enables optical sensor readout. The formatted periodical microstructure allows registering a dimensional change of the period as low as 0.25%.

LIST OF PUBLICATIONS

Publications indexed in the *Web of Science* with Impact Factor

International Publishers

1. [S1; CH] Cekas, Elingas; Janusas, Giedrius; Guobiene, Asta; Palevicius, Arvydas; Vilkauskas, Andrius; Ponelyte Urbaite, Sigita. Design of controllable novel piezoelectric components for microfluidic applications // *Sensors*. Basel: MDPI AG. ISSN 1424-8220. eISSN 1424-8220. 2018, vol. 18, iss. 11, art. no. 4049, p. 1–23. DOI: 10.3390/s18114049. [Science Citation Index Expanded (Web of Science); Scopus; Academic Search Complete] [IF: 3.031; AIF: 3.797; IF/AIF: 0.798; Q1 (2018, InCites JCR SCIE)] [FOR: T009] [Input: 0.170]
2. [S1; DE] Janušas, Giedrius; Palevičius, Arvydas; Čekas, Elingas; Brunius, Alfredas. Development and analysis of electro-optical microresonator with low range natural frequency // *Microsystem Technologies*. Berlin: Springer. ISSN 0946-7076. eISSN 1432-1858. 2017, Vol. 23, iss. 10, p. 4487–4493. DOI: 10.1007/s00542-016-3233-4. [Science Citation Index Expanded (Web of Science); Scopus; SpringerLink] [IF: 1.581; AIF: 4.361; IF/AIF: 0.362; Q3 (2017, InCites JCR SCIE)] [FOR: T009] [Input: 0.250]
3. [S1; US] Palevičius, Arvydas; Janušas, Giedrius; Čekas, Elingas; Šakalys, Rokas. Analysis of the influence of high-frequency excitation into quality of the replicated microstructure // *Experimental techniques*. New York, NY: Springer. ISSN 0732-8818. eISSN 1747-1567. 2016, vol. 40, iss. 4, p. 1285–1296. DOI: 10.1111/ext.12177. [Science Citation Index Expanded (Web of Science); Scopus; Current Contents / Engineering, Computing & Technology] [IF: 0.932; AIF: 1.969; IF/AIF: 0.473; Q3 (2016, InCites JCR SCIE)] [FOR: T009] [Input: 0.250]
4. [S1; DE] Šakalys, Rokas; Janušas, Giedrius; Palevičius, Arvydas; Čekas, Elingas; Jūrėnas, Vytautas; Sodah, Amer. Microstructures replication using high frequency excitation // *Microsystem technologies*. Berlin: Springer. ISSN 0946-7076. eISSN 1432-1858. 2016, vol. 22, iss. 7, p. 1831–1843. DOI: 10.1007/s00542-016-2858-7. [Science Citation Index Expanded (Web of Science); SpringerLink] [IF: 1.195; AIF: 4.100; IF/AIF: 0.291; Q3 (2016, InCites JCR SCIE)] [FOR: T001] [Input: 0.166]

National Publishers

1. [S1; LT] Janušas, Giedrius; Čekas, Elingas; Pilkauskas, Kęstutis; Mullaveettil, Farusil Najeeb. Numerical analysis of microresonator developed on the basis of PZT nanocomposite // *Mechanika*. Kaunas: KTU. ISSN 1392-1207. eISSN 2029-6983. 2017, vol. 23, iss. 5, p. 769–773. DOI: 10.5755/j01.mech.23.5.16308. [Science Citation Index Expanded (Web of Science); Scopus; Academic Search Complete] [IF: 0.529; AIF: 2.663; IF/AIF: 0.198; Q4 (2017, InCites JCR SCIE)] [FOR: T009] [Input: 0.250]

Publications indexed in the Web of Science without Impact Factor

International Publishers

1. [P1a; US] Cekas, Elingas; Janusas, Giedrius; Palevicius, Arvydas; Janusas, Tomas; Ciganas, Justas. Q-factor control of multilayer micromembrane using PZT composite material // SPIE BIOS: Microfluidics, BioMEMS, and Medical Microsystems XVI: 19 February 2018, San Francisco, California, United States / editors: Bonnie L. Gray, Holger Becker. Bellingham, WA: SPIE, 2018, art. 104910S. ISBN 9781510614680. p. 1–9. (Proceedings of SPIE, ISSN 0277-786X, eISSN 1996-756X; vol. 10491). DOI: 10.1117/12.2286618. [Conference Proceedings Citation Index – Science (Web of Science); Scopus] [FOR: T009] [Input: 0.200]
2. [P1a; US] Janušas, Giedrius; Guobienė, Asta; Palevičius, Arvydas; Brunius, Alfredas; Čekas, Elingas; Baltrušaitis, Valentinas; Šakalys, Rokas. Influence of binding material of PZT coating on microresonator's electrical and mechanical properties // Proceedings of SPIE: Smart sensors, actuators and MEMS VIII / edited by Luis Fonseca, Mika Prunnila, Erwin Peiner. Bellingham, WA: SPIE. ISSN 0277-786X. 2017, Vol. 10246, Article 102461E, p. 1–7. DOI: 10.1117/12.2265978. [Conference Proceedings Citation Index – Science (Web of Science); Scopus] [FOR: T009] [Input: 0.142]
3. [P1a; US] Janušas, Giedrius; Palevičius, Arvydas; Čekas, Elingas; Brunius, Alfredas; Baucė, Jokūbas. Development and analysis of new type microresonator with electro-optic feedback // Proceedings of SPIE: Optical modelling and design IV: Brussels, Belgium, April 03, 2016 / Frank Wyrowski; John T. Sheridan; Youri Meuret, eds. Bellingham, WA: SPIE. ISSN 0277-786X. 2016, vol. 9889, article 98891N, p. 1–8. DOI: 10.1117/12.2228789. [Conference Proceedings Citation Index – Science (Web of Science); Scopus] [FOR: T009] [Input: 0.200]
4. [P1a; US] Ostasėvičius, Vytautas; Malinauskas, Karolis; Janušas, Giedrius; Palevičius, Arvydas; Čekas, Elingas. Development and investigation of MOEMS type displacement-pressure sensor for biological information monitoring // Proceedings of SPIE: Optical sensing and detection IV: Brussels, Belgium, April 03, 2016. Bellingham, WA: SPIE. ISSN 0277-786X. 2016, vol. 9899, article 98992Q, p. 1–7. DOI: 10.1117/12.2228792. [Conference Proceedings Citation Index – Science (Web of Science); Scopus] [FOR: T009] [Input: 0.200]

National Publishers

1. [P1a; LT] Janušas, Giedrius; Palevičius, Arvydas; Čekas, Elingas; Rimkutė, Eligija. Development of finite element model for new type composite piezoelectric material // Mechanika 2016 : proceedings of the 21st international scientific conference, 12–13 May 2016, Kaunas University of Technology, Lithuania / Kaunas University of Technology, Lithuanian Academy of Science, IFTOMM National Committee of Lithuania, Baltic

Association of Mechanical Engineering. Kaunas: Kauno technologijos universitetas. ISSN 1822-2951. 2016, p. 98–102. [Conference Proceedings Citation Index – Science (Web of Science)] [FOR: T009] [Input: 0.250]

Articles in conference proceedings

International Publishers

1. [P1c; CH] Palevicius, Arvydas; Janusas, Giedrius; Cekas, Elingas; Patel, Yatinkumar Rajeshbhai. Composite piezoelectric material for biomedical micro hydraulic system // Bioinformatics and biomedical engineering: 6th international work-conference, IWBBIO 2018, Granada, Spain, April 25–27, 2018: proceedings / Ignacio Rojas, Francisco Ortuño (eds.). Cham: Springer, 2018. ISBN 9783319787589. eISBN 9783319787596. p. 49–58. (Lecture notes in computer science, ISSN 0302-9743, eISSN 1611-3349 ; vol. 10814). DOI: 10.1007/978-3-319-78759-6_5. [Scopus] [FOR: T009] [Input: 0.250]

REFERENCES

1. WANG, W. & SOPER, S. *Bio-MEMS: technologies and applications*. Boca Raton, FL, CRC, 2006. ISB 1420018671.
2. KAROONUTHAISIRI, N., CHARLERMROJ, R., UAWISETWATHANA, U., LUXANANIL, P., KIRTIKARA, K. & GAJANANDANA, O. Development of antibody array for simultaneous detection of foodborne pathogens. *Biosensors and Bioelectronics*. 2009, **24**(6), 1641-1648.
3. SANG, S. & WITTE, H. A novel PMDS micro membrane biosensor based on the analysis of surface stress. *Biosensors and Bioelectronics*. 2010, **25**(11), 2420-2424.
4. YE, J. M., PIVARNIK, P. E., SENEAL, A. G. & RAND, A. G. Rapid detection of staphylococcus aureus using a membrane fiber optic biosensor. *Pathogen Detection and Remediation for Safe Eating, Proceedings Volume 3544*. Boston, MA, United States, 12th January 1999.
5. MCGRAW, S. K., ALOCILJA, E., SENEAL, K. & SENEAL, A. A resistance based biosensor that utilizes conductive microfibers for microbial pathogen detection. *Open Journal of Applied Biosensors*. 2012, **1**(3), 36-43.
6. LI, D. P., FREY, M. W. & BAEUMNER, A. J. Electrospun polyactive acid nanofiber membranes as substrates for biosensor assemblies. *Journal of Membrane Science*. 2006, **279**(1-2), 354-363.
7. PARK, S., KIM, H., PAEK, S. H., HONG, J. W. & KIM, Y. K. Enzyme-linked immuno-strip biosensor to detect escherichia coli O157: H7. *Ultramicroscopy*. 2008, **108**(10), 1348-1351.
8. JAIN, S., CHATTOPADHYYAY, S., JACKERAY, R., ABID, C. K. V. Z., KOHLI, G. S. & SINGH, H. Highly sensitive detection of salmonella typhi using surface aminated polycarbonate membrane enhanced-ELISA. *Biosensors and Bioelectronics*. 2012, **31**(3), 37-43.
9. CONNELLY, J. T., KONDAPALLI, S., SKOUPPI, M., PARKER, J. S. L., KIRBY, B. J. & BAEUMNER, A. J. Micro-total analysis system for virus detection: microfluidic pre-concentration coupled to liposome-based detection. *Analytical and Bioanalytical Chemistry*. 2012, **402**(1), 315-323.
10. SUNG, Y. J., SUK, H. J., SUNG, H. Y., LI, T., POO, H. & KIM, M. G. Novel antibody/gold nanoparticle/magnetic nanoparticle nanocomposites for immunomagnetic separation and rapid colometric detection of staphylococcus aureus in mil. *Biosensors and Bioelectronics*. 2013, **43**(1), 432-439.
11. DADARWAL, R., NAMVAR, A., THOMAS, D. F., HALL, J. C. & WARRINER, K. Organic conducting polymer electrode based sensor for detection of salmonella infecting bacteriophages. *Material Science and Engineering*. 2009, **29**(3), 761-765.
12. LEWIS, C. L., CRAIG, C. C. & SENEAL, A. G. Mass and density measurements of live and dead gram-negative and gram-positive bacterial populations. *Applied and Environmental Microbiology*. 2014, **80**(12), 3622-3631.
13. WALDNER, J. B. *Nanocomputers and swarm intelligence*. London: ISTE John Wiley & Sons, 2008. ISBN 9781848210097.
14. *Merriam-Webster dictionary* [online]. 2019 [viewed 3 July 2019]. Available from <https://www.merriam-webster.com/dictionary/sensor>
15. PAWLAK, A. *Sensors and actuators in mechatronics: design and applications*. Boca Raton, FL, CRC, 2006. ISBN 9780849390135.
16. AHUJA, D. & PARANDE, D. Optical sensors and their applications. *Journal of Scientific Research and Reviews*. 2012, **1**(5), 60-68.

17. FIDANBOYLU, K. A. & EFENDIOGLU, H. S. Fibre optic sensor and their applications. *5th International Advanced Technologies Symposium (IATS'09)*. Karabük University, 2009.
18. JOHN, C. Optical sensing: the last frontier for enabling intelligence in our wired up world and beyond. *Photonic Sensors*. 2012, **2**(3), 193-202.
19. YAN, D., YANG, Y., HONG, Y., LIANG, T., YAO, Z., CHEN, X. & XIONG, J. Low-cost wireless temperature measurement: design, manufacture, and testing of a PCB-based wireless passive temperature sensor. *Sensors*. 2018, **18**(2), 532.
20. VAN HERWAARDEN, A. W. & SARRO, P. M. Thermal sensor based on the Seebeck effect. *Sensors and Actuators*. 1986, **10**(3-4), 321-346.
21. PLATT, R. B. & WOLF, J. N. General uses and methods of thermistors in temperature investigations, with special reference to a technique for high sensitivity contact temperature measurement. *Plant Physiology*. 1950, **25**(3), 507-512.
22. LEE, E., AHN, J., SHIN, S. & LEE, K. Comparative analysis of active inrush current limiter for high-voltage DC power supply system. *IEEE Vehicle Power and Propulsion Conference*. Seoul, South Korea, 9-12 October 2012, IEEE.
23. MUKHERJEE, R., BASU, J., MANDAL, P. & GUHA, P. K. A review of micromachined thermal accelerometers. *Journal of Micromechanics and Microengineering*. 2017, **27**(12), 18.
24. FENLAN, X., XIUYAN, L., YUE, S., LUHAI, L., WEI, W., LIANG, H. & RUPING L. Recent developments for flexible pressure sensors: A Review. *Micromachines*. 2018, **9**(11), 580.
25. ALBERI, M., BALDONCINI, M., BOTTARDI, C., CHIARELLI, E., FIORENTINI, G., RAPTIS, K. G. C., REALINI, E., REGUZZONI, M., ROSSI, L., SAMPIETRO, D., STRATI, V. & MANTOVANI, F. Accuracy of flight altitude measured with low-cost GNSS, radar and barometer sensors: Implications for airborne radiometric surveys. *Sensors*. 2017, **17**(8), 1889.
26. LAMMERINK, T. S. J., TAS, N. R., ELWENSPOEK, M. & FLUITMAN, J. H. J. Micro-liquid flow sensors. *Sensors and Actuators A: Physical*. 1993, **1993**(37), 45-50.
27. PENDLETON, R. & TUTTLE, M. E. *Fundamental strain-gage technology. manual on experimental methods for mechanical testing of composites*. Springer Netherlands, 1989. ISBN 978-94-009-1129-1.
28. TUTAK, P. Application of strain gauges in measurements of strain distribution in complex objects. *Journal of Applied Computer Science Methods*. 2014, **6**(2), 135-145.
29. EDWARDSON, S. P., WATKINS, K. G., DEARDEN, G., FRENCH, P. & MAGEE, J. strain gauge analysis of laser forming. *ICALEO 2002: 21st International Congress on Laser Materials Processing and Laser Microfabrication*. Scottsdale, Arizona, USA, 14-17 October 2002, Journal of Laser Applications.
30. GRAY, W. P., PALMER, J. D., GILL, J., GARDNER, M. & IANNOTTI, F. A clinical study of parenchymal and subdural miniature strain-gauge transducers for monitoring Intracranial Pressure. *Neurosurgery*. 1996, **39**(5), 931-932.
31. ALOMARI, M. A., SOLOMITO, A., REYES, R., KHALIL, S. M., WOOD, R. H. & WELSH, M. A. Measurements of vascular function using strain-gauge plethysmography: technical considerations, Standardization, and Physiological Findings. *American Journal of Physiology, Heart and Circulatory Physiology*. 2004, **286**(1), 99-107.
32. LIN, C., ZHAO, Z., KIM, J. & HUANG, J. Pencil drawn strain gauges and chemiresistors on paper. *Scientific Reports*. 2014, **4**, 3812.
33. HERNANDEZ, W. Improving the response of a load cell by using optimal filtering. *Sensors*. 2006, **6**(7), 697-711.

34. BOSCHETTI, G., CARACCILOLO, R., RICHIEDEI, D. & TREVISANI, A. Model-based dynamic compensation of load cell response in weighing machines affected by environmental vibrations. *Mechanical Systems and Signal Processing*. 2013, **34**(1-2), 116-130.
35. VERKERKE, G. J., SCHRAFFORDT KOOPS, H. & VETH, R. P. H. Design of a load cell for the Wagner distractor. *Journal of Engineering in Medicine*. 1989, **203**(2), 91-96.
36. LEE, H. J., BOX, G. N., ABRAHAM, J. B. A., ELCHICO, E. R., PANAH, R. A., TAYLOR, M. B., MOSKOWITZ, R., DEANE, L. A., MCDUGALL, E. M. & CLAYMAN, R. V. Laboratory evaluation of laparoscopic vascular clamps using a load-cell device – are all clamps the same?. *The Journal of Urology*. 2008, **180**(4), 1267-1272.
37. FLEMING, W. J. Overview of automotive sensors. *IEEE Sensors Journal*. 2001, **1**(4), 296-308.
38. BRASSEUR, G. A robust capacitive angular position sensor. *Quality Measurement: The Indispensable Bridge between Theory and Reality (No Measurements? No Science! Joint Conference – 1996: IEEE Instrumentation and Measurement Technology Conference and IMEKO Tec*. Brussels, Belgium, 4-6 June 1996, IEEE.
39. SECO, F., MARTIN, J. M., JIMENEZ, A. R. & CALDERON, L. A high accuracy magnetostrictive linear position sensor. *Sensors and Actuators A: Physical*. 2005, **123**(4), 216-223.
40. OBERLE, M., REUTEMANN, R., HERTLE, R. & HUANG, Q. A 10-mW two-channel fully integrated system-on-chip for eddy-current position sensing [in biomedical devices]. *IEEE Journal of Solid-State Circuits*. 2002, **37**(7), 916-925.
41. FERRAZZIN, D., DI DOMIZIO, G., SALSEDO, F., AVIZZANO, C. A., TECCHIA, F. & BERGAMASCO, M. Hall effect sensor-based linear transducer. *8th IEEE International Workshop on Robot and Human Interaction. RO-MAN '99*. Pisa, Italy, 27-29 September 1999, IEEE.
42. RUHAR, D., MAMIN, H. J., SHERWOOD, M. H., KIM, M., RETTNER, C. T., OHNO, K. & AWSCHALOM, D. D. Proton magnetic resonance imaging using a nitrogen – vacancy spin sensor. *Nature Nanotechnology*. 2015, **10**(2), 120-124.
43. NAGAOKA, T. & UCHIYAMA, A. Development of a small wireless position sensor for medical capsule devices. *The 26th Annual International Conference of the IEEE Engineering in Medicine and Biology Society*. San Francisco, CA, USA, 1-5 September 2004, IEEE.
44. BAI, S. & TEO, M. Y. Kinematic calibration and pose measurement of a medical parallel manipulator by optical position sensors. *Journal of Robotic Systems*. 2003, **20**(4), 419-424.
45. DE VOLDER, M., COOSEMANS, J., PUERS, R. & REYNAERTS, D. Characterization and control of a pneumatic microactuator with an integrated inductive position sensor. *Sensors and Actuators A: Physical*. 2008, **141**(1), 192-200.
46. HUANG, M. S. Cavity pressure based grey prediction of the filling-to-packing switchover point for injection molding. *7th International Conference on Control, Automation, Robotics and Vision, 2002. ICARCV 2002*. Singapore, 2-5 December 2002, IEEE.
47. SAGGIO, G., RIILLO, F., SBERNINI, L. & QUITADAMO, L. R. Resistive flex sensors: a survey. *Smart Materials and Structures*. 2016, **25**(1).
48. ALAPATI, S. & SHIVRAJ, Y. A review on applications of flex sensors. *International Journal of Emerging Technology and Advanced Engineering*. 2017, **7**(7).
49. TAO, L. Q., TIAN, H., LIU, Y., JU, Z. Y., PANG, Y., CHEN, Y. Q., WANG, D. Y., TIAN, X. G., YAN, J. C., DENG, N. Q., YANG, Y. & REN, T. L. An intelligent artificial throat with sound-sensing ability based on laser induced graphene. *Nature Communications*. 2017, **8**, 14579.

50. ATMOKO, H., TAN, D. C., TIAN, G. Y. & FAZENDA, B. Accurate sound source localization in a reverberant environment using multiple acoustic sensors. *Measurement Science and Technology*. 2008, **19**(2).
51. WANG, Y., YANG, T., LAO, J., ZHANG, R., ZHANG, Y., ZHU, M., LI, X., ZANG, X., WANG, K., YU, W., JIN, H., WANG, L. & ZHU, H. Ultra-sensitive graphene strain sensor for sound signal acquisition and recognition. *Nano Research*. 2015, 8(5), 1627-1636.
52. RUFFIER, F., BENACCHIO, S., EXPERT, F. & OGAM, E. A tiny directional sound sensor inspired by crickets designed for micro-air vehicles. *Sensors, 2011 IEEE*. Limerick, Ireland, 28-31 October 2011, IEEE.
53. TOUSE, M., SINIBALDI, J. & KARUNASIRI, G. MEMS directional sound sensor with simultaneous detection of two frequency bands. *Sensors, 2010 IEEE*. Kona, HI, USA, 1-4 November 2010, IEEE.
54. *Schematic representation of the working process of an ultrasonic sensor* [online]. 2019 [viewed on 9 July 2019]. Available from <https://www.keyence.com/ss/products/sensor/sensorbasics/ultrasonic/info/>
55. PARK, W. J., KIM, B. S., SEO, D. E., KIM, D. S. & LEE, K. H. Parking space detection using ultrasonic sensor in parking assistance system. *2008 IEEE Intelligent Vehicles Symposium*. Eindhoven, Netherlands, 4-6 June 2008, IEEE.
56. KHURI-YAKUB, B. T. & ORALKAN, O. Capacitive micromachined ultrasonic transducers for medical imaging and therapy. *Journal of Micromechanics and Microengineering*. 2011, **21**(5), 54004-54014.
57. FUCHS, S. I., STURZ, J., JUNGE, S., BALLMANN, M. & GAPPA, M. A novel sidestream ultrasonic flow sensor for multiple breath washout in children. *Pediatric Pulmonology*. 2008, **43**(8), 731-738.
58. CHENG, T. C., CHEN HSU, C. W., WANG, H. C. & TSAI, T. H. A low-power oscillator-based readout interface for medical ultrasonic sensors. *2016 International Symposium on VLSI Design, Automation and Test (VLSI-DAT)*. Hsinchu, Taiwan, 25-27 April 2016, IEEE.
59. GAO, F. & ZHENG, Y. M. Experimental study on measuring sound velocity and distance using ultrasonic sensor. *Transducer and Microsystem Technologies*. 2009, **11**.
60. LEE, S. K., BUXTON, W. & SMITH, K. C. A multi-touch three dimensional touch-sensitive tablet. *CHI '85 Proceedings of the SIGCHI Conference on Human Factors in Computing Systems*. San Francisco, California, USA, 1985, ACM SIGCHI Bulletin.
61. UNANDER, T., NILSSON, H. E. & OELMANN, B. Printed touch sensor for interactive packaging and display. *Polytronic 2007 – 6th International Conference on Polymers and Adhesives in Microelectronics and Photonics*. Tokyo, Japan, 15-18 January 2007.
62. KOYAMA, S., SUGIURA, Y., OGATA, M., WITHANA, A., UEMA, Y., HONDA, M., YOSHIZU, S., SANNOMIYA, C., NAWA, K. & INAMI, M. Multi-touch steering wheel for in-car tertiary applications using infrared sensors. *AH '14 Proceedings of the 5th Augmented Human International Conference*. Kobe, Japan, 7-8 March 2014, ACM New York.
63. PRASAD, S., MAHALAKSHMI, P., SUNDER, A. J. C. & SWATHI, R. Smart Surveillance Monitoring System Using Raspberry PI and PIR Sensor. *(IJCSIT) International Journal of Computer Science and Information Technologies*. 2014, **5**(6), 621-624.
64. TSAI, C. H., BAI, Y. W., CHU, C. A., CHUNG, C. Y. & LIN, M. B. PIR-sensor-based lighting device with ultra-low standby power consumption. *2011 IEEE International Instrumentation and Measurement Technology Conference*. Binjiang, China, 10-12 May 2011.

65. *Tilt sensor working principle* [online]. 2013-2019 [viewed on 9 July 2019]. Available from <https://www.elprocus.com/tilt-sensor-types-working-principle-and-its-applications/>
66. MARTINEZ, K., HART, J. K. & ONG, R. Environmental sensor networks. *Computer*. 2004, **37**(8), 50-56.
67. CHONG, C. Y. & KUMAR, S. P. Sensor networks: evolution opportunities and challenges. *Proceedings of the IEEE*. 2003, **91**(8), 1247-1256.
68. AKYILDIZ, I. F., SU, W., SANKARASUBRAMANIAM, Y. & CAYIRCI, E. A Survey on sensor networks. *IEEE Communications Magazine*. 2002, **40**(8), 102-114.
69. DAI, R., STEIN, R. B., ANDREWS, B. J., JAMES, K. B. & WIELER, M. Application of tilt sensors in functional electrical stimulation. *IEEE Transactions on Rehabilitation Engineering*. 1996, **4**(2), 63-72.
70. CHENG, Y., WINTERFLOOD, J., JU, L. & BLAIR, D. G. Tilt sensor and servo control system for gravitational wave detection. *Classical and Quantum Gravity*. 2002, **19**(7), 1723.
71. YAMAZOE, N. & SHIMANOE, K. New perspectives of gas sensor technology. *Sensors and Actuators B: Chemical*. 2009, **138**(1), 100-107.
72. DAHIYA, R. S. & VALLE, M. Tactile sensing for robotic applications. *Sensors: Focus on Tactile, Force and Stress Sensors*. 2008.
73. KHOSHNOUD, F. & DE SILVA, C. W. Recent advances in MEMS sensor technology-biomedical applications. *IEEE Instrumentation and Measurement Magazine*. 2012, **15**(1), 8-14.
74. LIU, W., LIU, N., YUE, Y., RAO, J., CHENG, F., SU, J., LIU, Z. & GAO, Y. Piezoresistive pressure sensor based on synergistical innerconnect polyvinyl alcohol nanowires/wrinkled graphene film. *Small*. 2018, **14**(15).
75. CHEN, Z., WANG, Z., LI, X., LIN, Y., LUO, N., LONG, M., ZHAO, N. & XU, J. B. Flexible piezoelectric-induced pressure sensors for static measurements based on nanowires/graphene heterostructures. *ACS Nano* 2017. 2017, **11**(5), 4507-4513.
76. HE, Z., CHEN, W., LIANG, B., LIU, C., YANG, L., LU, D., MO, Z., ZHU, H., TANG, Z. & GUI, X. Capacitive pressure sensor with high sensitivity and fast response to dynamic interaction based on graphene and porous nylon networks. *ACS Applied Materials & Interfaces* 2018. 2018, **10**(15), 12816-12823.
77. WEIB, K. & WORN, H. The working principle of resistive tactile sensor cells. *IEEE International Conference on Mechatronics and Automation, 2005*. Niagara Falls, Ont., Canada, 29 July – 1 August 2005, IEEE.
78. *Piezoelectric ceramic disk, EQ ultrasound* [online]. 2019 [viewed on 29 September 2019]. Available from <https://www.equtrasound.com/general-info-about-therapeutic-ultrasound/>.
79. LANG, S. B. & MUENSIT, S. Review of some lesser-known applications of piezoelectric and pyroelectric polymers. *Applied Physics A*. 2006, **85**(2), 125-134.
80. *Tekscan, "FlexiForce Force Sensors"* [online]. 2019 [viewed on 25 July 2019]. Available from <http://tekscan.com/interface-pressure-measurement-options>.
81. TIWANA, M. I., REDMOND, S. J. & LOVELL, N. H. A review of tactile sensing technologies with applications in biomedical engineering. *Sensors and Actuators A: Physical*. 2012, **179**, 17-31.
82. MAHESHWARI, V. & SARAF, R. Tactile devices to sense touch on a par with a human finger. *Angewandte Chemie International Edition*. 2008, **47**(41), 7808-7826.
83. YAO, J. J., ARNEY, S. C. & MACDONALD, N. C. Fabrication of high frequency two-dimensional nanoactuators for scanned probe devices. *Journal of Microelectromechanical Systems*. 1992, **1**(1), 14-22.

84. YEH, R., HOLLAR, S. & PISTER, K. S. J. Single mask, large force, and large displacement electrostatic linear inchworm motors. *Journal of Microelectromechanical Systems*. 2002, **11**(4), 260-264.
85. MINAMI, K., KAWAMURA, S. & ESASHI, M. Fabrication of distributed electrostatic micro actuator (DEMA). *Journal of Microelectromechanical Systems*. 1993, **2**(3), 121-127.
86. LEE, K. B. & CHO, Y. Laterally driven electrostatic repulsive-force microactuators using asymmetric field distribution. *Journal of Microelectromechanical Systems*. 2001, **10**(1), 128-136.
87. ZHAO, Y. & CUI, T. Fabrication of high-aspect-ratio polymer-based electrostatic comb drives using the hot embossing technique. *Journal of Micromechanics and Microengineering*. 2003, **13**(3), 430-435.
88. MITA, M., ARAI, M., TENSAKA, S., KOBAYASHI, D. & FUJITA, H. A micromachined impact microactuator driven by electrostatic force. *Journal of Microelectromechanical Systems*. 2003, **12**(1), 37-41.
89. LI, L., BROWN, J. G. & UTTAMCHANDANI, D. Study of scratch drive actuator force characteristics. *Journal of Micromechanics and Microengineering*. 2002, **12**(6).
90. LEE, H. S., LEUNG, C. H., SHI, J., CHANG, S. C., LORINCZ, S. & NEDELESCU, I. Integrated microrelays: concept and initial results. *Journal of Microelectromechanical Systems*. 2002, **11**(2), 147-153.
91. SHIKIDA, M., SATO, K. & HARADA, T. Fabrication of an S-shaped microactuator. *Journal of Microelectromechanical Systems*. 1997, **6**(1), 18-24.
92. LAGTENBERG, R., GILBERT, J., SENTURIA, S. D. & ELWENSPOEK, M. Electrostatic curved electrode actuators. *Journal of Microelectromechanical Systems*. 1997, **6**(3), 257-265.
93. KOGANEZAWA, S., UEMATSU, Y., YAMADA, T., NAKANO, H., INOUE, J. & SUZUKI, T. Dual-stage actuator system for magnetic disk drives using a shear mode piezoelectric microactuator. *IEEE Transactions on Magnetics*. 1999, **35**(2), 988-992.
94. ZHANG, Q. Q., GROSS, S. J., TADIGADAPA, S., JACKSON, T. N., DJUTH, F. T. & TROLIER-MCKINSTRY, S. Lead zirconate titanate films for d33 mode cantilever actuators. *Sensors and Actuators A: Physical*. 2003, **105**(1), 91-97.
95. BUTLER, J. T., BRIGHT, V. M. & COWAN, W. D. Average power control and positioning of polysilicon thermal actuators. *Sensors and Actuators A: Physical*. 1999, **72**(1), 88-97.
96. SEHR, H., TOMLIN, I. S., HUANG, B., BEEBY, S. P., EVANS, A. G. R., BRUNNSCHWEILER, A., ENSELL, G. J., SCHABMUELLER, C. G. J. & NIBLOCK, T. E. G. Time constant and lateral resonances of thermal vertical bimorph actuators. *Journal of Micromechanics and Microengineering*. 2002, **12**(4).
97. LU, T. J., HUTCHINSON, J. W. & EVANS, A. G. Optimal design of a flexular actuator. *Journal of the Mechanics and Physics of Solids*. 2001, **49**(9), 2071-2093.
98. MOULTON, T. & ANANTHASURESH, G. K. Micromechanical devices with embedded electro-thermal-compliant actuation. *Sensors and Actuators A: Physical*. 2001, **90**(1-2), 38-48.
99. ROCH, I., BIDAUD, P., COLLARD, D. & BUCHAILLOT, L. Fabrication and characterization of an SU-8 gripper actuated by a shape memory alloy thin film. *Journal of Micromechanics and Microengineering*. 2003, **13**(2).
100. CARLEN, E. T. & MASTRANGELO, C. H. Electrothermally activated paraffin microactuators. *Journal of Microelectromechanical Systems*. 2002, **11**(3), 165-174.

101. GOMM, T., HOWELL, L. L. & SELFRIDGE, R. H. In-plane linear displacement bistable microrelay. *Journal of Micromechanics and Microengineering*. 2002, **12**(1), 257-264.
102. KHOO, M. & LIU, C. Micro magnetic silicone elastomer membrane actuator. *Sensors and Actuators A: Physical*. 2001, **89**(3), 259-266..
103. CHO, H. J. & AHN, C. H. A bidirectional magnetic microactuator using electroplated permanent magnet arrays. *Journal of Microelectromechanical Systems*. 2002, **11**(1), 78-84.
104. BOUROUINA, T., LEBRASSEUR, E., REYNE, G., DEBRAY, A., FUJITA, H., LUDWIG, A., QUANDT, E., MURO, H., OKI, T. & ASAOKO, A. Integration of two degree-of-freedom magnetstrictive actuation and piezoresistive detection: application to a two-dimensional optical scanner. *Journal of Microelectromechanical Systems*. 2002, **11**(4), 355-361.
105. RUAN, M., SHEN, J. & WHEELER, C. B. Latching micromagnetic relays. *Journal of Microelectromechanical Systems*. 2001, **10**(4), 511-517.
106. VELDHUIS, S. A., BOIX, P. B., YANTARA, N., LI, M., SUM, T. C., MATHEWS, N. & MHAISALKAR, S. G. Perovskite materials for light-emitting diodes and lasers. *Advanced Materials*. 2016, **28**(32), 6804-6834.
107. ZHAO, D., FAN, F., CHENG, J., ZHANG, Y., WONG, K. S., CHIGRINOV, V. G., KWOK, H. S., GUO, L. & TANG, B. Z. Light-emitting liquid crystal displays based on an aggregation-induced emission luminogen. *Advanced Optical Materials*. 2014, **3**(2).
108. FUENTES, J. L. M., FERNANDEZ, E. J., PRIETO, P. M. & ARTAL P. Interferometric method for phase calibration in liquid crystal spatial light modulators using a self-generated diffraction-grating. *Optics Express*. 2016, **24**(13), 14159-14171.
109. GUPTA, S., PAHWA, T., NARWAL, R., PRASAD, B., & KUMAR, D.S. Optimizing the performance of MEMS electrostatic comb drive actuator with different flexure springs. *Proceedings of the 2012 COMSOL Conference in Bangalore*. Bangalore, India, 2-3 November 2012.
110. *Electrostatic harmonic motor* [online]. 2019 [viewed on 11 July 2019]. Available from <https://www.mcnc.org/>.
111. JUNG, B. C., YOON, H., OH, H., LEE, G., YOO, M., YOUN, B. D. & HUH, Y. C. Hierarchical model calibration for designing piezoelectric energy harvester in the presence of variability in material properties and geometry. *Structural and Multidisciplinary Optimization*. 2016, **53**(1), 161-173.
112. ZOLFAGHARIAN, A., KOUZANI, A. Z., KHOO, S. Y., MOGHADAM, A. A. A., GIBSON, I. & KAYNAK, A. Evolution of 3D printed soft actuators. *Sensors and Actuators A: Physical*. 2016, **250**(1), 258-272.
113. SHAN, J., LIU, Y., GABBERT, U. & CUI, N. Control system design for nano-positioning using piezoelectric actuators. *Smart Materials and Structures*. 2016, **25**(2).
114. LI, J., ZHOU, X., ZHAO, H., SHAO, M., LI, N., ZHANG, S. & DU, Y. Development of a novel parasitic-type piezoelectric actuator. *IEEE/ASME Transactions on Mechatronics*. 2017, **22**(1), 541-550.
115. YANG, T., CHEN, Y. & MINZIONI, P. A review on optical actuators for microfluidic systems. *Journal of Micromechanics and Microengineering*. 2017, **27**(12).
116. ASADNIA, M., KOTTAPALLI, A. G. P., SHEN, Z., MIAO, J. & TRIANTAFYLLOU, M. Flexible and surface-mountable piezoelectric sensor arrays for underwater sensing in marine vehicles. *IEEE Sensors Journal*. 2013, **13**(10), 3918-3925.
117. AQILAH, A., JAFFAR, A., BAHARI, S., LOW, C. Y. & KOCH, Y. Resistivity characteristics of single miniature tactile sensing element based on pressure sensitive

conductive rubber sheet. *2012 IEEE 8th International Colloquium on Signal Processing and Its Applications*. Melaka, Malaysia, 23-25 March 2012, IEEE.

118. CHOI, W. -C. Polymer micromachined flexible tactile sensor for three-axial loads detection. *Transactions on Electrical and Electronic Materials*. 2010, **11**(3), 130-133.

119. NODA, K., HASIMOTO, Y., TANAKA, Y. & SHIMOYAMA, I. MEMS on robot applications. *TRANSUCERS 2009 – 2009 International Solid-State Sensors, Actuators and Microsystems Conference*. Denver, CO, USA, 21-25 June 2009, IEEE.

120. LEE, H. -K., CHUNG, J., CHANG, S.-I. & YOON, E. Normal and shear force measurement using a flexible polymer tactile sensor with embedded multiple capacitors. *Journal of Microelectromechanical Systems*. 2008, **17**(4), 934-942.

121. TAKAO, H., SAWADA, K. & ISHIDA, M. Monolithic silicon smart tactile image sensor with integrated stain sensor array on pneumatically swollen single-diaphragm structure. *IEEE Transactions on Electron Devices*. 2006, **53**(5), 1250-1259.

122. SHAN, J. H., MEI, T., SUN, L., NI, L., MENG, M. & CHU, J. R. The design and fabrication of a flexible three-dimensional force sensor skin. *2005 IEEE/RSJ International Conference on Intelligent Robots and Systems*. Edmonton, Alta., Canada, 2-6 August 2005, IEEE.

123. KANE, B. J., CUTKOSKY, M. R. & KOVACS, G. T. A. A traction stress sensor array for use in high-resolution robotic tactile imaging. *Journal of Microelectromechanical Systems*. 2000, **9**(4), 425-434.

124. REY, P., CHARVET, P., DELAYE, M. T. & HASSAN, S. A. High density capacitive pressure sensor array for fingerprint sensor application. *Proceedings of the International Solid-State Sensors and Actuators Conference (Transducers '97)*. Chicago, IL, USA, 19 June 1997, IEEE.

125. FIORILLO, A. S. Design and characterization of a PVDF ultrasonic range sensor. *IEEE Transactions on Ultrasonics, Ferroelectrics, and Frequency Control*. 1992, **39**(6), 688-692.

126. BOISEN, A., DOHN, S., KELLER, S. S., SCHMID, S. & TENJE, M. Cantilever-like micromechanical sensors. *Reports on Progress in Physics*. 2011, **74**(3).

127. CHAUDHARY, M. & GUPTA, A. Microcantilever-based Sensors. *Defence Science Journal*. 2009, **59**(6), 634-641.

128. KOSAKA, P. M., TAMAYO, J., RUIZ, J. J., PUERTAS, S., POLO, E., GRAZU, V., DE LA FUENTE, J. M. & CALLEJA, M. Tackling reproducibility in microcantilever biosensors: a statistical approach for sensitive and specific end-point detection of immunoreactions. *The Analyst*. 2013, **138**(3), 863-872.

129. TORTONESE, M., BARRETT, R. C. & QUATE, C. F. Atomic resolution with an atomic force microscope using piezoresistive detection. *Applied Physics Letters*. 1993, **62**(834).

130. GEL, M. & SHIMOYAMA, I. Force sensing submicrometer thick cantilevers with ultra-thin piezoresistors by rapid thermal diffusion. *Journal of Micromechanics and Microengineering*. 2003, **14**(3).

131. TAKAHASHI, H., IWASE, E., MATSUMOTO, K. & SHIMOYAMA, I. Air flow sensor for an insect-like flapping wing. *2008 IEEE The 21st International Conference On Micro Electro Mechanical Systems*. Wuhan, China, 13-17 January 2008, IEEE.

132. TAKAHASHI, H., KAN, T., MATSUMOTO, K. & SHIMOYAMA, I. Simultaneous detection of particles and airflow with a MEMS piezoresistive cantilever. *Measurement Science and Technology*, 2013, **24** (2).

133. TAKAHASHI, H., MINH DUNG, N., MATSUMOTO, K. & SHIMOYAMA, I. Differential pressure sensor using a piezoresistive cantilever. *Journal of Micromechanics and Microengineering*. 2012, **22**(5).

134. NGUYEN, M. D., TAKAHASHI, H., UCHIYAMA, T., MATSUMOTO, K. & SHIMOYAMA, I. A barometric pressure sensor based on the air-gap scale effect in a cantilever. *Applied Physics Letters*. 2018, **103**(14), 143505-143540.
135. EATON, W. P., BITSIE, F., SMITH, J. H. & PLUMMER, D. W. A new analytical solution for diaphragm deflection and its application to a surface-micromachined pressure sensor. *TechConnect Briefs*. 1999, 640-643.
136. CEN, S. & SHANG, Y. Developments of Mindlin-Reissner Plate Elements. *Mathematical Problems in Engineering*. 2015, **2015**(1), 1-12.
137. LI, H., DENG, H., ZHENG, G., SHAN, M., ZHONG, Z. & LIU, B. Reviews on corrugated diaphragms in miniature fiber-optic pressure sensors. *Applied Sciences*. 2019, **9**(11).
138. LI, C., CORDOVILLA, F. & OCANA, J. L. The design and analysis of a novel structural piezoresistive pressure sensor for low pressure measurement. *Microsystem Technologies*. 2017, **23**(12).
139. GAO, Y., OTA, H., SCHALER, E. W., CHEN, K., ZHAO, A., GAO, W., FAHAD, H. M., LENG, Y., ZHENG, A., XIONG, F., ZHANG, C., TAI, L. C., ZHAO, P., FEARING, R. S. & JAVEY, A. Wearable microfluidic diaphragm pressure sensor for health and tactile touch monitoring. *Advanced Materials*. 2017, **29**(39).
140. STARR, P., BARTELS, K., MAULI AGRAWAL, C. & BAILEY, S. A thin-film pressure transducer for implantable and intravascular blood pressure sensing. *Sensors and Actuators A: Physical*. 2016, **248**(1), 38-45.
141. XU, T., WANG, H., XIA, Y., ZHAO, Z., HUANG, M., WANG, J., ZHAO, L., ZHAO, Y. & JIANG, Z. Piezoresistive pressure sensor with high sensitivity for medical application using peninsula-island structure. *Frontiers of Mechanical Engineering*. 2017, **12**(4).
142. LI, X., ZHEN, S., QIAN, K., LIANG, X., WANG, X., SHI, J., WU, X. & YU, B. A hear-resistance and high-sensitivity acoustic pressure sensor based on aluminum-polyimide diaphragm. *Sensors and Actuators A: Physical*. 2018, **279**(1), 75-78.
143. ZHANG, Z., LIAO, C., TANG, J., BAI, Z., GUO, K., HOU, M., HE, J., WANG, Y., LIU, S., ZHANG, F. & WANG, Y. High-sensitivity gas-pressure sensor based on fiber-tip PVB diaphragm Fabry-Perot interferometer. *Journal of Lightwave Technology*. 2017, **35**(18), 4067-4071.
144. NALLATHAMBI, A. & SHANMUGANANTHAM, T. Design of diaphragm based MEMS pressure sensor with sensitivity analysis for environmental applications. *Sensors & Transducers*. 2015, **188**(5), 48-54.
145. AMEZQUITA-SANCHEZ, J. P. & ADELI, H. Signal processing techniques for vibration-based health monitoring of smart structures. *Archives of Computational Methods in Engineering*. 2016, **23**(1), 1-15.
146. FARAG, S. G. Application of smart structural system for smart sustainable cities. *2019 4th MEC International Conference on Big Data and Smart City (ICBDSC)*. Muscat, Oman, 15-16 January 2019, IEEE.
147. ZELENIAKIENE, D., LEISIS, V., GRISKEVICIUS, P., BULDERBERGA, O. & ANISKEVICH, A. A numerical simulation of mechanical properties of smart polymer composite with microcapsules for damage sensing applications. *ECCM17 – 17th European Conference on Composite Materials*. Munich, Germany, 26-30 June 2016.
148. SAFARI, A. & AKDOGAN, E. K. *Piezoelectric and acoustic materials for transducer applications*. Springer, US, 2008. ISBN978-0-387-76538-9.
149. DUAN, W. H. & WANG, Q., QUEK, S. T. Applications of piezoelectric materials in structural health monitoring and repair: selected research examples. *Materials*. 2010, **3**(12), 5169-5194.

150. SHARMA, A., OLSZEWSKI, O. Z., TORRES, J., MATHEWSON, A. & HOULIHAN, R. Fabrication, simulation and characterization of MEMS piezoelectric vibration energy harvester for low frequency. *Procedia Engineering*. 2015, **120**(1), 645-650.
151. GUEGAN, Q. & FOULC, J. Dielectric response of electrorheological fluids: application to the electrical characterization of particles suspended in liquid medium. *2008 IEEE International Conference on Dielectric Liquids*. Futuroscope-Chasseneuil, France, 9 September 2008, IEEE.
152. EL FATNANI, F. Z., GUYOMAR, D., MAZROUI, M., BELHORA, F. & BOUGHALEB, Y. Optimization and improvement of thermal energy harvesting by using pyroelectric materials. *Optical Materials*. 2016, **56**(1), 22-26.
153. BORKAR, H., RAO, V., TOMAR, M., GUPTA, C., SCOTT, J. F. & KUMAR, A. Giant enhancement in ferroelectric polarization under illumination. *Materials today Communications*. 2018, **14**(1), 116-123.
154. UCHINO, K. *Piezoelectric composite materials. Advanced Piezoelectric Materials, Science and Technology*. Woodhead Publishing Series in Electronic and Optical Materials, Elsevier, 2010. ISBN 9781845695347.
155. *Polymer Properties Database* [online]. 2015 [viewed on 18 July 2019]. Available from <https://polymerdatabase.com/polymer%20classes/Polysulfone%20type.html>.
156. COYLE, T. & ANWAR, N. A novel approach to condom lubricant analysis: In-situ analysis of swabs by FT-Raman Spectroscopy and its effects on DNA analysis. *Science & Justice*. 2009, **49**(1), 32-40.
157. CHEN, S., ZANG, M., WANG, D., ZHENG, Z. & ZHAO, C. Finite element modelling of impact damage in polyvinyl butyral laminated glass. *Composite Structures*. 2016, **138**(1), 1-11.
158. LIN, Y., ZHU, C., ALVA, G. & FANG, G. Palmitic acid/polyvinyl butyral/expanded graphite composites as form-stable phase change materials for solar thermal energy storage. *Applied Energy*. 2018, **228**(1), 1801-1809.
159. RUAN, Y., SHI, P., LEI, Y., WENG, S., LI, S., HUANG, L., LIN, X. & YAO, H. Polyvinyl butyral/graphene oxide nanocomposite modified electrode for the integrate determination of terminal metabolites of catecholamines in human urine. *Journal of Electroanalytical Chemistry*. 2019, **848**(1).
160. SODERGARD, A & STOLT, M. Properties of lactic acid based polymers and their correlation with composition. *Progress in Polymer Science*. 2002, **27**(6), 1123-1163.
161. MIDDELTON, J. C. & TIPTON, A. J. Synthetic biodegradable polymers as orthopedic devices. *Biomaterials*. 2000, **21**(23), 2335-2346.
162. GIORDANO, R. A., WU, B. M., BORLAND, S. W., CIMA, L. G., SACHS, E. M. & CIMA, M. J. Mechanical properties of dense polyactic acid structures fabricated by three dimensional printing. *Journal of Biomaterials Science, Polymer Edition*. 1997, **8**(1), 63-75.
163. HUDA, M. S., DRZAL, L. T., MOHANTY, A. K. & MISRA, M. Chopped glass and recycled newspaper as reinforcement fibers in injection molded poly(lactic acid) (PLA) composites: A comparative study. *Composites Science and Technology*. 2006, **66**(11-12), 1813-1824.
164. HAMAD, K., KASEEM, M., YANG, H. W., DERI, F. & KO, Y. G. Properties and medical applications of polylactic acid: A review. *eXPRESS Polymer Letters*. 2015, **9**(5).
165. MCKEEN, L. W. *Permeability Properties of Plastics and Elastomers, 4th ed*. William Andrew: Oxford, UK, Elsevier, 2017. ISBN 9780323508599.
166. WYPYCH, G. *Handbook of Polymers, 2nd ed*. ChemTec Publishing, Toronto, Canada, Elsevier, 2016, ISBN 9781895198928.

167. MCKEEN, L. W. *Fatigue and Tribological Properties of Plastics and Elastomers*, 3rd ed. William Andrew: Oxford, UK, Elsevier, 2016. ISBN 9780323442015.
168. BRUNIUS, A. *Research and development of piezoelectric composite material for biomedical application*. PhD thesis, Kaunas University of Technology, 2018.
169. GAIKWAD, S. P., DHAGE, S. R. & RAVI, V. Co-precipitation method for the preparation of ferroelectric CaBi₄Ti₄O₁₅. *Journal of Materials Science: Materials in Electronics*. 2005, **16**(4), 229-231.
170. GOLDSTEIN, J. I., NEWBURY, D. E., MICHAEL, J. R., RITCHIE, N. W. M., SCOTT, J. H. J. & JOY, D. C. *Scanning electron microscopy and X-Ray microanalysis*. 3rd ed. Springer, US.
171. GOLDSMITH, C. S. & MILLER, S. E. Modern uses of electron microscopy for detection of viruses. *Clinical Microbiology Reviews*. 2009, **22**(4), 552-563.
172. REIMER L. *Scanning electron microscopy. Springer series in optical sciences*. Springer-Verlag Berlin Heidelberg, Germany, 1998, ISBN 978-3-540-63976-3.
173. STETSOVYCH, O., TODOROVIC, M., SHIMIZU, T. K., MORENO, C., RYAN, J. W., LEON, C. P., SAGISAKA, K., PALOMARES, E., MATOLIN, V., FUJITA, D., PEREZ, R. & CUSTANCE, O. Atomic species identification at the (101) anatase surface by simultaneous scanning tunneling and atomic force microscopy. *Nature Communications*. 2015, **6**, 7265.
174. BAKER, S. R., BENERJEE, S., BONIN, K. & GUTHOLD, M. Determining the mechanical properties of electrospun poly-ε-caprolactone (PCL) nanofibers using AFM and a novel fiber anchoring technique. *Materials Science and Engineering: C*. 2016, **59**, 2013-212.
175. LEKKA, M. Discrimination between normal and cancerous cells using AFM. *BioNanoScience*. 2016, **6**(1), 65-80.
176. GOLDSTEIN, J., NEWBURY, D. E., JOY, D. C., LYMAN, C. E., ECHLIN, P., LIFSHIN, E., SAWYER, L. & MICHAEL, J. R. *Scanning electron microscopy and X-ray microanalysis*. Springer, US, 2003. ISBN 978-0-306-47292-3.
177. *X-ray Spectroscopy. University of Michigan, Advanced Physics Laboratory* [online]. 2005 [viewed on 10 June 2019]. Available from http://instructor.physics.lsa.umich.edu/adv-labs/X-Ray_Spectroscopy/x_ray_spectroscopy_v2.pdf
178. *XFlash® 6 | 30 Detector* [online]. 2019 [viewed on 21 November 2018]. Available from www.bruker.com/products/x-ray-diffraction-and-elemental-analysis/eds-wds-cbsd-sem-micro-xrf-and-sem-micro-ct/quantax-eds-for-sem/quantax-hardware/xflashr-6-30-detector.html.
179. Atkins, P., De Paula, J. *Physical Chemistry*. 8th ed. Oxford University Press: Oxford, UK, 2006.
180. OSBORNE, B. G. *Near-infrared spectroscopy in food analysis*. Encyclopedia of analytical chemistry. John Wiley & Sons, USA, 2006.
181. VILLAR, A., GORRITXATEGI, E., ARANZABE, E., FERNANDEZ, S., OTADUY, D. & FERNANDEZ, L. A. Low-cost visible-near infrared sensor for on-line monitoring of fat and fatty acids content during the manufacturing process of the milk. *Food chemistry*. 2012, **135**(4), 2756-2760.
182. LAU, W. S. *Infrared characterization for microelectronics*. World scientific, 1999. ISBN 978-981-02-2352-6.
183. *Infrared spectroscopy at ColourLex* [online]. 2019 [viewed on 27 May 2019]. Available from <https://colourlex.com/project/infrared-spectroscopy/>.
184. DERRICK, M. R., STULIK, D., LANDRY & J. M. *Infrared spectroscopy in conservation science, scientific tools for conservation*. J. Paul Getty Trust, USA, 1999. ISBN 0-89236-469-6.

185. RICCIARDI, P. *Unlocking the secrets of illuminated manuscripts* [online]. 2012 [viewed on 27 May 2019]. Available from http://www.labnews.co.uk/article/2027499/unlocking_the_secrets_of_illuminated_manuscripts.
186. Wilson, E.J. *Strain-Gage Instrumentation. Harris' Shock and Vibration Handbook, 5th ed.* McGraw-Hill: New York, USA, 2002. ISBN 978-0071508193.
187. *Sensor head LK-G82* [online]. 2019 [viewed on 25 June 2019]. Available from <https://www.keyence.com/products/measure/laser-1d/lk-g3000/models/lk-g82/index.jsp>
188. *Control block LK-G3001P* [online]. 2019 [viewed on 25 June 2019]. Available from <https://www.keyence.com/products/measure/laser-1d/lk-g3000/models/lk-g3001pv/index.jsp>
189. JANUSAS, G.; PALEVICIUS, A. & BUBULIS, A. Numerical analysis of holographic plate stability. *Vibroengineering 2008: Proceedings of the 7th International Conference*. Kaunas, Lithuania, 9-11 October 2008, Mechanika.
190. YEPES, INDIRA S. V. & GESUALDI, M. R. R. Dynamic digital holography for recording and reconstruction of 3D images using optoelectronic devices. *Journal of Microwaves, Optoelectronics, and Electromagnetic Applications*. 2017, **16**(3), 797-811.
191. KELLY, D. P., MONAGHAN, D. S., PANDEY, N., KOZACKI, T., MICHALKIEWICZ, A., FINKE, G., HENNELLY, B. M. & KUJAWINSKA, M. Digital holographic capture and optoelectronic reconstruction for 3D displays. *International Journal of Digital Multimedia Broadcasting*. 2009, **2010**(10).
192. DEL SOCORRO HERNANDEZ-MONTES, M., FURLONG, C., ROSOWSKI, J. J., HULLI, N., HARRINGTON, E., CHENG, J. T., RAVICZ, M. E. & SANTOYO, F. M. Optoelectronic holographic otoscope for measurement of nano-displacements in tympanic membranes. *Journal of Biomedical Optics*. 2009, **14**(3).
193. DEAN STRAW, R. *The ARRL Antenna Book*. The American Radio Relay League, Inc., Newington, CT: ARRL, USA, 2007.
194. HUTCHINSON, C. *The ARRL Handbook for Radio Amateurs 2001*. Newington, CT: ARRL, USA, 2001.
195. *Problems with VSWR in Medical Applications* [online]. 2019 [viewed on 27 June 2019]. Available from <https://www.microwaves101.com/encyclopedias/problems-with-vswr-in-medical-applications>.
196. PAVLINA, E. J. & VAN TYNE, C. J. Correlation of yield strength and tensile strength with hardness for steels. *Journal of Materials Engineering and Performance*. 2008, **17**(6), 888-893.
197. TABOR, D. *The Hardness of Metals*. Oxford University Press, USA, 2000. ISBN 9780198507765.
198. WILDE, H. R. & WEHRSTEDT, A. Introduction of Martens hardness HM. *Materialpruefung*. 2000, **42**(11-12), 468-470.
199. *Micro Scratch Tester MST³* [online]. 2019 [viewed on 1 July 2019]. Available from <https://www.anton-paar.com/corp-en/products/details/micro-scratch-tester-mst3/>
200. BENAM, M.R. Monitoring the processing steps of Pb (Zr0.52 Ti0.48) O₃ nano powders by FTIR technique. *International Journal of Recent Research Aspects*. 2014, **18**(2), 145–150.
201. ABDELRAZEK, E.M., HEZMA, A.M., EL-KHODARY, A. & ELZAYAT, A.M. Spectroscopic studies and thermal properties of PCL/PMMA biopolymer blend. *Egyptian Journal of Basic Applied Sciences*. 2016, **3**(1), 10–15.
202. SONG, X., LIN, Q., CHEN, C., CHEN, J. & HU, C. Discrimination between virgin and recycled polystyrene containers by Fourier transform infrared spectroscopy and principal component analysis. *Packaging Technol and Science*. 2018, **31**(10).

203. NOHEDA, B., GONZALO, J.A., CROSS, L.E., GUO, R., COX, D.E., PARK, S.E. & SHIRANE, G. Tetragonal-to-monoclinic phase transition in a ferroelectric perovskite: The structure of $\text{Pb Zr}_{0.52} \text{Ti}_{0.48} \text{O}_3$. *Physical Review. B, Condensed matter*. 2000, **61**(13), 8687–8695.
204. TSU, R. *Superlattice to nanoelectronics, 2nd ed.* Elsevier: London, UK, 2011. ISBN 9780080968131.
205. ZHANG, H.Q., JIN, Y. & QIU, Y. The optical and electrical characteristics of PMMA film prepared by spin coating method. *IOP Conference Series: Materials Science and Engineering*. 2015, **87**.
206. GILL, A., ARSHAK, A., ARSHAK, K. & KOROSTYNSKA, O. Effects of polymer binder, surfactant and film thickness on pH sensitivity of polymer thick film sensors. *Proceedings of the Eurosensors XXIII conference I*. Lausanne, Switzerland, 6–9 September 2009, Elsevier.
207. ZHONG, Z., ZHOU, J., ZHANG, H., ZHANG, H., ZHANG, W. & MENG, G. Thermoelastic damping in fluid-conveying microresonators. *International Journal of Heat Mass Transfer*. 2016, **93**, 431–440.
208. XUA, J., LIA, Y., GEB, D., LIUA, B. & ZHUA, M. Experimental investigation on constitutive behaviour of PVB under impact loading. *International Journal of Impact Engineering*. 2011, **38**(2), 106–114.
209. LERCH, B.A., THESKEN, J.C. & BUNNELL, C.T. *Polymethylmethacrylate (PMMA) Material Test Results for the Capillary Flow Experiments (CFE)*; NASA/TM—2007-214835; 2007; pp. 1–16. NASA technical reports server. Available online: <https://ntrs.nasa.gov/search.jsp?R=20070030192> (accessed on 19 November 2018)
210. PIANIGIANI, M., KIRCHNER, R., SOVERNIGO, E., POZZATO, A., TORMEN, M. & SCHIFT, H. Effect of nanoimprint on the elastic modulus of PMMA: Comparison between standard and ultrafast thermal NIL. *Microelectronic Engineering*. 2006, **155**, 85–91.
211. ARNOLD, D. N., MADUREIRA, A. L. & ZHANG, S. On the range of applicability of the Reissner-Midlin and Kirchhoff-Love plate bending models. *Journal of elasticity*. 2002, **67**(3), 171-185.
212. PEENI, B. A., LEE, M. L., HAWKINS, A. R., WOOLEY, A. T. Sacrificial layer microfluidic device fabrication methods. *Electrophoresis*. 2006, **27**(24), 4888-4895.
213. *Thermal evaporation in vacuum* [online]. 2019 [viewed on 12 August 2019]. Available from https://www.icmm.csic.es/fis/english/evaporacion_resistencia.html.
214. DIAZ, V. H. G. & TOST, G. O. Butanol production from lignocellulose by simultaneous fermentation, saccharification, and pervaporation or vacuum evaporation. *Bioresource Technology*. 2016, **218**, 174-182.
215. SABANCI, S. & ICIER, F. Applicability of ohmic heating assisted vacuum evaporation for concentration of sour cherry juice. *Journal of Food Engineering*. 2017, **212**, 262-270.
216. MA, D., DUAN, L. & QIU, Y. Orange-red- and white-emitting diodes fabricated by vacuum evaporation deposition of sublimable cationic iridium complexes. *Journal of Materials Chemistry C*. 2016, **22**.
217. HAAZ, E., FOZER, D., NAGY, T., VALENTINYI, N., ANDRE, A., MATYASI, J., BALLA, J., MIZSEY, P. & TOTH, A. J. Vacuum evaporation and reverse osmosis treatment of process wastewaters containing surfactant material: COD reduction and water reuse. *Clean Technologies and Environmental Policy*. 2019, **21**(4), 861-870.
218. TAYLOR, H., LAM, Y. C. & BONING, D. A computationally simple method for simulating the micro-embossing of thermoplastic layers. *Journal of Micromechanics and Microengineering*. 2009, **19**(7).

219. SHAN, X. C. & MOHAHIDIN, M. B. Roll-to-roll thermal embossing for large area microstructure formation and application. *2015 Symposium on Design, Test, Integration and Packaging of MEMS/MOEMS (DTIP)*. Montpellier, France, 27-30 April 2015, IEEE.
220. DHINESH, K. S., SUBHASANKARI, T., PANEERSELVAM, T. & VENKATESAN, M. Simulation and numerical analysis of warm stamping (AA6061). *Materials today: Proceedings*. 2019, **16**(2), 598-603.
221. SODAH, A., GAIDYS, R., NARIJAUSKAITE, B., SAKALYS, R., JANUSAS, G. & PALEVICIUS, A. Analysis of microstructure replication using vibratory assisted thermal imprint process. *Microsystem Technologies*. 2019, **25**(2).

